# UNIVERSITÀ DEGLI STUDI DI MILANO

Department of Biosciences

PhD Course in Molecular and Cellular Biology

**XXXII Cycle**

# *The double life of the Apoptosis Inducing Factor (AIF): the pro-survival role of a pro-death protein*

Paolo Cocomazzi

PhD Thesis

Tutor: Prof. Alessandro Aliverti

Co-Tutor: Eloise Mastrangelo

Academic year 2018-2019

# Abstract

Beside its apoptotic function, the Apoptosis Inducing Factor (AIF), a highly conserved mitochondrial flavoprotein, plays a pro-vital role in eukaryotic cells through its interaction with CHCHD4, a mitochondrial protein that contributes to oxidative folding of respiratory complexes' subunits. A unique feature of AIF is the ability to form a tight, air-stable charge-transfer complex (CT complex) upon reaction with NAD(H), which leads to protein dimerization modulating the affinity for its ligands.

To date, nine point mutations of the human AIF gene were found to cause rare and severe neurodegenerative mitochondriopathies. To define the molecular bases of the pathogenicity of AIF variants, we selected a set of AIF mutations (G337E, D236G, G261S and F133L) and investigated their effects on both AIF molecular properties and its interaction with CHCHD4. To this aim, a combination of biophysical techniques, Microscale Thermophoresis (MST) and structural biology was used. AIF variants CT complex stability was evaluated studying its reoxidation by $O_2$. Interestingly, CT complex of G337E and G261S forms displayed a faster oxidation compared to wild type AIF, indicating a lower stability. Moreover, the 3D structures of the CT complex of AIF-D236G and of AIF-F133L both in oxidized and CT complex state were obtained, showing, however, no significant structural rearrangements with respect to the wild type protein. Hence, we investigated possible alterations of the interaction with CHCHD4 induced by AIF pathogenic mutations. Through a MST approach, for the first time we quantitatively studied redox-dependent effects of AIF amino acid replacements on its affinity for CHCHD4, revealing a possible involvement of the G337 residue in protein-protein complex formation. We characterized the AIF-CHCHD4 complex also from a structural point of view using the Small-Angle X-ray Scattering (SAXS) technique, through which we identified a putative interaction region between the two proteins. In addition, all SAXS models obtained revealed that the solvent-exposed G337 residue is localized in the neighborhood of the identified region, in agreement with a possible role of this residue in complex formation. Our results, not only shed new light on AIF-CHCHD4 relationship, but also provide a possible explanation of the pathogenicity of the AIF G337E allelic variant.

# Riassunto

Oltre al suo ruolo apoptotico, l'Apoptosis Inducing Factor (AIF), una flavoproteina mitocondriale altamente conservata, possiede un ruolo essenziale nelle cellule eucariotiche, svolto tramite la sua interazione con CHCHD4, un'altra proteina mitocondriale che regola il folding ossidativo delle subunità che compongono i complessi respiratori. Caratteristica unica che contraddistingue AIF è la sua capacità di formare un complesso a trasferimento di carica (CT complex) stabile all'ossigeno in seguito al legame con il NAD(H), il quale porta alla dimerizzazione della proteina.

Ad oggi, nove mutazioni puntiformi del gene umano di AIF sono state identificate causare rare ma gravi mitocondriopatie neurodegenerative. Al fine di caratterizzare la patogenicità della varianti alleliche di AIF, abbiamo selezionato un gruppo di mutazioni di AIF (G337E, D236G, G261S and F133L) e studiato il loro effetto sia sulle sue proprietà molecolari sia sulla sua interazione con CHCHD4. Con questo obbiettivo, abbiamo utilizzato una combinazione di tecniche spettrofotometriche, di MicroScale Thermophoresis (MST) e di biologia strutturale. La stabilità delle specie CT complex dei mutanti di AIF sono state studiate valutando la loro riossidazione in presenza di $O_2$. Il CT complex dei mutanti G337E e G261S ha mostrato una più rapida riossidazione a confronto con la forma selvatica, un chiaro segno della loro minore stabilità. Inoltre, sono state ottenute le strutture del mutante D236G in forma ridotta e quelle del mutante F133L sia in forma ridotta che ossidata, ma il loro confronto con la proteina selvatica non ha evidenziato cambiamenti conformazionali significativi. Quindi, abbiamo studiato le possibili alterazioni sull'interazione AIF-CHCHD4 indotte dalle mutazioni patologiche di AIF. Tramite l'approccio MST, abbiamo caratterizzato quantitativamente gli effetti legati ai cambiamenti redox di AIF sulla sua interazione con CHCHD4, mostrando un probabile ruolo del residuo G337 nella formazione del complesso proteina-proteina. Inoltre, abbiamo caratterizzato il complesso AIF-CHCHD4 anche da un punto di vista strutturale tramite la tecnica di Small-Angle X-ray Scattering (SAXS), attraverso cui abbiamo identificato una possibile regione di interazione tra le due proteine, in prossimità del residuo 337 esposto al solvente. Questi risultati non solo gettano nuova luce sulla ancora poco caratterizzata interazione tra AIF e CHCHD4, ma possono fornire una possibile spiegazione del meccanismo patogenetico della mutazione G337E.

# 1. Introduction

## 1.1 Flavoproteins

Flavoproteins are proteins that contain the prosthetic group Flavin Adenine Dinucleotide (FAD) and/or Flavin MonoNucleotide (FMN), a derivative of riboflavin. This compound was isolated for the first time in 1879, as a result of a study concerning the composition of cow milk, and it was described as a bright yellow pigment. By the early 1930s, the same pigment was isolated from different sources and it was discovered to be a component of the vitamin B complex. In 1934, its structure was investigated and determined by two groups, which named it riboflavin, from the ribose-derived side chain and the yellow color of the conjugated ring system, namely the isoalloxazine ring[1]. The following year, Hugo Theorell and collaborators provided the first evidence that the flavin cofactor is required for enzymatic activity, through the isolation a bright-yellow colored yeast protein, implicated in cellular respiration, that could be separated into its apoprotein and a yellow pigment. Notably, they showed that neither the apoprotein nor the pigment alone had the ability to oxidize NADH, but the enzymatic activity was re-established by combining both of them. In addition, Theorell group replaced the isolated pigment with riboflavin observing that the enzyme was no more catalytically active, and demonstrated that the protein didn't require riboflavin, but instead FMN for its enzymatic activity. Three years later, Warburg and Christian performed similar studies on the enzyme D-amino acid oxidase, identifying FAD as a second form of flavin cofactor exploited by enzymes.

Flavoproteins cofactors can be considered natural reporters of changes in flavoproteins active site, thanks to their spectroscopic properties, making them one of the most biochemically and structurally characterized protein family.

To date, in the NCBI database more than 100,000 flavoprotein sequences are available and the Protein Data Bank (PDB) contains hundreds of structures of either FAD- or FMN-containing proteins, which present different structural features such as the common $(\alpha\beta)_8$ barrel or the unique $\alpha+\beta$ structure of acyl-CoA dehydrogenase.

Flavoenzymes can catalyze a variety of biochemical reactions as, for instance, hydroxylation and dehydrogenation of metabolites, but redox reactions represent the most large reactions group in which they are involved (Fig. 1.1).

Given their wide range of catalytic functions, flavoproteins are implicated in essential biochemical processes including photosynthesis, oxidative stress protection, DNA repair and apoptosis[2]. Moreover, cellular redox reactions are often linked to neurodegenerative diseases, and flavoproteins, which are ubiquitous redox enzymes, are often involved in the etiology of such disorders, as in the case of the Apoptosis Inducing Factor (AIF).

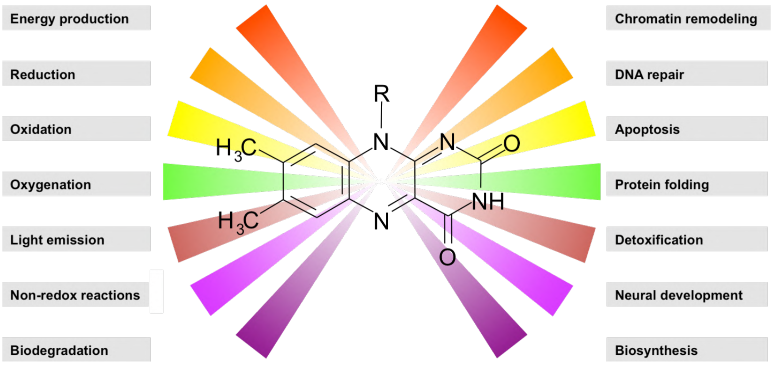

**Fig. 1.1 Important biological processes in which flavoproteins are involved.** At the center of the scheme, the dimethyl-isoalloxazine ring of flavin cofactors is shown (Joosten and van Berkel, 2007).

## 1.2 The Apoptosis Inducing Factor (AIF)

The apoptosis inducing factor (AIF) is a highly conserved mitochondrial flavoprotein which promotes caspase-independent apoptosis in vertebrates and in most other eukaryotes[3]. The AIF gene (*AIFM1* in humans) is localized on the X chromosome in humans and mice[4]. Gene expression results in a 67 kDa precursor apoprotein composed by 613 residues (Fig. 1.2A) which contains a 53 aa N-terminal mitochondrial localization sequence (MLS) and two nuclear leading signals (NLS), one located in the central and the other in the C-terminal portions of the protein.

The AIF precursor import into mitochondria occurs only when the protein is in the unfolded state[5] and, once in the organelle, MLS is cleaved, folding and FAD incorporation occur to yield the mature form of the protein, indicated as AIFΔ1-54 (Fig. 1.2B). AIFΔ1-54 resides in the mitochondrial intermembrane space (IMS), tethered to the inner membrane through to its N-terminus.

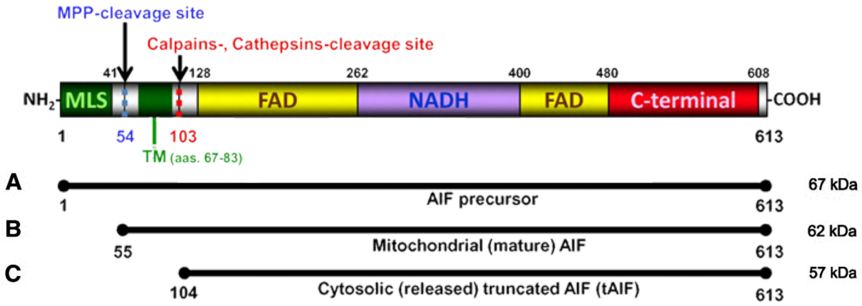

**Fig. 1.2 Major human AIF forms.** AIF precursor (**A**): MLS, Mitochondrial Processing Peptidase (MPP) cleavage site, calpain cleavage site, discontinuous FAD or NAD(H) binding domains are indicated. (**B**) Mature form of AIF produced upon mitochondrial processing. (**C**) Soluble and apoptogenic form of AIF (Yuste *et al.*, 2007).

After an apoptotic stimulus, the proteolytic cut of mature AIF is promoted by proteases such as μ-calpain, resulting in the generation of the soluble and pro-apoptotic form of the protein (AIFΔ1-102, Fig. 1.2C). As a consequence, AIFΔ1-102 is released from mitochondria into the cytoplasm and it is translocated into the nucleus where it recruits other proteins, binds DNA, promoting chromatin condensation and large scale DNA degradation in a caspase-independent apoptotic pathway[6].

The first AIF three-dimensional structure was solved for the oxidized form of refolded murine AIFΔ1-120, providing the first structural insights into the protein architecture[7]. AIF is a member of the glutathione-reductase (GR) protein superfamily and it comprises three structural domains: a discontinuous FAD-binding domain (aa 129-170, 203–262 and 400–479) and an NAD(P)H-binding one (aa 171–202 and 263–399), both characterized by the classical Rossmann fold topology, and a C-terminal domain (aa 478-610) which presents five antiparallel β-strands followed by two α-helices (Fig. 1.3). As a GR-like flavoprotein, the FAD-binding domain is the most conserved portion of AIF, which is unique for its the N-terminal insertion (aa 190–202), folded as a β-hairpin. This peptide establishes multiple contacts with the main core of the protein via hydrophobic and polar interactions , which are believed to play important roles in the conformational transitions of AIF as well as in the interaction with its partners[6]. The NADH-binding domain is well conserved in AIF, even if it has a larger pocket with respect to most other GR-like proteins and presents fewer specific contacts for NADH.

The C-terminal domain is usually the most variable portion of GR-like flavoproteins: another unique feature of AIF is the regulatory 509–559 insertion, a peptide organized into two short α-helices (aa 517–523) and an extended loop, which, together with the β-hairpin and the two α-helices of the C-terminal insertion, regulates the access to the active site.

Moreover, the regulatory peptide is involved in protein-protein interactions thanks to its PEST sequence, modulates the proteolytic cleavage by μ-calpain and regulates AIF redox properties, crucial for its function, as well as DNA binding.

Surprisingly, the first murine AIF three-dimensional structure showed the absence of canonical DNA-binding motifs, though the protein was known to directly associate with DNA. This issue was solved when the crystal structure of human AIFΔ1–120 was determined[8]. The human protein showed the same fold as the murine one but, due to a different crystal packing, its 540–559 fragment was disordered, leading to a positive electrostatic potential, due to the presence of Arg584 and Lys590 residues on the protein surface. Together with several other amino acids, these basic residues organize in a positively charged patch that allows AIF to interact with DNA.

In 2008, Churbanova and Sevrioukova solved the X-ray structure of naturally folded murine AIFΔ1-77, which lacks only the membrane binding domain, thus mimicking the mature intramitochondrial form of the protein. From the comparison between this structure and the one solved for the apoptogenic AIFΔ1-120 it was discovered a 0.6 Å displacement of the FAD cofactor and a different conformation of the 438-453 peptide, which connects the active site with the crystallographic dimer interface.

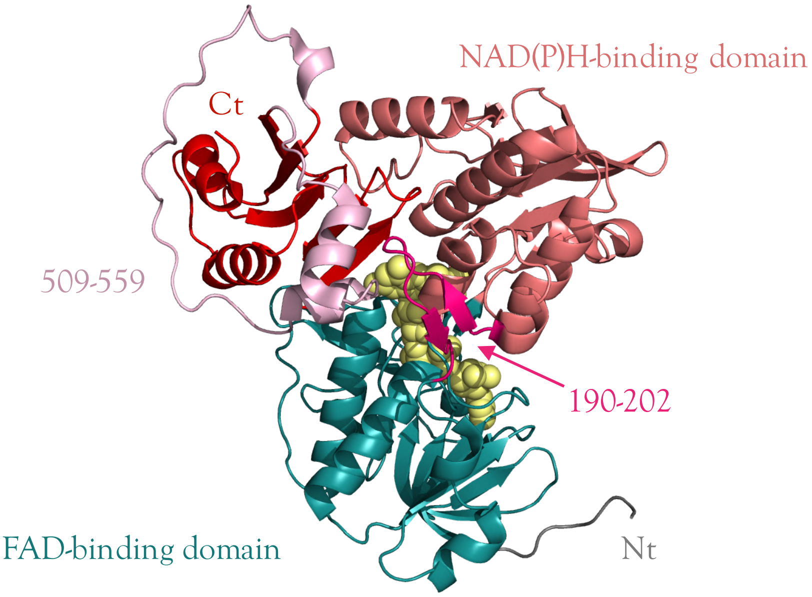

**Fig. 1.3 Three-dimensional structure of refolded murine oxidized AIFΔ1-120.** The FAD-binding, NAD(H)-binding, and C-terminal domains are depicted in deep teal cyan, deep salmon red and red, respectively. FAD is in a yellow spacefill representation. The extended N-terminus (gray), the 190–202 insertion folded as a β-hairpin (hot pink), and the C-terminal 509–559 insertion (light pink) are unique features of AIF (Mate *et al.*, 2002; PDB 1GV4).

The 438-450 peptide forms a loop in refolded AIFΔ1-120, while it forms a β-turn in naturally folded AIFΔ1-77, where Arg448 forms a salt bridge with Glu412 to assist dimerization: this altered conformation could have a large impact on formation and stabilization of the dimeric charge-transfer (CT) complex (*see* § 1.2.1). It is known that AIF acts as a pro-apoptotic factor promoting caspase-independent apoptosis. Nevertheless, in addition to its well characterized lethal function, in the last few years many evidences supported the importance of mitochondrial AIF as a pro-survival factor, although the precise vital role of the flavoprotein still remains unknown. Nowadays, it is widely accepted that AIF acts a redox sensor in the IMS, an hypothesis validated in 2015 by the Hangen's group which discovered the interaction between AIF and CHCHD4, a mitochondrial protein involved in the import and assembly of substrates implicated in the biogenesis of respiratory chain complexes subunits[9].

### 1.2.1 AIF redox properties

As member of the GR family, characterized by NADH/NADPH-dependent reductase activity towards different electron acceptors[6], AIF can function as a nicotinamide dinucleotide-dependent enzyme, though with a remarkably low turnover number, acting on unknown endogenous substrate(s). However, AIF reaction with NAD(H) is of great interest for its biochemical properties. In fact, the NAD(H) binding to AIF results in the formation of an exceptionally air-stable $(FADH^-)$-$NAD^+$ charge-transfer (CT) complex. The CT complex is the non-covalent association of two chemical entities, where a fraction of the electronic density of one of them (the electron donor) is transferred to the other (the electron acceptor), causing the modification of the electronic structure of the engaged entities and generating new allowed electronic transitions corresponding to characteristic new bands in the light absorption spectrum of the CT complex. In the case of AIF, NADH acts as electron donor to reduce FAD, according to the reaction:

$$\mathrm{AIF(FAD)} + \mathrm{NADH} \Leftrightarrow (\mathrm{FADH}^-) - \mathrm{NAD}^+$$

The above reaction also is coupled to the transition of the AIF between monomeric and dimeric states. This led to the hypothesis that AIF could represent a redox and/or NADH sensor, whose quaternary structure changes are part of a novel signal-transduction pathway.

In addition to dimerization, the formation of the CT complex causes large conformational changes in AIF, first of all leading to shift in the FAD position of about 1.2 Å to optimize the π-π interactions between the flavin and nicotinamide rings at the basis of the CT complex. In this configuration, the nicotinamide ring of $NAD^+$ position itself in between the isoalloxazine of FAD and the aromatic residue Phe309. With respect to other flavoproteins, a unique feature of AIF active site is the presence of His453, which undergoes a large positional shift to establish an H-bond with nicotinamide, properly orienting redox groups for charge transfer (Fig. 1.4). Moreover, NADH binding triggers rearrangement of a number of aromatic residues (Y559, F507, Y346, W578, W350, Y491, F481, F309, H453), whose side chains align in a tunnel spanning from the active site to the surface. Tyr559 undergoes the largest movement (> 9.0 Å) and shields the tunnel from the solvent. With the ring-to-ring distance of < 4.0 Å, the aromatic cluster is perfectly suited for transfer/delocalization of electrons, which could extend the lifetime of the reduced species. Redox signal transmission from the active site to the protein surface occurs due to the adjacent 438-452 peptide, suggesting that His453 could be involved not only to CT complex stabilization but also in protein dimerization[10].

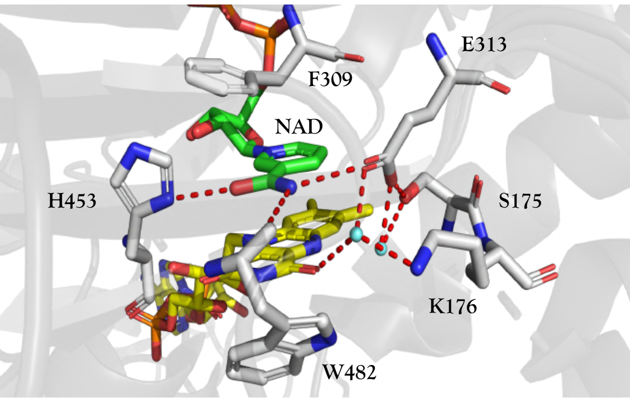

**Fig. 1.4 Structure of AIF active site when in CT complex with $NAD^+$.** $NAD^+$ nicotinamide ring (shown in green) is parallel stacked between the isoalloxazine of FAD (shown in yellow) and Phe309, establishing an H-bonding network with the surrounding residues. One of these, His453, undergoes a large positional shift upon AIF reduction (Sevrioukova, 2011).

In addition, also the regulatory 509-559 insertion is involved in monomer-dimer transition, as it is crucial for AIF protein-protein interactions, and contains a PEST sequence, which regulates the proteolysis of the flavoprotein by the action of μ-calpain. Solvent exposure of the 509-559 peptide is controlled by the FAD redox state and it is proposed to have implications in AIF protein-protein interactions during caspase-independent apoptosis.

Moreover, the Arg449 residue of the Arg449-Glu413 salt link is part of NLS2, which is less accessible when AIF is in its CT complex state and, because of its minor sensitivity to μ-calpain proteolytic cleavage, dimeric AIF is considered less prone to induce apoptosis than its oxidized and monomeric form.

AIF redox state drives its dual function in eukaryotic cells, possibly modulating the sensing/transducing role of the flavoprotein. In healthy mitochondria, reduced nicotinamide cofactors are abundant in the IMS and intramitochondrial AIF is predominantly in its dimeric CT complex form, contributing in the assembly and functioning of the respiratory chain, probably through interaction with CHCHD4 (*see* § 1.2.5). After an apoptotic stimulus, NAD(P)H concentration rapidly decreases leading to oxidation of AIF. In the oxidized state, AIF is more sensitive to proteolytic cleavage by μ-calpain and more prone for translocation into the nucleus, thus acting as a pro-apoptosis factor. Damage of mitochondrial inner membrane, to which AIFΔ1-54 is tethered, could also concur in the transient dissociation of AIF dimers and leading to an increase of ROS species in the IMS, with promotion of AIF proteolytic cut and its subsequent release into the cytosol.

Since different pools of nicotinamide nucleotides could be found in mitochondria, cytoplasm and nucleus, the AIF interaction with NADH could modulate properties of the flavoprotein also outside the organelle, playing a role in its nuclear translocation and DNA binding. In fact, after AIF dimerization and conformational rearrangement of the 509-559 peptide, the charge distribution on the flavoprotein surface could change resulting in an altered affinity for DNA[10]. Also the 190-202 β-hairpin is sensible to the redox state of AIF, as it is released during dimerization, and probably this could affect the AIF interactions with other protein partners.

### 1.2.2 AIF lethal role

The molecular mechanism of the AIF lethal function was deeply characterized[6,11], showing that permeabilization of mitochondria is an obligatory event in the AIF-mediated apoptotic signaling. AIF plays a crucial role in the so called intrinsic, or mitochondrial, apoptotic pathway: intracellular stimuli such as irreparable DNA damage and severe oxidative stress (ROS) result in mitochondrial morphology modifications that, coupled to the loss of mitochondrial transmembrane potential, induce the release of pro-apoptotic proteins from the intermembrane space.

The intrinsic pathway is regulated by proteins of the Bcl-2 family that modulate mitochondrial membrane permeability and can act as either pro-apoptotic (e.g., Bid, Bak, Bax) or anti-apoptotic (e.g., Bcl-2, Bcl-XL) factors[12]. The physiologic function of Bcl-2 and Bcl-XL is to avoid the release of mitochondrial proteins, probably by controlling the activation of caspase proteases[13].

Under apoptotic conditions, pro-apoptotic protein Bid is cleaved by caspases and promotes the activation of membrane pore-forming proteins Bak and Bax: they can homo-oligomerize leading to the permeabilization of the mitochondrial outer membrane and the release of mitochondrial proteins (Fig. 1.5).

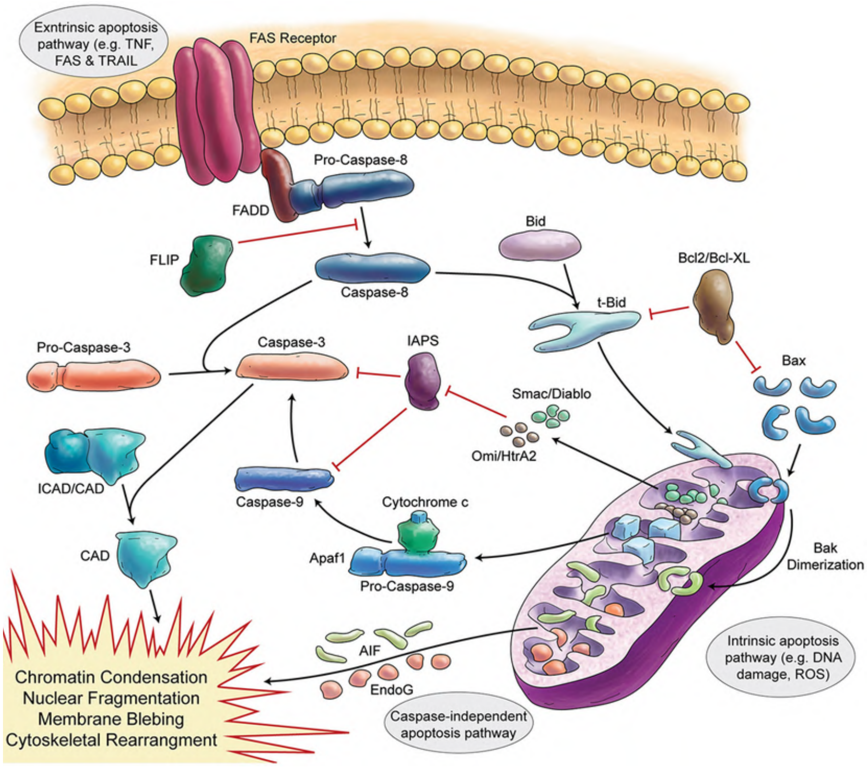

**Fig. 1.5 Mammalian intrinsic and extrinsic apoptotic pathways.** The scheme reports the most important factors of the two apoptotic pathways: AIF plays a crucial role in the intrinsic one promoting caspase-independent apoptosis (Hassan Marzban *et al.*, 2015).

Currently, two models have been proposed to describe the mechanism through which AIF is released to the cytosol. According to the first model, opening of mitochondrial permeability transition pore (MPTP) allows small molecules to enter the mitochondrial matrix, leading to swelling of the organelle.

Under these conditions, Poly(ADP-ribose) polymer can trigger dissipation of the mitochondrial membrane potential ($\Psi$m) and, thus, altering mitochondrial $Ca^{2+}$ homeostasis. In the second model, instead, pro-apoptotic Bcl-2 family members could promote the formation of pores that cause permeabilization of mitochondria, without affecting $\Delta\Psi$m.

In both models, after mitochondrial permeabilization, the membrane tethered AIFΔ1-54 undergoes proteolytic cleavage thanks to the action of $Ca^{2+}$-dependent μ-calpain. Several *in vitro* evidences of the involvement of other proteases, like cathepsins B, L, S, have been provided but still have to be validated *in vivo*[14]. Proteolytic cleavage leads to the production of the soluble and apoptogenic form of AIF, called AIFΔ1-102, which can be easily released from mitochondria to the cytoplasm, where it can interact with pro-survival or pro-death protein partners. Interaction with different partners can be influenced by AIF redox state: many evidences showed that oxidized AIF possess a higher tendency to induce apoptosis, while reduced dimers have a higher affinity for pro-survival proteins.

Cyclophilin A (CypA) is an AIF pro-death partner and the AIF-CypA complex can be translocated into the nucleus, where AIF binds DNA through electrostatic interactions of a continuous patch of basic residues with the negatively charged sugar-phosphate backbone of DNA. AIF-DNA interaction causes peripheral chromatin condensation and large scale DNA degradation, but since AIF lacks nuclease activity, it was proposed to directly interact with DNA and recruiting proteases and nucleases to form DNA degrading complexes. Evidences of the cooperation of AIF with Endonuclease G were obtained in *C. elegans*[15] but not confirmed through studies on mammalian cells, while CypA-mediated interaction of AIF with histone H2AX seems to be essential for chromatinolysis[16].

### 1.2.3 AIF pro-survival role

In the last years, many studies supported the fact that, apart from its apoptotic function, AIF plays a pivotal role in some vital functions in mitochondria, even if the precise molecular mechanism of its action in the IMS still remains elusive. One issue linked to this problem is the great difficulty in separating AIF lethal and vital functions, as some of its apoptotic effects could be triggered after the protein is released from mitochondria. Homozygous *AIF* knockout in mice demonstrated to be embryonically lethal[17], probably due to an altered function of respiratory complex I[18]. Instead, it was possible to investigate the consequences of severe AIF deficiency thanks to the discovery of a useful animal model, the *Harlequin* (*Hq*) mouse, which presents an 80% decreased expression of the flavoprotein, caused by a retroviral insertion into the first intron of the AIF gene.

During early life stages, *Hq* mice are viable and do not exhibit phenotypic alterations. However, adult animals are characterized by lack of hair and develop progressive neurodegeneration, ataxia and blindness, and are resistant to weight gain and lipid accumulation[19]. Moreover, in *Hq* mice, AIF-deficient neurons and cardiomyocytes are sensible to peroxides and reactive oxygen species (ROS): this led to the hypothesis that AIF could function as an antioxidant and/or ROS scavenger that plays a role in oxidative phosphorylation (OXPHOS), but this possibility was later rejected by *in vitro* experiments on isolated mitochondria[20].

Further studies demonstrated that AIF-deficient neurons present short, fragmented mitochondria with $\Delta\Psi$m hyperpolarization and abnormally dilated cristae. Expression of AIF targeted to the inner mitochondrial membrane totally restores the alterations in cristae and respiratory defects[21]. It was therefore proposed that AIF is implicated in mitochondrial morphology and cristae formation, possibly via its interaction with OPA1, a GTPase directly involved in cristae remodeling and whose mutations are associated with familial autosomal dominant optic atrophy.

Although the flavoprotein does not tightly associate with any of the respiratory complexes, AIF deficiency or tissue-specific gene inactivation lead also to defects in the assembly and function of respiratory complexes I and III, causing OXPHOS impairment[22]. However, only expression of full-length AIF in AIF-negative cells could restore a proper OXPHOS function.

All the above observations suggested that the flavoprotein could play an important role in OXPHOS regulation and energy homeostasis as an assembly factor and/or redox sensor that assists the biogenesis of the multi-subunit complexes I and III.

Unfortunately, despite many efforts in the characterization of metabolic changes caused by AIF removal *in vivo*, the precise role of the mitochondrial flavoprotein has not been clearly identified yet.

### 1.2.4 Mia40/CHCHD4

Mia40, which is also referred to as CHCHD4 in mammalian cells, was initially isolated in mitochondria of budding yeast[23–25]. It is a soluble 16 kDa IMS protein characterized by the presence of seven cysteine residues, six of which are conserved and engaged in three disulfide bonds constituting a redox-sensitive cysteine-proline-cysteine site (or CPC motif) and a -$CX_9C$-$CX_9C$- motif. CHCHD4 contains a small helical segment in residues 56–59 (helix $\alpha$1) and two longer helical segments (helix $\alpha$2, residues 65–77, and helix $\alpha$3, residues 88–100), whereas the other 80% of residues, mainly located at the N and C termini, do not adopt any secondary structure, a large part of them being highly flexible.

Through NMR studies, the first and only available structure of CHCHD4 was obtained (PDB 2K3J), showing that the CPC motif exists in a solvent-exposed conformation protruding from a hydrophobic cleft (Fig. 1.6). This hydrophobic region consists of the strictly conserved phenylalanine residues Phe68, Phe72, Phe75 and Phe91, as well as Leu42, Ile43, Ile49, Trp51, Leu56, Met59, Ala60, Met94, Met98 and may function as a substrate binding site[26].

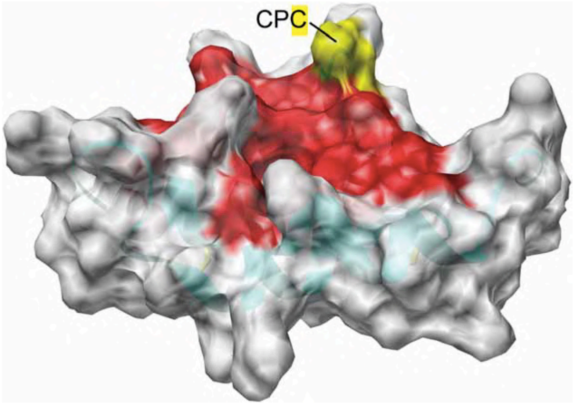

**Fig. 1.6 NMR structure of human CHCHD4.** The hydrophobic cleft on the surface is shown in red. The second cysteine of the CPC motif, Cys55, which lies adjacent to the hydrophobic cleft, is shown in yellow (Banci *et al.*, 2009, PDB 2K3J).

In healthy mitochondria, the protein acts as an oxidoreductase able to introduce disulfide bonds into its substrates, and several disulfide bonds-containing IMS proteins that are implicated in the biogenesis of respiratory chain complexes. Indeed, from mammalian cell-based experiments, CHCHD4 depletion resulted in reduced protein expression of several respiratory chain subunits leading to functional defects in complexes I and IV[9]. More in details, CHCHD4 works as an import receptor that performs two functions.

During the first step of its action, the peptide-binding cleft of CHCHD4 specifically binds to the internal IMS-targeting region of the incoming precursor through hydrophobic interactions. In the subsequent step, CHCHD4 covalently binds to one cysteine of the bound substrate through an intermolecular disulfide bond engaging the CPC active site[27].

Thus, CHCHD4 acts as a chaperone that promotes both the oxidative folding and entrapment of the substrate into the IMS. At the end of its catalytic cycle, after generating a disulfide in the substrate, the CPC motif is reduced and its reoxidation is ensured by the FAD-linked sulfhydryl oxidase Erv1 (ALR in humans).

Although the main catalytic and structural features of CHCHD4 have been conserved throughout eukaryotic evolution, in particular the segment that contains the CPC and the -$CX_9C$-$CX_9C$- motifs, there are important differences between yeast and mammalian homologs.

In contrast to yeast Mia40, which has a molecular mass of about 40 kDa, human CHCHD4 does not possess an N-terminal membrane-anchoring sequence. CHCHD4 has lost its hydrophobic inner-membrane anchor and has acquired the capacity to interact with a new partner, the flavoprotein AIF, which in turn is tethered to the mitochondrial inner membrane.

### 1.2.5 AIF interaction with CHCHD4

Few years ago, Hangen and collaborators provided new insights on the AIF pro-survival role, proving that this flavoprotein interacts and stabilizes the mitochondrial protein CHCHD4[9]. Through *in vitro* and *in vivo* experiments, they provided several evidences on the translation-dependent import of CHCHD4 into mitochondria and showed that it was affected by the presence of AIF. The knockdown of CHCHD4 did not diminish the abundance of AIF. In contrast, depletion of AIF led to a reduction of CHCHD4 protein expression, but the reduction of CHCHD4 protein levels in AIF-depleted cells was not accompanied by any change in the levels of CHCHD4 mRNA. The biochemical and functional consequences of AIF depletion were found to be similar to those observed as a result of CHCHD4 depletion, causing selective defects of respiratory chain complexes I and IV. In addition, the knockdown of either AIF or CHCHD4 had similar effects on the abundance of CHCHD4 substrates.

Hangen's group assessed also that AIF directly interacts with CHCHD4 within cells and this interaction does not require additional partners. However, no specific AIF polypeptide segment was found to be involved in binding, indicating that the interaction site of the flavoprotein could be conformational. On the other hand, the first N-terminal 27-residues of CHCHD4 were found to be necessary and sufficient for interaction with AIF. In this context, a crucial role of NADH was reported: in fact, in the presence of the compound significantly increased the affinity between the two proteins.

All of the above observations proved that the AIF-CHCHD4 interaction is a direct one, with AIF in the form of its dimeric membrane-associated CT complex with $NAD^+$, and that it binds the N-terminus of CHCHD4 and drags the protein into the mitochondrial intermembrane space, during its co-translational import into the organelle (Fig. 1.7). As CHCHD4 adopts its mature and functional conformation, it can regulate the import and assembly of respiratory complexes subunits and other IMS proteins.

The discovery of AIF-CHCHD4 interaction represented a crucial finding for a deeper understanding of the AIF vital role in mitochondria, also shedding new light on the effect of the flavoprotein on the biogenesis and maintenance of respiratory complexes. Hangen and collaborators proposed that this process could be mainly mediated by AIF physical and functional interaction with CHCHD4[9], though additional studies are needed for a full confirmation.

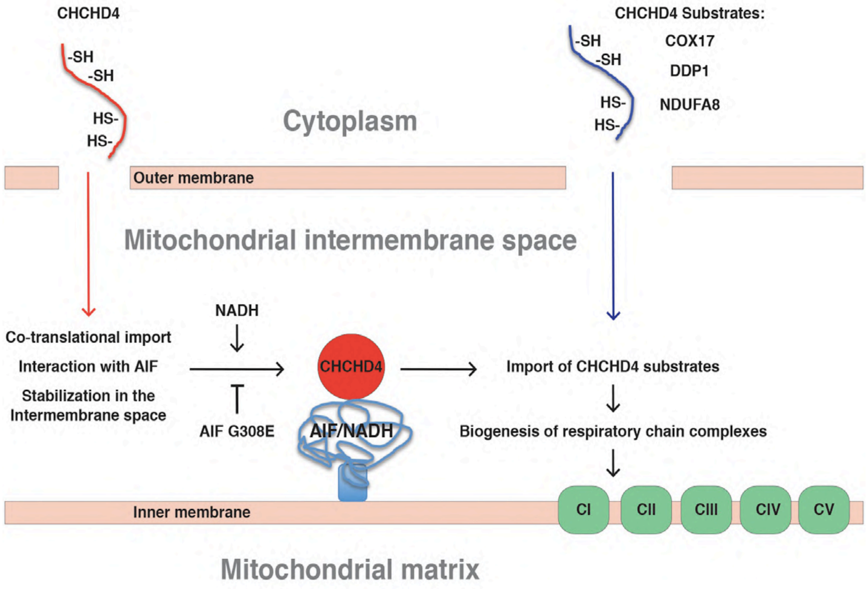

**Fig. 1.7 Schematic representation of AIF-CHCHD4 interaction** (Hangen *et al.*, 2015).

## 1.3 AIF-related diseases

Neuronal metabolism relies on mitochondrial functioning and particularly on OXPHOS, this representing the sole energy source for this cell type. Therefore, OXPHOS alterations or its complete failure are deleterious for the nervous system and are typically associated with neurodegeneration[28]. Both the *Hq* mouse and experimental models of AIF deficiency are characterized by OXPHOS defect, mitochondrial alterations and neuron loss[6].

To date, nine AIF allelic variants have been found to cause severe human mitochondriopathies, with neurodegeneration as a common feature. The deletion of R201[29], the G308E[30], G262S[31], G338E[32] and T141I[33], replacements cause mitochondrial encephalopathies. The V243L[34], F210S[35] and E493V[36] changes mainly cause peripheral symptoms such as muscular atrophy, neuropathy and deafness, with the condition associated to the latter mutation being also known as the Cowchock syndrome.

In addition to progressive neurodegeneration, the D237G replacement[37] was found to cause skeletal deformities and hypomyelination, a totally new feature associated to AIF-related diseases. Since the *AIFM1* gene is localized on the X chromosome, inheritance of all these mitochondrial-related diseases is X-linked and therefore they were found to affect male infants. However, the dual role that AIF plays in eukaryotic cells makes quite complicated the interpretation at the molecular level of clinical symptoms determined by flavoprotein defects.

In the last years, biochemical studies were performed on most AIF allelic variants to determine their structural/functional properties. The V243L, G262S and G338E mutations were found to cause a marked decrease of AIF level, probably due to the impairment of its folding and/or stability, leading to lower respiratory complex I and IV activities. The E493V and R201 mutations, instead, both significantly increase the rates of AIF reduction by NADH and CT complex reoxidation by molecular oxygen.

Moreover, the R201 deletion causes protein instability and subsequent tendency to lose the FAD cofactor. On the contrary, in the case of the E493V mutant, an increased apoptogenic activity of the flavoprotein seems to be at the basis of neurodegenerative disease. The AIF-G308E variant was associated with a disease similar to that caused by the R201. The G308 residue, highly conserved in vertebrate AIFs, is located in a crucial region of the NADH binding tunnel of the protein, occupying the second position of the canonical Rossmann fold GXGXXG motif.

Aim of the present PhD project was the biophysical characterization of the pathogenic AIF variants D237G, G338E and G262S to investigate in detail how the effect of these replacements are connected to the pathology onset. In addition, we studied a new mutant carrying the F134L replacement, recently identified by our collaborators at the Carlo Besta Neurological Institute in Milano in human patients, showing symptoms very similar of AIF-related mitochondriopathies.

### 1.3.1 The Arg201 deletion of AIF causes mitochondrial encephalomyopathy

Ten years ago, two male patients were found to be affected by a severe mitochondrial encephalomyopathy during their childhood, a disease linked to the deletion of Arg201 in human AIF[29]. They displayed symptoms including severe retardation in neuronal and psychomotor development, associated to mitochondrial respiratory chain defects due to a reduced functionality of respiratory complexes III and IV.

Only riboflavin administration seemed to temporally rescue their clinic condition. As the two patients were born from two twin sisters and two different fathers, it was speculated that the pathology was linked to the X chromosome. Further SNPs-based analysis was performed to analyze haploidentical region on their X chromosomes. The analysis identified a mutation in the *AIFM1* gene, coding for the apoptosis inducing factor. Both patients presented the deletion of an entire codon of the Arg201 residue of the protein.

Based on the crystal structure of AIF, (Fig. 1.4) Arg201 is localized in the β-hairpin (191-203 residues) that contributes to the conformational stability to the flavoprotein. Further studies demonstrated that Arg201 deletion does not dramatically impair AIF structure, but it leads to a decreased stability of the protein which, in addition, becomes more susceptible to proteases digestion. As a consequence, the biochemical features of AIF are altered. In particular, Arg201 deletion dramatically affect CT complex AIF(FADH$^-$)-NAD$^+$ stability, which is much lower with respect to that of the wild type protein. In addition, the mutant protein was found to bind less firmly the flavin prosthetic group, which is easily lost even during protein purification.

### 1.3.2 The D237G replacement of AIF leads to spondyloepimetaphyseal dysplasia

In 1999, Bieganski and collaborators described three male patients affected by spondyloepimetaphyseal dysplasia (SEMD) with mental retardation (MR). SEMD-MR was a novel syndrome with probably sex-linked recessive inheritance and unknown molecular defect. SEMD-MR symptoms include skeletal deformities and hypomyelination followed by progressive neurodegeneration affecting both central and peripheral nervous system.

During the analysis of a second family presenting SEMD-MR symptoms, in 2016, Mierzewska and collaborators provided evidences that in both families the disease is caused by the *AIFM1* p.Asp237Gly mutation.

The mutation is located in the first portion of the discontinuous FAD-binding domain of AIF and the D237 residue is part of a solvent-exposed β-sheet (Fig. 1.8). To date, the crystal structure of this AIF variant is not available and the substitution of an aspartic acid with a smaller residue as glycine may lead to local rearrangements, impairing the proper FAD incorporation and/or redox properties of AIF. Since *AIFM1* mutations are known to cause mitochondrial dysfunctions but no skeletal defects, SEMD-MR represents a novel phenotype of the *AIFM1* disease spectrum of unclear origin.

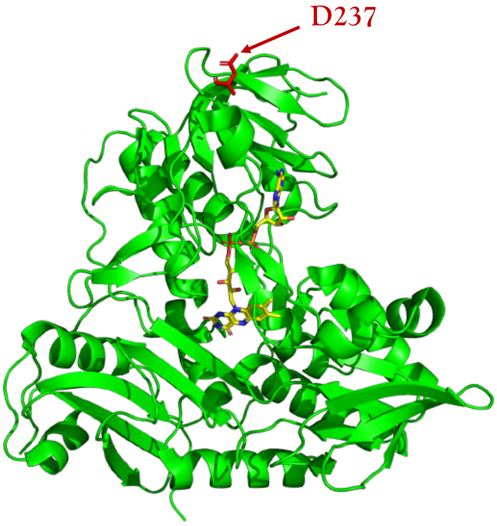

**Fig. 1.8 Crystal structure of the human Apoptosis Inducing Factor (PDB 4BV6).** The FAD cofactor and the D237 residue are depicted in yellow and red, respectively.

### 1.3.3 The discovery of the AIF G338E mutant

In 2015, Diodato and collaborators studied the clinical condition of two male cousins born from two sisters. The two patients presented a phenotype characterized by perinatal onset of marked hypotonia with proximal muscle weakness, resembling a spinal muscular atrophy (SMA) phenotype. Sanger sequencing of *AIFM1* revealed the novel missense change p.Gly338Glu hemizygous in both patient and heterozygous in their mothers. The G338E substitution falls nearby the protein region that bind the NAD(H) molecule involved in the formation of the FADH$^-$–NAD CT complex and the mutation may influence this interaction. The research group suggested that the amino acid replacement could have functional consequences because it involves residues that interact with the regulatory 510–550 peptide region, whose conformation is regulated by AIF redox state changes and is thought to determine the protein localization, lifetime, post-translational modifications, and interactions with other proteins as well as DNA. In fact, upon reduction with NADH the 510–560 peptide undergoes major dislocation, and despite being largely unstructured, a portion of this peptide results anchored nearby the site of the 388 residue by a network of interactions involving Lys337 (adjacent to Gly338), Glu346 and Gln556 (belonging to the regulatory peptide).

On the other hand, in the oxidized protein the 510–550 peptide is far away from the 388 site (Fig. 1.9A). Within a study of a selected group of AIF pathogenic variants, the crystallographic structure of the AIF-G338E variant in the oxidized state was obtained [38]. However, the structure analysis revealed only small positional shifts in the neighboring residues as a consequence of the bulkiness of the Glu338 side chain (Fig. 1.9B).

Thus, they suggested that the lower expression levels of the AIF mutant with respect to those of the wild type protein could be at the basis of the pathology, although the mutational effect on cellular physiology appears to be more complicated and therefore needs to be more thoroughly investigated.

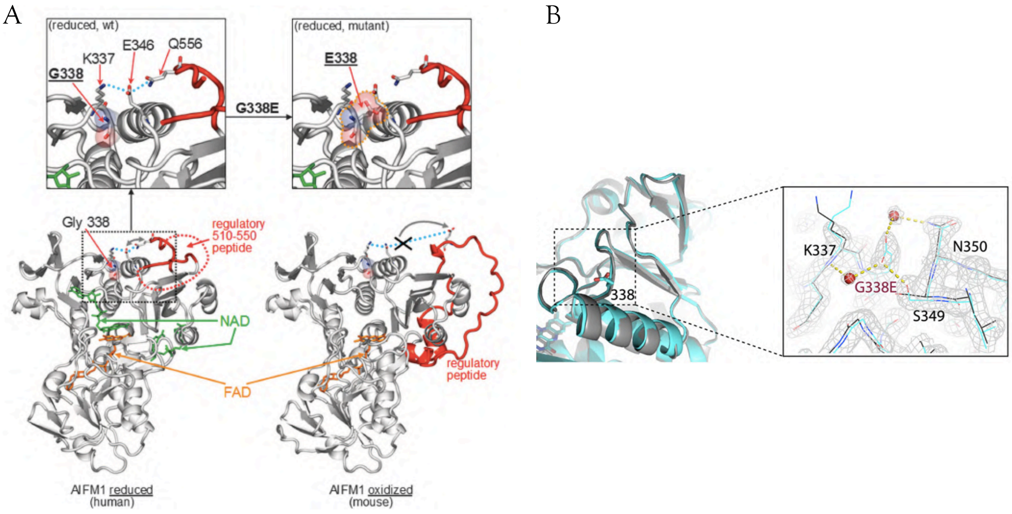

**Fig. 1.9** (**A**) Molecular structures of reduced human AIFM1 (Protein Data Bank, PDB 4BUR) and oxidized mouse AIFM1 (PDB 1GV4). G338, K337, E346 and Q556 in the reduced human protein, and the corresponding residues in the oxidized mouse protein are shown as sticks. Site of the G338E mutation is highlighted by a transparent surface. In the reduced human protein the region around Gly338 is shown together with an in silico Gly338 to Glu replacement to highlight the alterations that can be induced by the mutation (indicated by azure dots). The 510–560 peptide is colored in red and the red dotted line in the reduced human AIFM1 represents disordered portion of the peptide (Diodato *et al.*, 2015).(**B**) Superposition of the wild type and G338E AIF (in gray and cyan, respectively). Only minor conformational changes are observed in the crystal structure of the G338E mutant. The Glu338 side chain is well ordered and H-bonded to Lys337, Ser349, and Asn350 directly or via water molecules, shown as red spheres (Sevrioukova *et al.*, 2016).

### 1.3.4 The G262S AIF mutation causes a progressive mitochondrial encephalomyopathy

In 2015, Ardissone and collaborators reported the clinical conditions of a man with an early-onset, slowly progressive mitochondrial disease associated with a novel *AIFM1* mutation. During childhood, he developed gait and limb ataxia (sensory and cerebellar), hearing loss, and cognitive impairment. Visual deficit and distal muscle wasting and weakness became evident at puberty, with scanned speech, head and trunk titubation, and intention tremor, progressively more marked at repeated neurologic examinations. The sequencing of a panel containing more than 100 nuclear genes associated with mitochondriopathies revealed a hemizygous p.Gly262Ser mutation in *AIFM1* gene. Western blot analysis on patient fibroblasts showed strong reduction in AIF levels, indicating instability of the mutant protein and confirming a deleterious outcome of the identified variant.

Gly262 residue is localized on the border of the FAD- and NAD- binding domains, close to the flavin pyrophosphate group and in 2016 Sevrioukova obtained the crystal structure of AIF-G262S variant. After superimposition of the wild type and AIF-G262S structures, a notable (~1.0 Å) shift of the isoalloxazine ring, the redox moiety of FAD, was observed (Fig. 1.11A). This could be due to a slightly different interdomain orientation caused by different crystal packing. Thus, to more carefully highlighting the conformational changes, AIF-G262S was compared to the V243L mutant, which crystallizes in the same space group with its area near the catalytic site not affected by the V243L substitution. From the comparison, the G262S mutation was found to slightly distort the flavin mononucleotide portion of FAD (by ~0.2 Å; Fig. 1.11B,C). Ser262-triggered rearrangement in neighboring residues (Arg45, Glu453 and Leu400) may lead to a decrease in the conformational flexibility needed for structural adjustments during the association of NAD(H), causing a faster oxidation of CT complex and an enhanced redox activity of AIF.

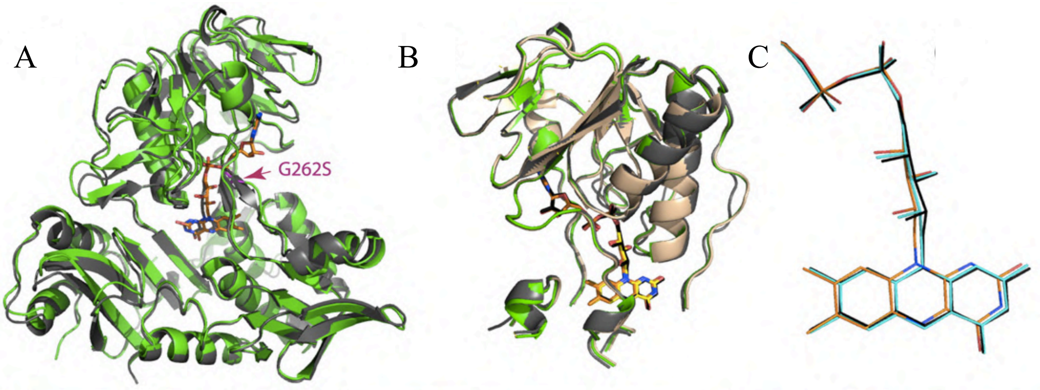

**Fig. 1.11 Structural changes induced by the G262S mutation.** (**A**) Superposition of the wild type (4BV6) and G262S AIF structures (shown in gray and green, respectively), with the mutation site indicated by an arrow. A notable (~1.0 Å) shift in the isoalloxazine portion of FAD is due to a slightly distinct domain-domain orientation in wild type AIF caused by different crystal packing. (**B**) Superposition of the active sites/FAD-binding domains of wild type (gray), G262S (green), and V243L AIF (beige). The V243L mutant was used for comparison because it crystallizes in the same space group and, overall, is structurally more similar to AIF G262S than wild type. (**C**) The FAD conformation in wild type, V243L, and G262S AIF (shown in black, cyan, and orange, respectively). Only a part of the flavin is displayed to better show a ~0.2 Å distortion in the isoalloxazine/ribitol portion caused by the G262S mutation (Sevrioukova *et al.*, 2016).

# 2. Aim of the project

The present PhD project was focused on the study of an FAD-dependent mitochondrial flavoprotein, the mitochondrial Apoptosis Inducing Factor (AIF) and its recently discovered interaction with the mitochondrial protein CHCHD4. Upon different apoptotic stimuli, AIF can be released from mitochondria and translocated to the nucleus where it promotes chromatin condensation and large scale DNA degradation, acting as the main mediator in caspase-independent cell death program. Beside its well characterized lethal role, there are many evidences of AIF role in maintaining proper mitochondrial morphology and oxidative phosphorylation (OXPHOS). In this context, the formation of an air-stable CT complex between AIF and NAD(H), linked to protein dimerization, seems to play a pivotal role. However, although many efforts to analyze AIF pro-survival role during the last years, the molecular mechanism of this AIF function remains largely unclear . Recently, it was discovered that AIF interacts and modulates the activity of another mitochondrial protein known as CHCHD4, involved in the import and assembly of respiratory complexes subunits. This finding provided for the first time a clear connection between AIF and OXPHOS and shed new light on the AIF vital role. Furthermore, nine distinct point mutations of the *AIFM1* gene, localized on the X chromosome in humans and mice, were found to cause severe mitochondriopathies, with neurodegeneration as a common feature. Some of these pathogenic variants of the flavoprotein were biochemically characterized and well defined alterations in AIF molecular properties were associated with the neurodegenerative disorders they caused. However, some mutants still lack a through biophysical characterization while in some instances their structural/biochemical characterization didn't reveal a clear connection with the pathological consequences.

Therefore, the aim of the present PhD project was the structural and biochemical characterization of relevant pathogenic allelic variants of murine AIF, carrying the equivalent amino acyl substitution (D236G, G337E, G261S and F133L) of the human one, aimed to investigate possible alterations in their biochemical properties, with a particular focus on the pivotal interaction with murine CHCHD4. During this PhD project, we produced and purified the above mentioned murine variants of AIF. We set up and optimized aa production and purification protocol for recombinant mouse CHCHD4, and performed its base characterization. Next, we optimized some novel techniques to study the interaction between AIF and its protein partner, with a particular focus on MicroScale Thermophoresis, through which we were able to quantitatively measure the strength of the interaction.

In addition, we performed several crystallization trials in order to gain structural information on the wild type AIF-CHCHD4 complex, although without success, probably because of the intrinsic disorder of CHCHD4. To overcome this problem, we decided to investigate the complex structure by Small-Angle X-ray Scattering, obtaining for the first time the identification of a putative region of the AIF interacting with CHCHD4.

# 3. Results and discussion

## 3.1 AIF and CHCHD4 production and purification

### 3.1.1 Production and purification of apoptogenic variants of murine AIF

Since murine protein shares about 92% sequence identity with human AIF, and can be easily purified with large yields in recombinant form[6], in order to investigate at the molecular level the effects of the D237G, G338E, G262S and F134L replacements, we engineered these substitutions at the equivalent position (D236G, G337E, G261S and F133L, respectively) of the murine apoptogenic form (AIFΔ1-101). To introduce the four amino acyl replacements in mouse AIF, we adopted a site-directed mutagenesis approach using the expression vector containing the wild type coding sequence fused with a sequence encoding a C-terminal His-tag as the template (pKK-AIFΔ1-101). In particular, we used the QuikChange® Lightning Site-Directed Mutagenesis Kit (Agilent) with specifically designed couples of complementary oligonucleotide primers. We produced in recombinant form and purified the four AIF variants according to the protocols already set up for the wild type protein[10]: it consists of protein overexpression in *E. coli* BL21(DE3) cells, cell disruption to obtain the crude extract, a capturing step based on $Ni^{2+}$-affinity chromatography and a final polishing step consisting of anion-exchange chromatography. All chromatographic steps were performed using an ÄKTA-FPLC system (GE Healthcare). The four AIF variants were large-scaled purified with very similar yields with respect to the wild type form (about 20 mg of protein per 1 L of cell culture) and with high purity.

### 3.1.2 Production and purification of murine CHCHD4

Using as expression vector a construct obtained by the insertion of the mouse CHCHD4 coding sequence into the pET-21a(+) vector, we explored protein expression under different growth temperatures and inducer concentrations, in three different *E. coli* strains: BL21(DE3), SHuffle® and Rosetta(DE3). The SDS-PAGE analysis shown in Fig. 3.1, showed that, while CHCHD4 production was not detectable in BL21 cells, in the other two strains a band compatible with a protein with an apparent molecular mass lower than 20 kDa appeared after IPTG induction in comparison with not induced (NI) samples. CHCHD4 is known to contain three intramolecular disulfide bonds. Thus, to favor the production of correctly organized CHCHD4, the SHuffle® strain (an engineered *E. coli* strain that promotes disulfide bond formation in the cytoplasm) was used.

In a typical cell growth performed at 25 °C overnight, 10 g of cells were collected from 5 L culture medium. Cell were resuspended in two volumes of buffer A (50 mM Tris-HCl, pH 8.0, 200 mM NaCl, 10 mM Imidazole added with 1 mM PMSF), and disrupted by sonication.

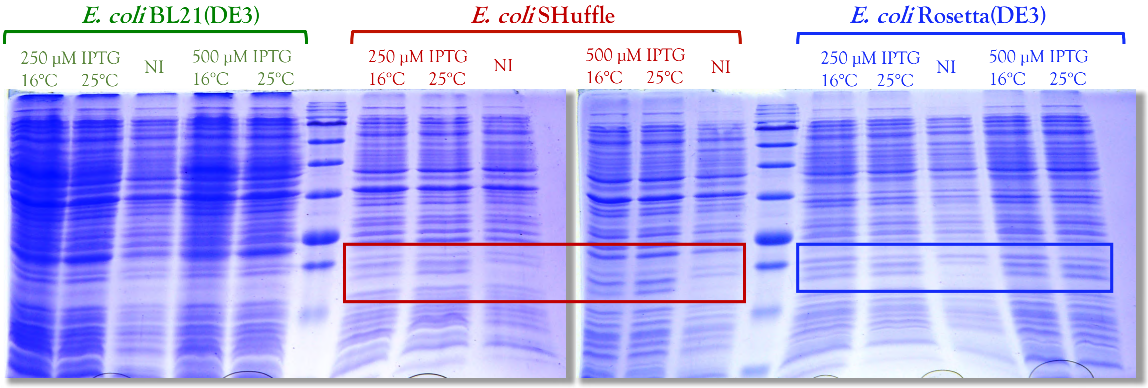

**Fig. 3.1 SDS-PAGE analysis of CHCHD4 expression trials.** BL21(DE3), Rosetta(DE3) and SHuffle® *E. coli* strains were used to test CHCHD4 expression at different IPTG concentration and temperature. NI lane: not induced sample.

The purification protocol that we set up consisted of three main steps. At first, we exploited a $Ni^{2+}$-affinity chromatography to separate CHCHD4 from the majority of contaminants of the crude extract, using two HisTrap HP columns (GE Healthcare) 5 ml each, equilibrated with buffer A. The gradient elution was performed reaching 100% of buffer B (50 mM Tris-HCl, pH 8.0, 200 mM NaCl, 500 mM Imidazole) in 10 column volumes (Fig. 3.2A). Unexpectedly, the fractions analyzed through SDS-PAGE in the absence of reductant agents revealed that CHCHD4 was purified as a mixture of both monomeric and dimeric form of the protein (Fig. 3.2B). While CHCHD4 is expected to exist under physiological conditions in monomeric form[26], it is feasible that its high concentration reached in a bacterial system that promotes disulfide bond formation could favor the formation of intermolecular disulfide bond(s), thus leading to dimerization, possibly through its N-terminal free Cys residue.

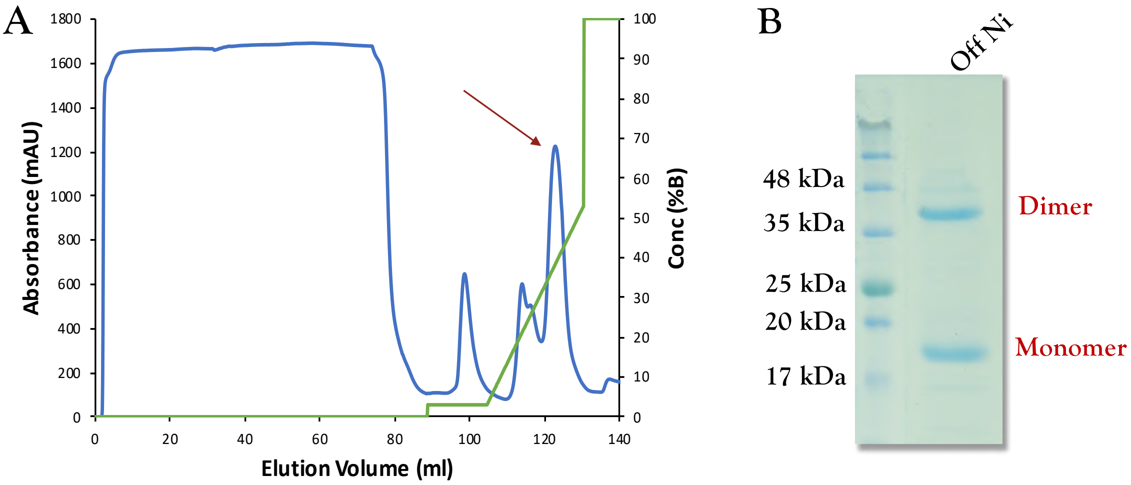

**Fig. 3.2 $Ni^{2+}$-affinity chromatography profile and SDS-PAGE analysis.** (**A**) The chromatogram shows CHCHD4 elution, whose peak is highlighted with a red arrow. (**B**) Subsequent SDS-PAGE analysis in the absence of reductant agents shows that CHCHD4 was isolated as a mixture of both dimer and monomer.

Thus, with the aim to obtain the protein as a monomer, we analyzed the effect of the reductant agent DL-dithiothreitol (DTT) on CHCHD4 aggregation state by analytical size-exclusion chromatography (SEC) using a Superdex 75 10/300 GL column (GE Healthcare). We performed SEC analyses in GF buffer (50 mM Tris-HCl, pH 8.0, 200 mM NaCl) either in the absence of reductant or after incubation for 1 h with 2 mM DTT (Fig. 3.3A, orange and light blue, respectively). The superposition of the two SEC chromatograms shows that, in the absence of DTT, the amount of CHCHD4 dimer and monomer is comparable. Moreover, species at higher molecular weights were detected, probably representing contaminants and/or higher oligomerization states of CHCHD4. In contrast, after incubation with DTT, CHCHD4 is present mostly in a monomeric form, suggesting that the non-physiological oligomerization was driven by intermolecular disulfide bond formation. To evaluate the molecular weight of the protein in the presence of DTT, we constructed a calibration curve using protein standards as reference, which yielded an estimated molecular mass for the recombinant protein of about 35 kDa, a value significantly higher than expected. This effect was probably due to the lack of a precise folding of the protein N- and C-terminal regions, described as highly flexible and/or disordered and thus resulting in a high hydrodynamic radius for the protein molecule.

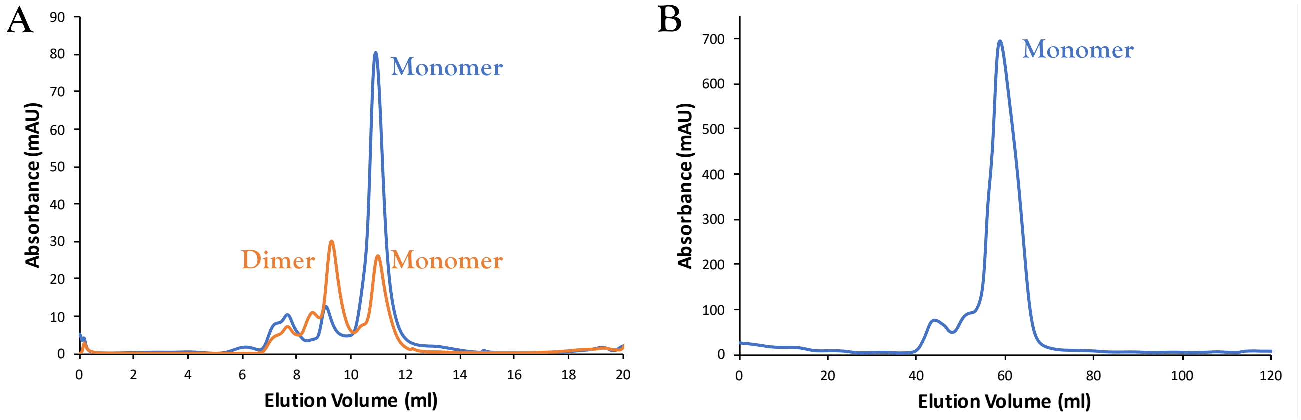

**Fig. 3.3 Analytical and preparative SEC**. (**A**) Analytical SEC performed either in the absence or in the presence of 2 mM DTT (orange and light blue chromatograms, respectively). (**B**) Preparative SEC in the presence of 2 mM DTT exploited to further remove contaminants and purify CHCHD4 as a monomer.

The second purification step consisted on a preparative SEC in the presence of 2 mM DTT using a HiLoad Superdex 75 16/600 pg column (GE Healthcare), through which we were able to remove a large part of high molecular weights contaminants and to obtain an almost pure protein in monomeric form (Fig. 3.3B). Despite the effectiveness of the SEC, a small amount of contaminants was still present in the purified preparation (Fig. 3.4B, SEC lane). Thus, we decided to perform an additional purification step. In details, the C-terminal His-tag of CHCHD4 was removed through thrombin digestion, and the treated protein was further separated through a second $Ni^{2+}$-affinity chromatography, using an HisTrap HP column (GE Healthcare). Untagged CHCHD4 was recovered in the column flow-through using buffer A, while contaminants were eluted with 50% of buffer B (Fig. 3.4A). As shown in lane Thrmb of Fig. 3.4B, by this final step we removed the majority of contaminants obtaining highly pure CHCHD4 , with a total final yield of 1.25 mg protein per gram of cells.

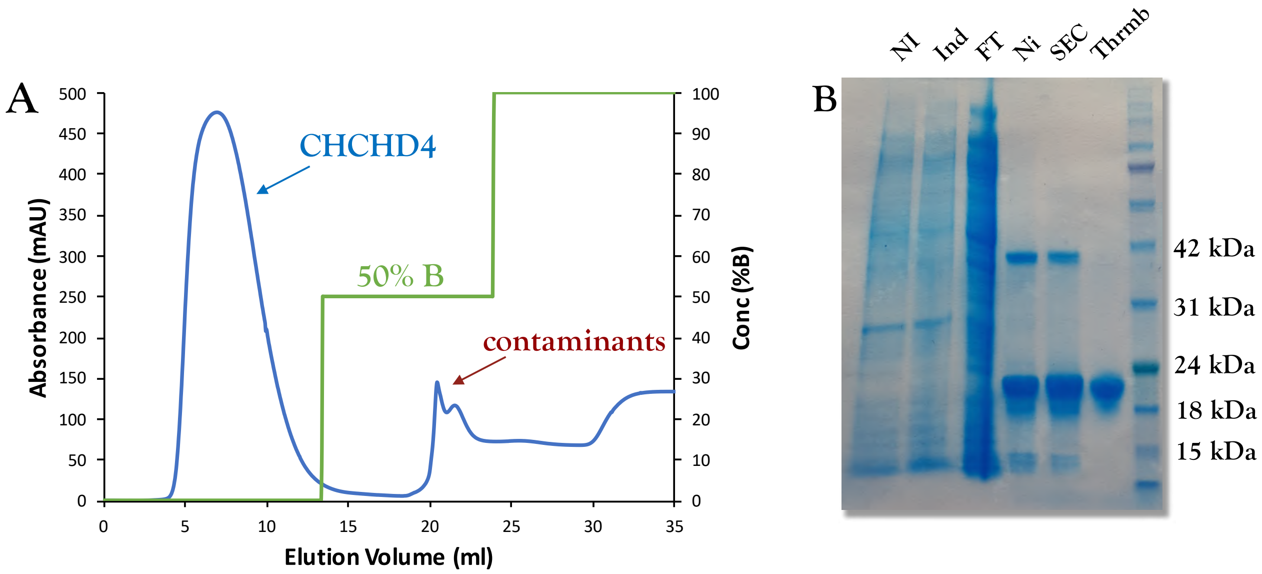

**Fig. 3.4 Thrombin cleavage and Ni$^{2+}$-affinity chromatography**. (**A**) Chromatogram showing a Ni$^{2+}$-affinity chromatography after thrombin cleavage of CHCHD4 His-tag. (**B**) SDS-PAGE of the entire purification process: NI (not induced), Ind (after IPTG induction), FT (flow through), Ni (Ni$^{2+}$-affinity chromatography), SEC (size exclusion chromatography), Thrmb (Ni$^{2+}$-affinity chromatography performed after thrombin cleavage).

## 3.2 Basic molecular characterization of murine AIFΔ1-101 forms

We investigated possible alterations in the conformational stability of AIF induced by the replacements using the ThermoFAD technique, as previously reported[39]. ThermoFAD relies on the fact that unfolding of a flavoprotein expose its flavin prosthetic group, usually resulting in a large increase of its fluorescence quantum yield. By recording the fluorescence emission of the sample at increasing temperature values it is possible to obtain a denaturation profile and to assess the thermal stability of the protein itself[40]. The results of the analysis revealed a slightly decreased conformational stability for the G337E variant in its monomeric oxidized state, corresponding to a melting temperature lower than that of the wild type protein by 2 °C. A more marked destabilization of 6 °C was observed in the presence of a NADH excess (Table 1), suggesting that the mutation could alter the conformation of the CT complex state of AIF. Moreover, we found that the effect of the G261S mutation was a decrease of 3 °C of the thermal stability of the protein in the oxidized/monomeric state. Instead, inclusion of NADH resulted in a biphasic thermal denaturation profile, showing two different melting temperature values, of 47 °C and 57 °C, respectively (Fig. 3.5). The two peaks were interpreted as the unfolding of the oxidized protein (57 °C) and its CT complex state (47 °C). This imply that the G261S variant, even in the presence of a NADH excess, is not able to form a stable CT complex, which, during the temperature ramp, partially reverted into the oxidized form of the protein.

The ThermoFAD technique did not revealed alterations in the thermal stability of the D236G and F133L mutants, in both the oxidized and reduced state, whose melting temperature values were very similar to that obtained for the wild type protein.

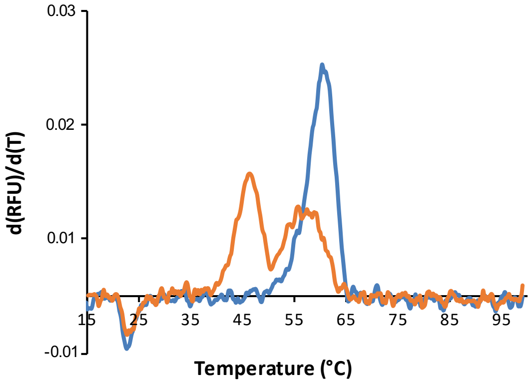

**Fig. 3.5 Conformational stability of the AIF G261S mutant.** In the oxidized state the mutant showed a melting temperature value close to the oxidized wild type one (light blue curve) while, in the presence of NADH excess, two different values of melting temperature were detected (orange curve), one consistent with the oxidized form of the protein (57 °C) and the other with its reduced form (47 °C).

| AIF | $T_m^{OX}$ (°C) | $T_m^{RED}$ (°C) |
|---|---|---|
| Wild type | 63.8 ± 0.1 | 55.4 ± 0.2 |
| G337E | 61.8 ± 0.2 | 49.4 ± 0.1 |
| G261S | 60.1 ± 0.2 | 47 - 57 ± 0.3 |
| D236G | 63.8 ± 0.1 | 57.2 ± 0.1 |
| F133L | 62.0 ± 0.1 | 52.0 ± 0.1 |

**Table 1. AIF forms melting temperatures measured through the ThermoFAD technique.**

## 3.3 Characterization of CT complexes engaged by AIF forms with NAD(H)

### 3.3.1 Effect of pathogenic mutations on AIF CT complex formation with NAD$^+$

All photoreduced AIF forms were able to form charge-transfer (CT) complexes when mixed with NAD$^+$, displaying spectral features very similar to those of the wild type protein. However, despite the anaerobic conditions, in the case of the G261S mutant, a lower CT complex species accumulation was observed (Fig. 3.6B) under equilibrium conditions, as monitored by the absorbance at 750 nm (Fig. 3.6A). This indicate that the G261S replacement caused a moderate disruption of the protein-NAD$^+$ interactions generating the CT complex (*see* § 3.2).

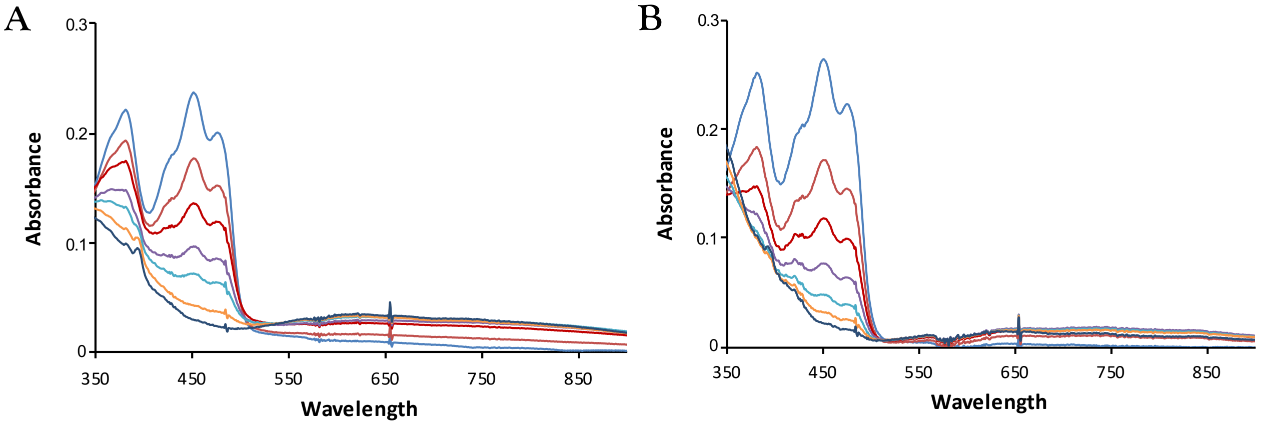

**Fig. 3.6 CT complex formation between AIF forms and NAD$^+$ upon anaerobic photoreduction.** Anaerobic solutions of 15 µM AIF forms containing 20 µM NAD$^+$ were progressively photoreduced and their spectra were recorded at different stages of FAD reduction. (**A**) Reduction of wild type AIF in the presence of NAD$^+$. (**B**) Reduction of G261S mutant in the presence of NAD$^+$.

### 3.3.2 Effect of pathogenic mutations on AIF CT complex reactivity towards $O_2$

It is known that AIF CT complex engaged with NAD(H) is very air-stable. Moreover, the G261S and the G337E mutant were found to possess a decreased conformational stability, in particular in their reduced CT complex states. Thus, we decided to investigate the effect of the four AIF mutations on the $O_2$-reactivity of their AIF(FADH$^-$)-NAD$^+$ CT complexes. For each mutant, a 100 µM AIF solution was incubated with 1 mM NADH for 30 min (to allow complete CT complex formation), then excess of NADH was removed through a PD MidiTrap G-25 (GE Healthcare) and CT complexes reoxidation was monitored spectrophotometrically at both 452 nm and 750 nm.

Our results (Fig. 3.7 and Table 2) clearly showed an 8-fold faster reoxidation of the CT complex engaged by the G337E mutant with respect to the wild type AIF, confirming that the G337E replacement significantly destabilizes the CT complex species, as previously suggested by the ThermoFAD analysis. We detected a more drastic alteration in the CT complex reactivity in the G261S mutant. In this case, the enzyme was completely oxidized a few seconds after the removal of the NADH excess, indicating that this mutation greatly enhances the CT complex reaction with molecular oxygen. A largely unstable CT complex could be correlated to a significant impairment of the pro-vital functions carried out by AIF inside mitochondria, in particular its pivotal interaction with CHCHD4, providing a possible explanation for the onset of the AIF G261S-linked mitochondriopathy.

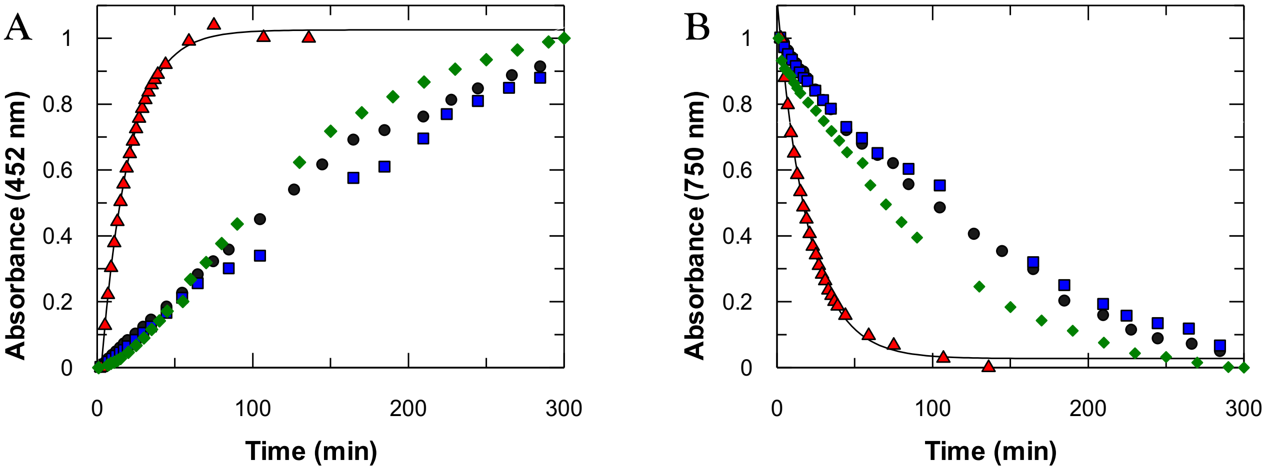

**Fig. 3.7 AIF forms CT complex stability towards $O_2$.** Upon removal of NADH excess, CT complex reoxidation was spectrophotometrically monitored at 452 nm for oxidized AIF (**A**) and at 750 nm for AIF in the CT complex state (**B**). AIF variants D236G, F133L, G337E and the wild type protein are shown in blue, green, red and black, respectively.

| AIF | t/2 (min) |
|---|---|
| Wild type | 125 |
| G337E | 15 |
| G261S | < 1 min |
| D236G | 140 |
| F133L | 120 |

**Table 2. Half-life of AIF forms CT complex upon NADH removal.**

## 3.4 Effect of the pathogenic mutations on AIF redox activity

It is known that AIF is able to catalyze electron transfer from NADH to 2,6-dichlorophenolindophenol (DCIP), an artificial acceptor, with a modest but significant turnover[10]. In order to investigate possible alterations of AIF redox properties induced by pathogenic mutations, we have determined the kinetic parameters of the NADH-DCIP diaphorase reaction under steady-state conditions, as previously reported[39]. It is important to underscore that the rate-limiting this reaction is the reductive half-reaction in which AIF is reduced by NADH to generate the CT complex. Thus, the kinetic parameters obtained can be considered a quantitative description of the CT complex formation process. Our results (Fig. 3.8 and Table 3) show that the D236G and the G261S did not lead to significant changes in the kinetic parameters of this reaction, which appeared very similar to those obtained for the wild type protein.

Instead, the G337E mutation leads to a slight alteration of both $k_{cat}$ and $K_M$ of AIF for the reaction, which, in comparison to the wild type protein, resulted 3-fold decreased and 2-fold increased, respectively. Although the F133L replacement is located at the very N-terminal portion of AIF and far from the NADH-binding site, we detected a 3-fold increased value of $K_M$ with respect to the wild type protein. Finally, the G337E and the F133L replacements were not found to significantly affect the AIF enzymatic properties, showing comparable parameters in comparison to the wild type protein.

Interestingly, even if the G261S mutation was found to alter CT complex state, it did not cause significant perturbations of the redox activity of the protein in the presence of excess NADH, showing that the mutation does not prevent CT complex formation, but rather it specifically affects its stability towards $O_2$.

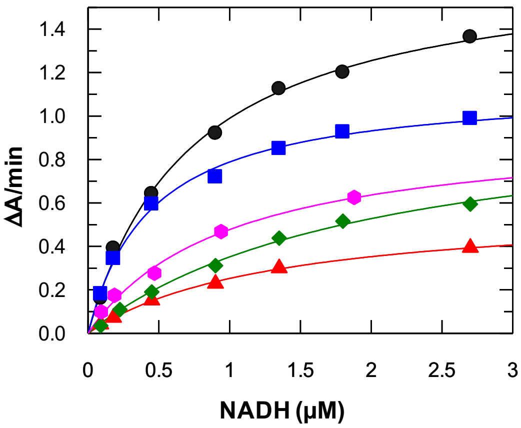

**Fig. 3.8 NADH-DCIP diaphorase reaction catalyzed by AIF forms.** Kinetics data of the D236G, G261S, F133L, G337E and wild type AIF were collected following DCIP reduction (600 nm) and are depicted in blue, pink, green, red and black, respectively.

| **AIF** | $k_{cat}$ ($s^{-1}$) | $K_m$ (mM) | $k_{cat}/K_m$ ($mM^{-1}s^{-1}$) |
|---|---|---|---|
| Wild type | 1.31 ± 0.04 | 0.73 ± 0.07 | 1.80 ± 0.20 |
| G337E | 0.43 ± 0.01 | 1.32 ± 0.08 | 0.33 ± 0.03 |
| G261S | 0.69 ± 0.06 | 1.00 ± 0.20 | 0.69 ± 0.20 |
| D236G | 0.75 ± 0.02 | 0.44 ± 0.04 | 1.71 ± 0.20 |
| F133L | 0.84 ± 0.06 | 2.01 ± 0.19 | 0.42 ± 0.07 |

**Table 3. AIF forms kinetic parameters.**

## 3.5 Effect of pathogenic mutations on AIF dimerization

AIF dimerization occurs through a large conformational reorganization of the flavoprotein linked to CT complex formation. This process is proposed to be pivotal in the signal-transduction pathway in which the protein would be involved, especially in the interaction with its partner protein CHCHD4. We therefore investigated the possible impact of the AIF pathogenic mutations on its ability to dimerize, by means of two different techniques: analytical size exclusion chromatography (SEC) and Dynamic Light Scattering (DLS). SEC experiments showed that all AIF forms were able to dimerize after incubation with 1 mM NADH, being their calculated molecular weights comparable with that of the dimeric form of wild type AIF.

To validate analytical SEC results, we investigated the dimerization process of the AIF forms also by Dynamic Light Scattering (DLS) measurements. Again, upon AIF incubation with 1 mM NADH, the hydrodynamic radius values obtained for all tested AIF forms were similar to that obtained for the wild type protein in the dimeric form.

In summary, analytical SEC experiments and DLS measurements confirmed that all mutated proteins are able to dimerize in the presence of a large NADH excess similarly to the wild type AIF, suggesting that none of the pathogenic replacements abolished this essential process (*see* § 5: Materials and Methods for further information about Analytical SEC and DLS measurements). This conclusion is in agreement with the localization of all mutated sites far away from the AIF dimerization interface.

## 3.6 Crystallization trials on the pathogenic AIF variants

Given the very similar biochemical features of all tested AIF mutants with respect to the wild type protein we decided to investigate possible alterations in their structures through a crystallographic approach. Crystallization trials were performed by both sitting drop and microbatch techniques, in which all AIF mutants were at a final concentration of 300 µM (18 mg/ml) in the absence or in the presence of 5 mM NADH. Crystals obtained under different crystallization conditions, both in sitting drop and in microbatch, in reduced and oxidized forms (Fig. 3.9), drowned from the drop and immersed into a cryo-protectant solution similar to crystallization condition but containing 20% glycerol and frozen in liquid nitrogen, were tested at the ESRF (European Synchrotron Radiation Facility in Grenoble, France). Although the majority of tested crystals showed very low propensity to diffract, we were able to obtain diffraction data of the reduced F133L variant at 2.2 Å resolution (Fig. 3.10 and Table 4) and, although at a lower resolution, of the oxidized F133L and D236G mutants (at 3.2 and 3.5 Å, respectively). However, superimposition of the F133L mutant structure in the reduced form to that of the wild type protein (PDB 3GD4[41]) did not revealed any significant conformational change (RMS value of 0.8) that could be linked to pathology onset. This result suggests that the mutation may affect the protein dynamic rather than cause local conformational changes in its three-dimensional structure. The resolution limit of the F133L mutant in the oxidized state and the D236G mutant in the reduced state was too low to make any consideration at atomic resolution level.

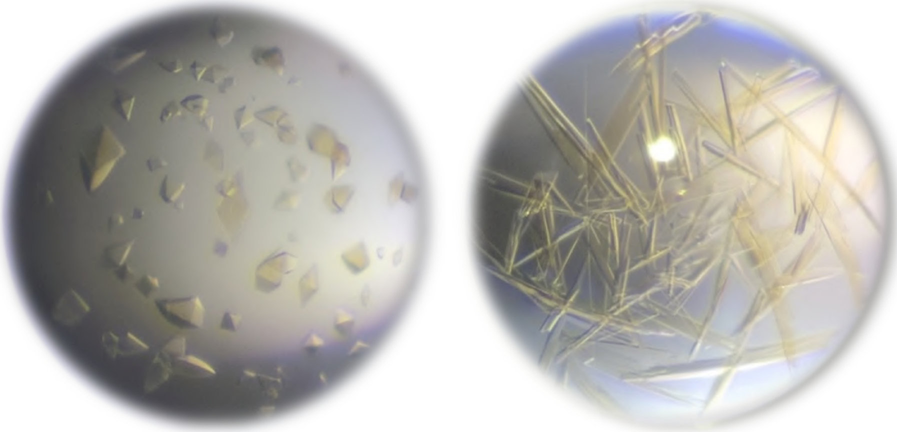

**Figure 3.9 AIF crystals obtained during crystallization trials.**

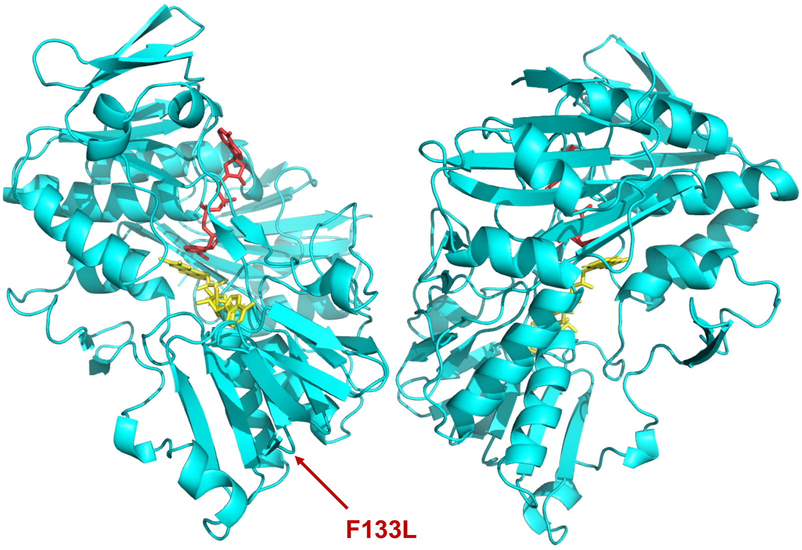

**Fig. 3.10 Crystal structure of the F133L mutant in the reduced form obtained at a 2.2 Å resolution.** The F133 residue is indicated by the red arrow, while FAD and NADH are depicted in yellow and red, respectively.

| AIF variant | Resolution (Å) | R | $R_{free}$ | RMSD bonds (Å) | RMSD angles (°) |
|---|---|---|---|---|---|
| F133L | 2.2 | 0.21 | 0.24 | 0.008 | 1.34 |

**Table 4. Summary of the reduced AIF F133L mutant structural parameters.** $R_{work} = \Sigma_{hkl}||Fo| - |Fc|| / \Sigma_{hkl}|Fo|$ for all data, except 5-10%, which were used for $R_{free}$ calculation.

## 3.7 Molecular characterization of murine CHCHD4

As previously described in § 3.1.2, analytical SEC revealed that CHCHD4 hydrodynamic radius was more consistent with a dimeric or partially disordered or elongated state of the protein than with a compact globular monomeric one. Thus, we decided to further investigate the CHCHD4 molecular organization through the Dynamic Light Scattering (DLS) technique. The DLS data showed a protein polidispersion (Pd) of 16 % and an estimated molecular weight of 50 kDa, a value that is consistent with a dimeric form of the protein, possibly suggesting as an alternative that the CHCHD4 molecule is flexible and elongated, features that are compatible with a hydrodynamic value higher than expected. Subsequently, to further characterize the molecular features of CHCHD4, we investigated its secondary structure and conformational stability by the Circular Dichroism (CD) technique. CD is a tool for rapid determination of the secondary structure and folding properties of proteins, and – by monitoring the CD signal of the target protein at different temperatures – it can provide information about their conformational stability. Protein structural elements displays characteristic CD spectra. α-helical proteins show negative bands at 222 nm and 208 nm and a positive band at 193 nm while proteins with antiparallel β-pleated sheets have negative bands at 218 nm and positive bands at 195 nm[42].

In Fig. 3.11A the CD spectra of CHCHD4 before and after denaturation as well as that obtained after renaturation are depicted in blue, red and green, respectively.

The spectrum before denaturation (blue spectrum) presents typical peaks attributable to α-helical secondary elements with no β-sheets.

This result is in agreement with the known structural features of CHCHD4, which possess essentially three α-helices while the rest of the protein does not adopt any definite secondary structure. After denaturation (red spectrum), α-helical signals are still present, although attenuated, suggesting a high persistence of CHCHD4 secondary structure. Finally, the renaturation process did not fully regenerated the original spectrum, suggesting that the native conformation was not completely regained. This behavior is probably due to the impossibility to properly form the intramolecular disulfide bonds lost during the denaturation process. In Fig. 3.11B the denaturation curve obtained after temperature ramp is reported, showing a melting temperature value close to 70 °C. The plot also indicates that, at 95 °C the protein could be not completely denatured, confirming that CHCHD4 possesses a high resistance to thermal denaturation.

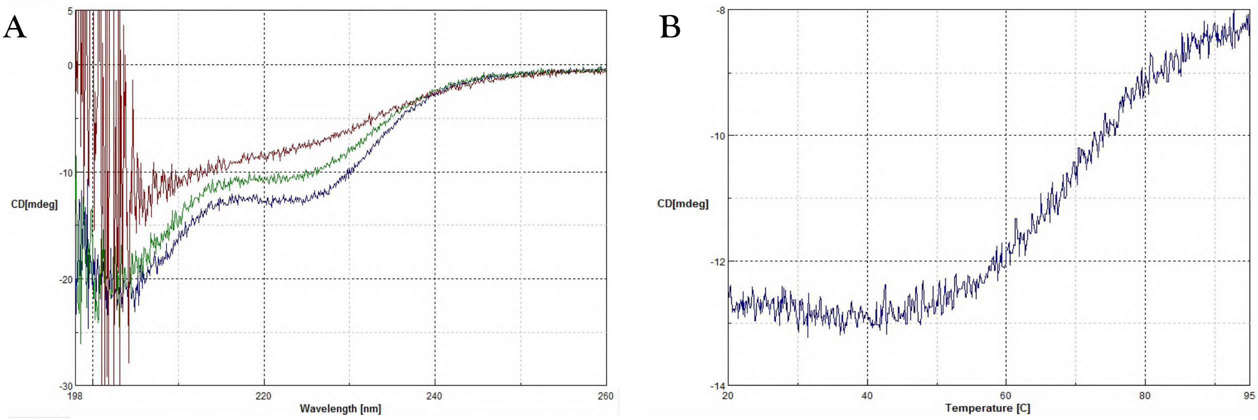

**Fig. 3.11 Analysis of CHCHD4 through Circular Dichroism (CD).** (**A**) CD spectra before and after denaturation and that of the renatured protein are shown in blue, red and green, respectively. (**B**) Denaturation curve monitored at 220 nm showed a melting temperature of about 70 °C.

## 3.8 AIF-CHCHD4 complex characterization

As the biochemical and biophysical characterizations of the four isolated pathogenic AIF mutants did not reveal a clear cause for the pathogenic effect of the respective replacement, we focused our attention on the recently discovered interaction between AIF and CHCHD4[9]. Our goal was to identify possible alterations of this essential interaction induced by AIF mutations, providing a possible molecular base for these disease-causing mutations. In a more general perspective, results of this study would provide important new information on the AIF-CHCHD4 interaction, which is still poorly characterized.

### 3.8.1 Interaction of AIF with CHCHD4

As a first approach, complex formation between AIF and CHCHD4 was investigated by analytical SEC. For this analysis wild-type AIF, in both its oxidized and reduced state, was incubated in the absence or in the presence of CHCHD4 in small excess. Fig. 3.12A reports the superposed chromatograms of the oxidized/monomeric AIF alone and incubated with CHCHD4 (light blue and orange traces, respectively).

As it can be seen, the significant shift of about 500 µl induced by the presence of CHCHD4 in the elution volume of AIF suggests that the interaction between the two proteins occurred, yielding a relatively tight, long-lived complex that persisted during the separation.

The experiment was performed also using AIF pre-incubated with NADH, to induce its CT complex/dimeric state. The superposed chromatograms of reduced AIF alone and reduced AIF incubated with CHCHD4 (light blue and orange, respectively) are reported in Fig. 3.12B.

In this case, a larger shift of about 1 ml in the elution volume was detected, confirming that also the reduced/dimeric AIF is able to interact with its partner protein.

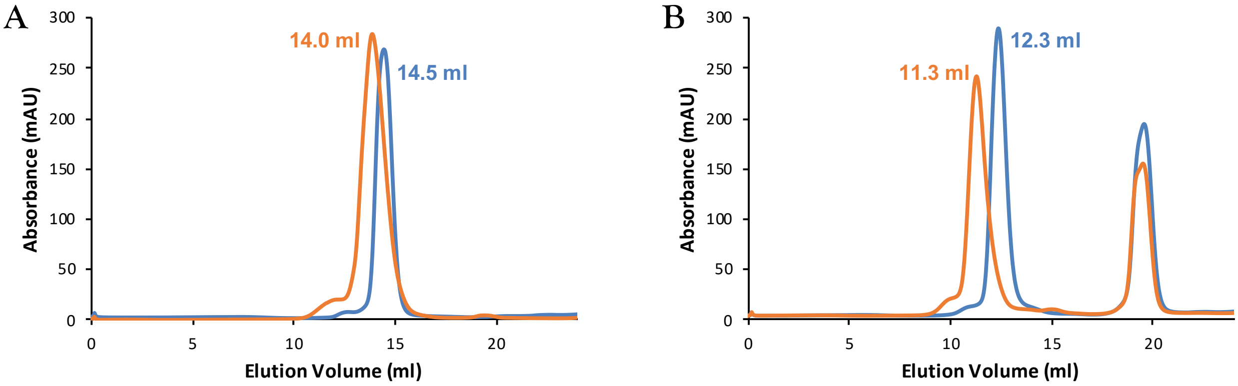

**Fig. 3.12 Analytical SEC experiments on wild type AIF-CHCHD4 interaction.** (**A**) Superposed chromatograms of oxidized AIF (light blue) and oxidized AIF in complex with CHCHD4 (orange). (**B**) Superposed chromatograms of reduced AIF (light blue) and reduced AIF in complex with CHCHD4 (orange). Elution volumes are reported close to the corresponding peak.

### 3.8.2 Effect of CHCHD4 binding on AIF conformational stability

Analytical SEC experiments showed that the two proteins are able to form a complex, thus we decided to investigate possible alterations induced by CHCHD4 binding on the conformational stability of AIF, both in the oxidized and reduced states, by the ThermoFAD technique. The ThermoFAD was performed as described for AIF variants alone (*see* § 5: Materials and Methods). The denaturation profiles of oxidized AIF alone and incubated with CHCHD4 are reported in Fig. 3.13A (in blue and orange, respectively). The results clearly show that CHCHD4 binding significant destabilizes AIF, whose melting temperature resulted 8 °C lower. Interestingly, the lower stability upon CHCHD4 binding is comparable to that induced by NADH binding, suggesting that AIF undergoes important conformational changes when it is engaged in this protein-protein complex. In contrast, no effect of CHCH4 binding on the thermal stability of AIF was detected when it was in the reduced/dimeric state (Fig. 3.13B). From these observations, it could be concluded that, while CHCHD4 binding induces a large conformational rearrangement of monomeric AIF, it leaves the structure of the dimeric form of the protein essentially unaffected.

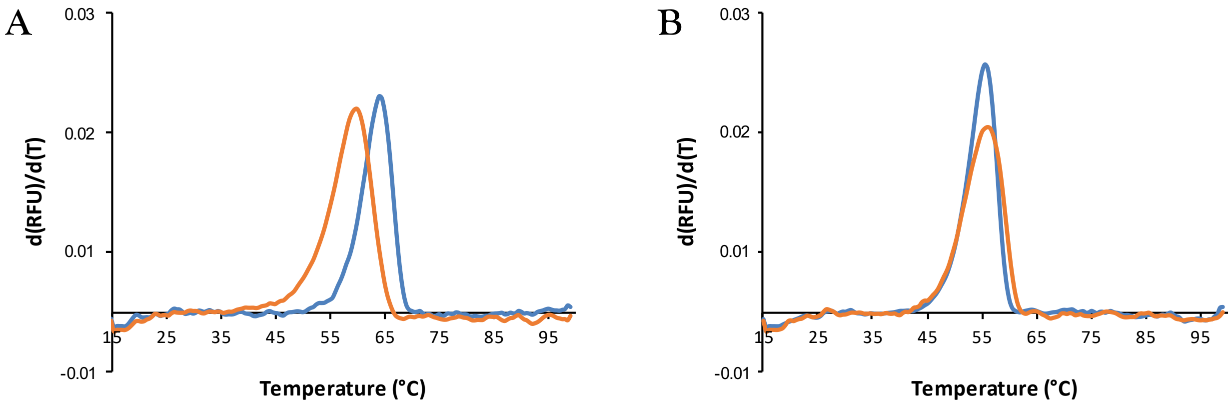

**Fig. 3.13 Effect of CHCHD4 binding on AIF conformational stability.** (**A**) Thermal denaturation profiles of oxidized AIF and oxidized AIF incubated with CHCHD4 are represented in light blue and orange, respectively. (**B**) Thermal denaturation profiles of reduced AIF and reduced AIF incubated with CHCHD4 are represented in light blue and orange, respectively.

### 3.8.3 MicroScale Thermophoresis (MST)

Once that the ability of wild type AIF and CHCHD4 to form a complex was ascertained, we decided to measure the strength of such interaction on a quantitative basis by using a MicroScale Thermophoresis (MST) approach. The technique is based on the measure of the concentrations of ligand-free and ligand bound forms of the target protein in solution through the record of the fluorescence emission intensity of sample mixtures. MST requires that the target protein is intrinsically fluorescent or labelled with an appropriate dye, with the samples confined within glass capillaries that protect them from air exposure. Briefly, MST detects changes in the hydration shell of molecules and measures biomolecule interactions under close-to-native conditions. Infrared-lasers are used to achieve precise microscale temperature gradients within thin glass capillaries that are filled with a solution of choice and molecules move along these temperature gradients. Hydration shell variations of biomolecules due to changes in their primary, secondary, tertiary and/or quaternary structure affects the thermophoretic movement and is used to determine binding affinities with high accuracy and sensitivity[43,44]. In our case, we labeled AIF at the level of its His-tag at its C-terminus through a non-covalent linkage, a site not expected to affect the conformation of the protein. In Fig. 3.14A the capillary scan of CHCHD4 titration of wild type AIF in its oxidized/monomeric state is reported, showing that protein-protein interaction induced no fluorescence quenching, while it was clearly detected a ligand dose-dependent thermophoresis effect from the recorded MST traces (Fig. 4.14B). Interpolation of MST data (Fig. 3.14C) yielded a $K_d$ value of 13 ± 2 µM for AIF in the oxidized state.

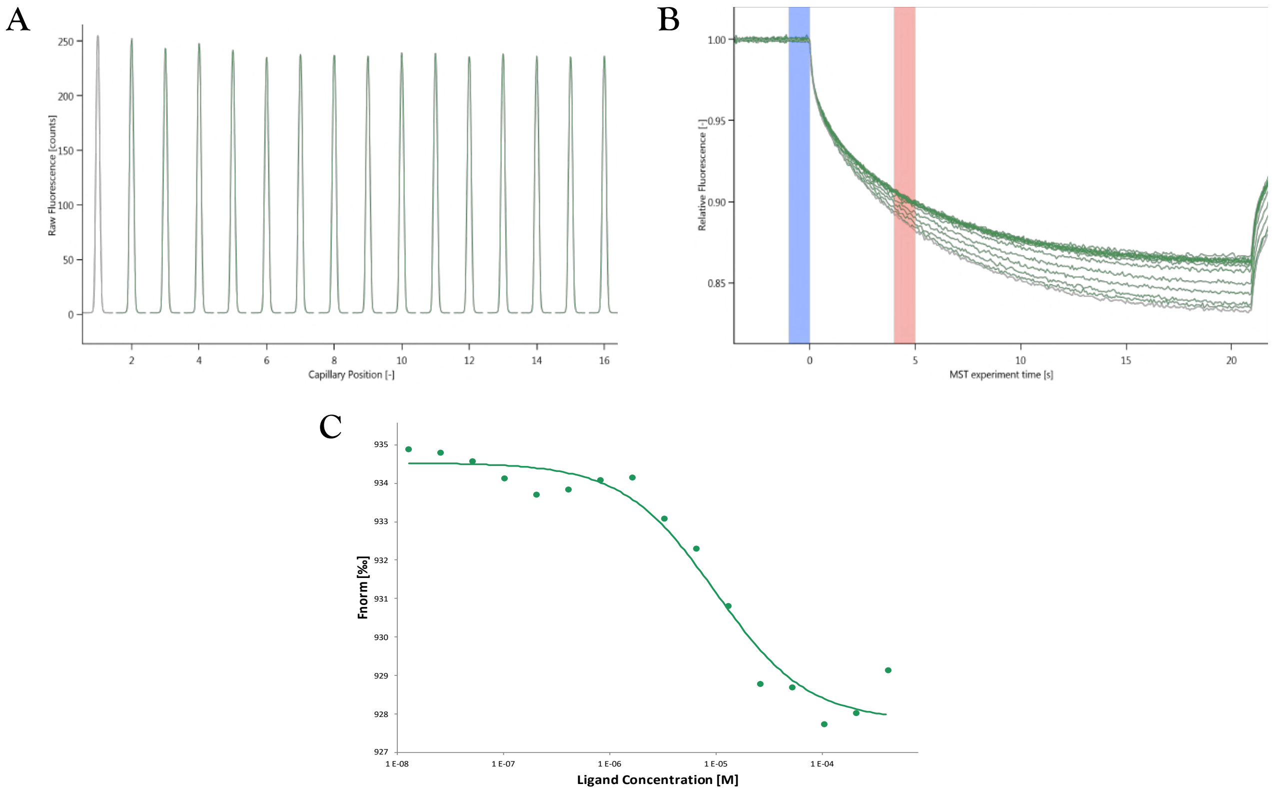

**Fig. 3.14 MicroScale Thermophoresis on wild type AIF in the oxidized form in complex with CHCHD4.** (**A**) Capillary scan showed constant initial fluorescence along all MST samples. (**B**) MST traces. From light blue interval was measured initial fluorescence intensity during capillary scan while the salmon red interval represents the region where the thermophoretic effect was exploited for $K_d$ calculation. (**C**) Interpolation of MST fluorescence data from which a $K_d$ of 13 ± 2 µM was estimated.

The same experiment was performed in the presence of a NADH excess, thanks to which AIF adopts a homodimeric quaternary structure. However, in this case a significant enhancement in fluorescence emission induced by ligand binding was detected from the capillary scan (Fig. 3.15A), suggesting a change in the fluorophore environment caused by the protein-protein interaction. Thus, according to manufacturer instructions, we performed an EDTA/His6-peptide (ECP) test, through which ligand-induced fluorescence changes while using dye-tris-NTA labeling can be quantified. This control procedure includes two sub-tests that must be performed to unambiguously distinguish between fluorescence changes caused by actual protein-ligand interactions from those caused by a non-specific quenching action of the ligand. The latter includes the interaction of the ligand with the dye (control peptide test) or the ligand-induced aggregation of the target protein or its adsorption to the labware (EDTA test, *see* § 5: Materials and Methods for further information). Since the ECP test showed ligand-induced fluorescence change, the raw fluorescence variation recorded during the capillary scan was exploited to cast the titration curve, in a fashion similar to a conventional fluorometric titration.

However also in this case, CHCHD4 binding induced a significant thermophoretic effect (Fig. 3.15B). Interpolation of data points (Fig. 3.15C) yielded a $K_d$ value of 85 ± 15 nM for AIF in the reduced form, corresponding to a 100-fold enhanced affinity of AIF for CHCHD4 upon its reduction and dimerization. Such a significant change in the affinity for CHCHD4 may suggest that this interaction is mainly driven by AIF regions which undergo conformational rearrangements upon CT complex formation as, for example, its C-terminal domain.

The aforementioned protocol was used to test the affinity of the four pathogenic AIF variants, both in their oxidized and reduced forms, to assess whether the relative mutations could impair the interaction with CHCHD4 and, possibly, also to help in identify the AIF binding site for its protein partner. The results reported in Table 5 revealed that all tested AIF variants have very similar affinity for CHCHD4 with the exception of the G337E mutant in its reduced state. Indeed, MST measurements revealed that the G337E replacement induced a 5-fold decrease in the affinity of AIF for CHCHD4.

This result indicate that AIF-CHCHD4 complex formation is relatively mildly affected by the mutation, suggesting that the G337 residue is not directly involved in the interaction but could be located in a region close to the binding site. Through the MST approach, we tested the CHCHD4 interaction with a previously characterized pathogenic mutant, G307E[39]. In brief, AIF G307E was found to engage a less tight CT complex with $NAD^+$, being unable to establish contacts with the adenylate moiety of its ligand that provides stabilization of CT complex. Thus, we incubated AIF with NADH for five hours to fully reach the reduced form of the enzyme. Although through GST pull-down experiments the G307E mutation was reported to largely impair AIF interaction with CHCHD4[9], we provided evidences that such replacement does not alter AIF ability to form protein complex with its partner protein both in the oxidized and reduced states, being the obtained $K_d$ values comparable to those of the wild type protein. We speculated that during GST pull-down experiments the AIF mutant was not incubated with NADH for a proper period of time to fully reach the reduced (dimeric) form of the protein and, thus, a lower capacity to CHCHD4 was reported. In conclusion, MST results revealed an impairment induced by the G337E replacement of the pivotal interaction between AIF and CHCHD4. Such an effect is not a drastic one, suggesting that the G337 residue is not directly involved in the interaction region but rather in its neighborhood. However, the combination of a lower affinity for CHCHD4, a decreased CT complex stability and a higher susceptibility towards $O_2$ could trigger or exasperate the clinical symptoms of AIF G337E-related mitochondriopathy.

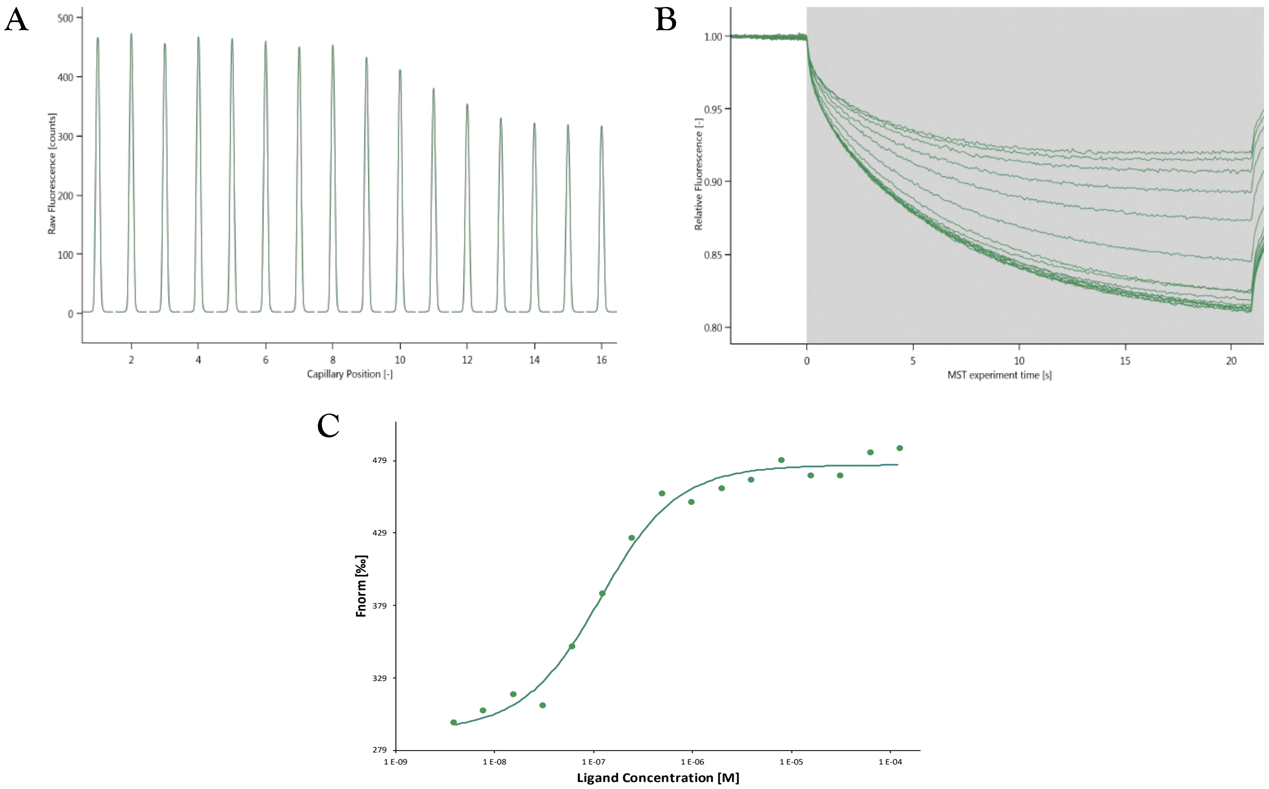

**Fig. 3.15 MicroScale Thermophoresis on wild type AIF in the reduced form in complex with CHCHD4.** (**A**) Capillary scan showed an initial fluorescence variation induced by ligand binding. (**B**) Initial fluorescence variation was used for $K_d$ calculation instead of MST, although the thermophoretic effect is clearly detectable. (**C**) Interpolation of initial fluorescence data from which a $K_d$ of 85 ± 15 nM was estimated.

| AIF | $K_d^{OX}$ (μM) | $K_d^{RED}$ (nM) |
|---|---|---|
| Wild type | 13 ± 2 | 85 ± 15 |
| G337E | 13 ± 4 | 425 ± 75 |
| G261S | 15 ± 2 | 70 ± 25 |
| D236G | 29 ± 5 | 85 ± 17 |
| F133L | 10 ± 4 | 78 ± 18 |
| G307E | 16 ± 1 | 60 ± 18 |

**Table 5. $K_d$ values of AIF variants in both their oxidized and reduced forms for HCHCD4.** The reduced G337E mutant showed a 5-fold decreased affinity for CHCHD4.

### 3.8.4 Molar ratio of AIF-CHCHD4 interaction

We tried to interpret SEC chromatographic profiles in order to define the stoichiometry of the AIF-CHCHD4 complex with the latter in its CT complex/dimeric state. We performed a small set of analytical SEC runs using a constant concentration of CHCHD4 and variable amounts of AIF, which was thus considered as a titrant. In Fig. 3.16A the chromatogram obtained with a AIF:CHCHD4 molar ratio of 1:2 is reported.

A peak at 11.5 ml, representing the reduced AIF in complex with CHCHD4, was detected, while the second peak at 15 ml represents the CHCHD4 excess, showing that 20 µM AIF were not sufficient to completely bind 40 µM CHCHD4. In both experiments, the peak at 19 ml represents the NADH excess. In contrast, the chromatogram obtained when AIF is twice as concentrated as CHCHD4 (Fig 3.16B), shows two partially overlapped peaks, one at 11.5 ml and the other at 12.5 ml, which represent reduced AIF in complex with CHCHD4 and reduced AIF alone, respectively. The two peaks have similar intensities, showing that half of total reduced AIF was in complex with CHCHD4 while the other half was not complexed. These results strongly suggest that the molar ratio is 1:1 between AIF:CHCHD4, an hypothesis supported by Hangen and collaborators[9].

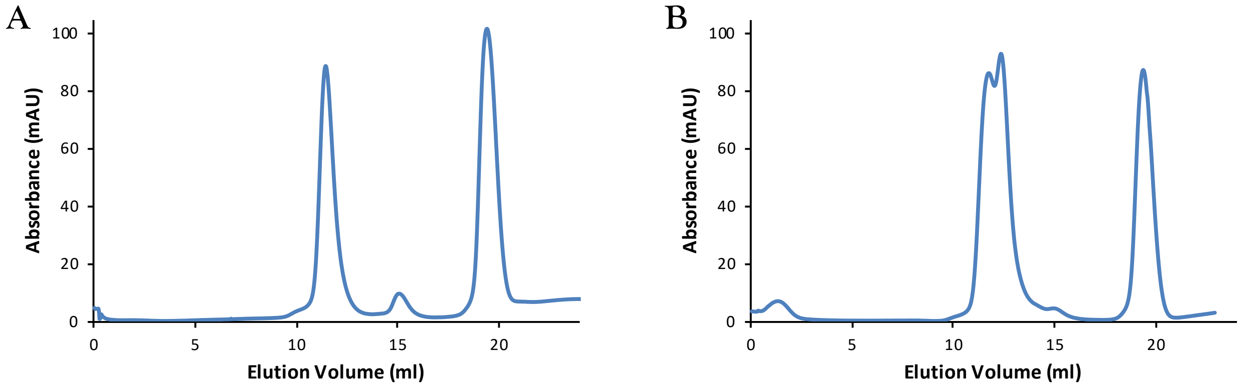

**Fig. 3.16 Analytical SEC experiments on the wild type AIF-CHCHD4 molar ratio.** (**A**) Chromatogram obtained incubating 40 µM CHCHD4 with 20 µM AIF preincubated with NADH . The single peak at 11.5 ml represents the AIF-CHCHD4 complex while that at 15 ml represents CHCHD4 excess. (**B**) Chromatogram obtained incubating 40 µM CHCHD4 with 80 µM of AIF preincubated with NADH-. In this case, two partially overlapped peaks were detected, one at 11.5 and the other at 12.5 ml, representing reduced AIF-CHCHD4 complex and reduced AIF alone. In both images, peak at 19 ml represents the NADH excess.

### 3.8.5 Crystallization trials on the wild type AIF-CHCHD4 complex

In order to validate MST results from a structural point of view and to identify a putative AIF interacting region, we performed both sitting drop and microbatch co-crystallization trials, by mixing NADH-preincubated AIF with CHCHD4 excess. In particular, solutions were prepared incubating a final concentration of 300 µM AIF with 5 mM NADH for 1 h for CT complex formation and then adding untagged CHCHD4 at a final concentration of 350 µM. Crystallization trials were performed as described in § 3.6. Unfortunately, no crystals were obtained, probably due to the intrinsic disordered nature of CHCHD4, which interferes with crystal formation.

To circumvent the problem, we decided to employ a synthetic peptide composed by the first N-terminal 27 residues of CHCHD4, which is reported to be able to interact with AIF.

### 3.8.6 Characterization and crystallization trials on the AIF-synthetic peptide complex

The N-terminal CHCHD4 synthetic peptide (synthetized by the Department of Biochemistry of Milan) was dissolved in 50 mM Tris-HCl, pH 8.0, 200 mM NaCl, 2 mM DTT at a final concentration of 2 mM. We tested its interaction with AIF in the reduced form through the MST approach (*see* § 3.8.3). MST results showed a $K_d$ value of 76 ± 2 nM, that represents an affinity very similar to that obtained for full-length CHCHD4, confirming that the N-terminal portion of the protein is necessary and sufficient for the interaction with AIF as previously reported[9].

Interestingly, the initial fluorescence change induced by ligand binding during the capillary scan (Fig. 3.17A) observed for the full-length protein was not detected in this case. This may suggest that full-length CHCHD4 is able to locally modify the environment of the fluorescent dye, which is located at AIF C-terminal region, a feature that the peptide does not possess.

Subsequently, we performed new crystallization trials as described in § 3.8.5, incubating 300 µM AIF with a 1.5-fold excess of peptide. We detected crystals formation (Fig. 3.18) in the sitting drop trials, and optimized the best conditions. Crystals grown in 12% PEG 6K, 0.1 mM Tris-HCl, pH 8.0 and 20% PEG 6K, 0.1 mM Tris-HCl, pH 8.0 were tested at the ESRF (European Synchrotron Radiation Facility in Grenoble, France), showing poor diffraction. New crystallization trials are on-going.

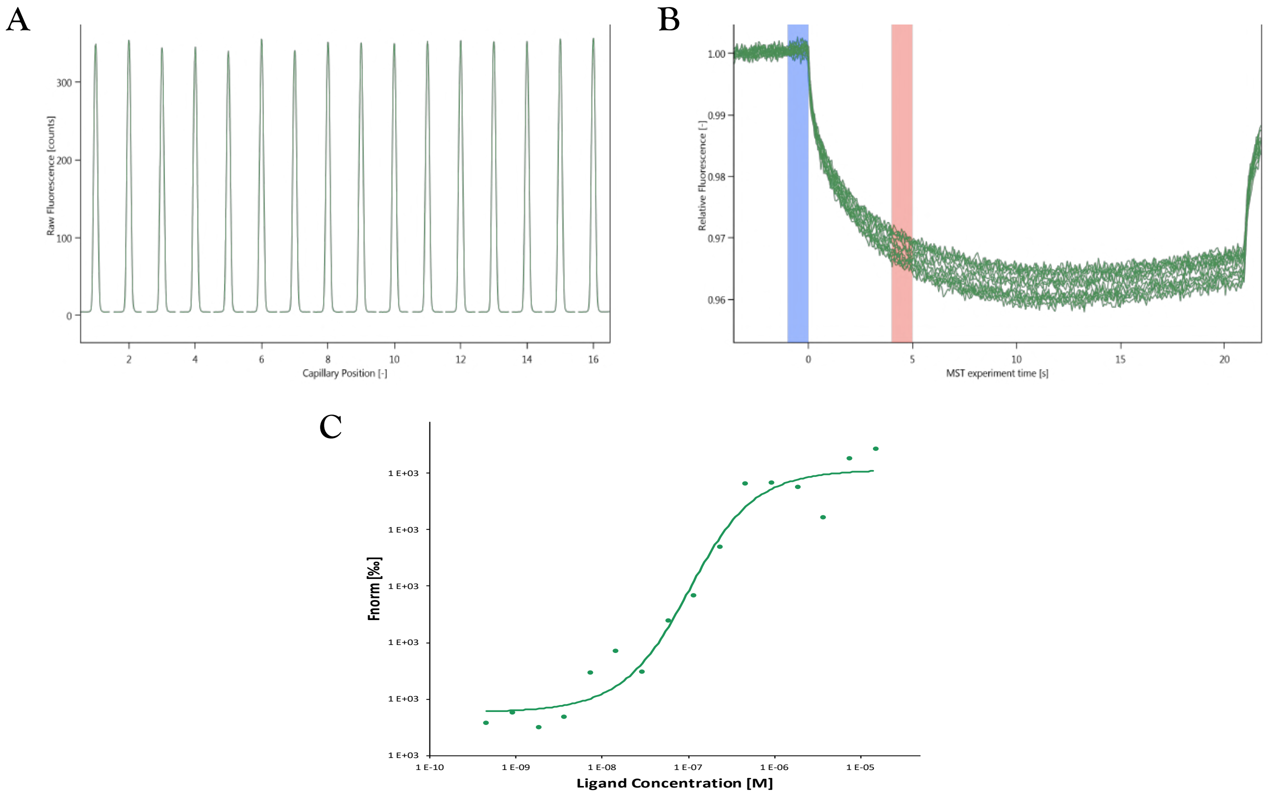

**Fig. 3.17 MicroScale Thermophoresis on wild type AIF in the reduced form in complex with CHCHD4 synthetic peptide.** (**A**) Differently from full-length CHCHD4, capillary scan showed constant initial fluorescence along all MST samples. (**B**) MST traces. From light blue interval was measured initial fluorescence intensity during capillary scan while the salmon red interval represents the region where the thermophoretic effect was exploited for $K_d$ calculation. (**C**) Interpolation of MST fluorescence data from which a $K_d$ of 76 ± 2 nM was estimated, a value very similar to that obtained using full-length CHCHD4.

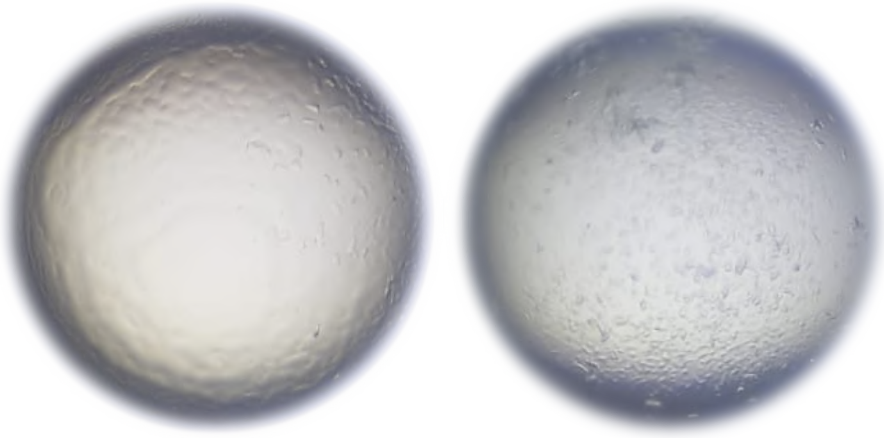

**Fig. 3.18** Crystals of AIF in the reduced form complex with the synthetic peptide obtained during crystallization trials.

## 3.9 Small-Angle X-ray Scattering measurements on AIF-CHCHD4 complex

As we encountered many difficulties in obtaining structural data on the AIF-CHCHD4 complex through a crystallographic approach, we decided to take advantage of the Small-Angle X-ray Scattering (SAXS) technique. Briefly, SAXS is based on measuring the scattered intensity of an X-ray beam hitting a sample at very small angles (between 0.1-10°). SAXS is widely used for low-resolution structural characterization of biological macromolecules in solution, i.e. in their native conformation, providing three-dimensional information in the 1-25 nm range.

More specifically, we used two different SAXS technique: the batch mode, where protein samples at different concentrations (from 0.1 to 40 mg/ml) are analyzed, and the SEC-SAXS, where a SEC experiment is coupled to SAXS measurements. An advantage of SEC-SAXS is the possibility to separate different proteins and quaternary states within a sample. On the other hand, the batch mode (where the SAXS signal is the average of all the components) allows to use protein samples at higher concentration where signal to noise ratio could be optimal at higher scattering angles. We, thus, performed SAXS measurements on AIF alone, both in the oxidized (monomeric) and reduced (dimeric) state, on CHCHD4 alone and on reduced AIF in complex with CHCHD4.

### 3.9.1 SAXS characterization of AIF in its monomeric and oxidized form

As first experiments, a solution of 307 µM AIF (18 mg/ml) in its oxidized-monomeric form was analyzed through SEC-SAXS. SAXS signal from the chromatogram analyzed with CHROMIXS[45] (Fig. 3.19A) showed a single symmetric peak, sign of protein sample purity and homogeneity, and its SAXS profile is reported in Fig. 3.19B. Structural parameters as the Radius of gyration ($R_g$), which represents an estimation of the molecule size, the $D_{max}$ value (molecule maximum dimension used to calculate the pair-distance distribution function) and the Bayesian molecular weight (that averages different methods to estimate Mw) calculated with PRIMUS[46] (Table 6) were consistent with the monomeric form of AIF. Agreement between SAXS and crystallographic data was investigated through CRYSOL[47] software which allows to calculate the solution scattering from atomic coordinates and to fit SAXS experimental curves. CRYSOL results (Fig. 3.20A) showed a significant discrepancy between SAXS and crystallographic data (shown in red and green, respectively), as the $\chi^2$ value was close to 29 (optimal $\chi^2$ value should be close to 1).

This discrepancy is probably due to the lack of almost 50 amino acids in the high resolution structure. Flexibility/unfolding degree was then evaluated through the Kratky plot, which is a plot of $s^2$ I(s) *vs* s. Unfolded (highly flexible) proteins should have a plateau in the Kratky plot at high q, while compact, globular proteins will have a bell-shaped (Gaussian) peak. A partially unfolded (flexible) protein may have a combination of the bell-shape and plateau, or a plateau that slowly decays to zero. For the case of oxidized AIF, Kratky plot resulted to be typical of globular and partially flexible proteins (Fig. 3.20B).

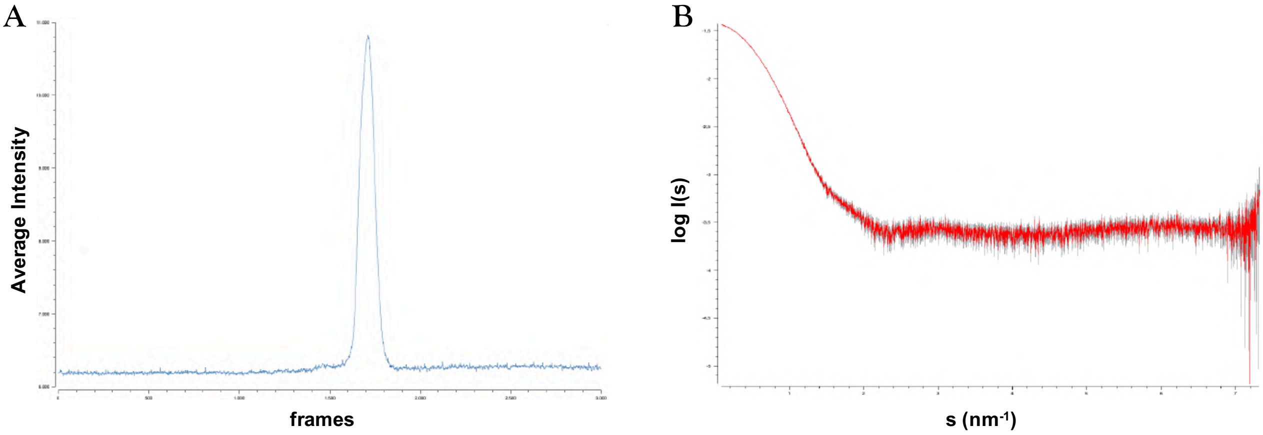

**Fig. 3.19 SEC-SAXS on oxidized AIF.** (**A**) SAXS signal from the chromatogram analyzed with CHROMIXS. (**B**) SAXS profile of oxidized AIF from SEC-SAXS experiment.

| $R_g$ (nm) | Bayesian MW range (kDa) | Expected MW (kDa) | $D_{max}$ (nm) |
|---|---|---|---|
| 2.6 ± 0.1 | 41.5 – 51.5 | 57 | 10.3 |

**Table 6. Structural parameters of oxidized AIF calculated with PRIMUS.** Data obtained through batch mode were consistent with the monomeric form of AIF.

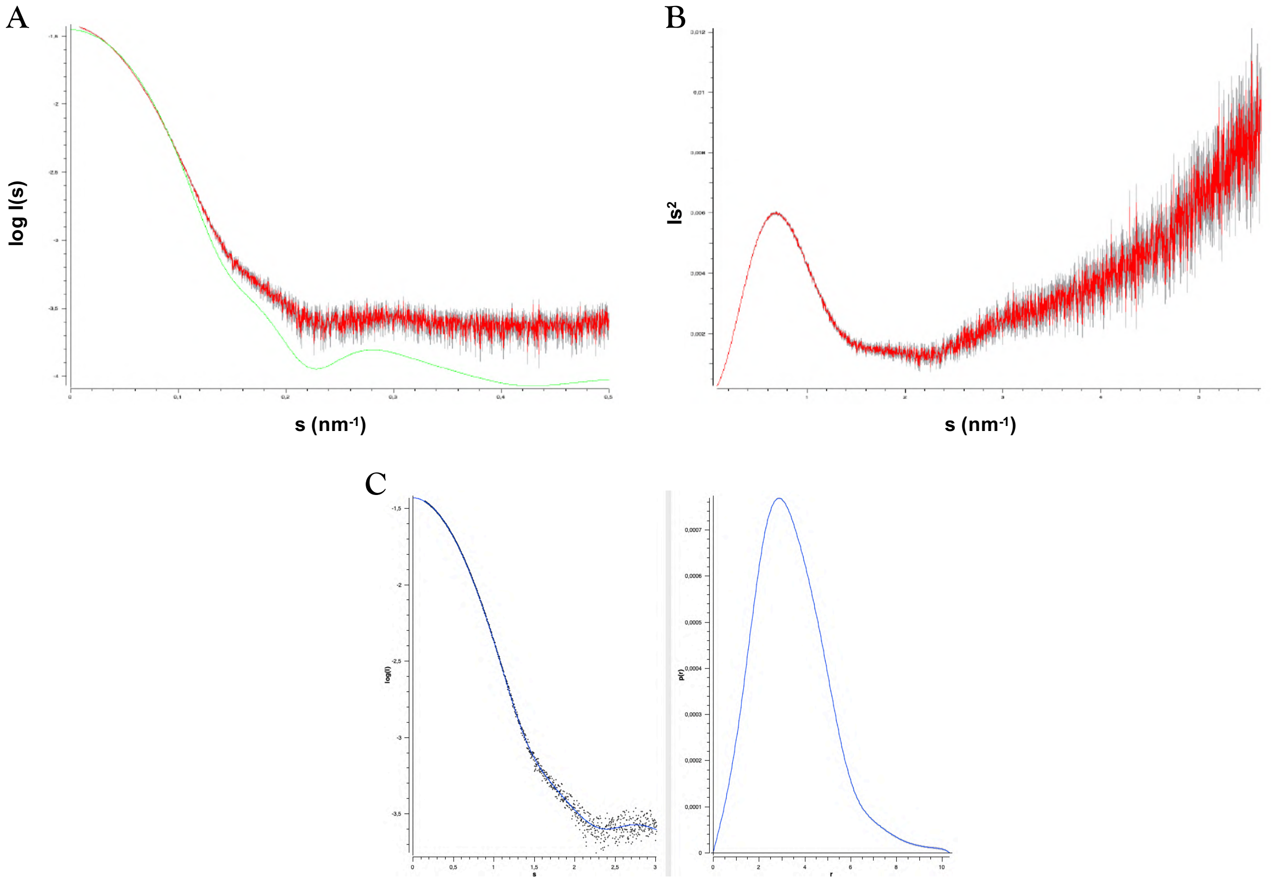

**Fig. 3.20 Crystallographic structure-SAXS data comparison and flexibility/unfolding degree analysis.** (**A**) Available crystallographic structure of oxidized AIF (PDB 3GD3) was compared with SAXS data (in green and red, respectively) through CRYSOL software. (**B**) Kratky plot was typical for globular and partially flexible proteins. (**C**) Pair distance distribution calculated from $D_{max}$ (right) and the corresponding fitting (left).

Subsequently, twenty SAXS models were constructed with the DAMMIF software, a widely used tool for rapid *ab initio* shape determination. The most representative model ($\chi^2$ value of 1.2) was superimposed on the high resolution structure of murine oxidized AIF (PDB 3GD3[41]) using SUPCOMB[48] tool and superimposition was evaluated through the Normalized Spatial Discrepancy (NSD) which, for ideally superimposed similar objects tends to 1. Final model reported in Fig. 3.21 showed that the crystallographic structure fits almost completely within SAXS model, with a NSD value of 2.3. The extra volume of the *ab initio* model probably represents flexible and/or missing regions from high resolution data.

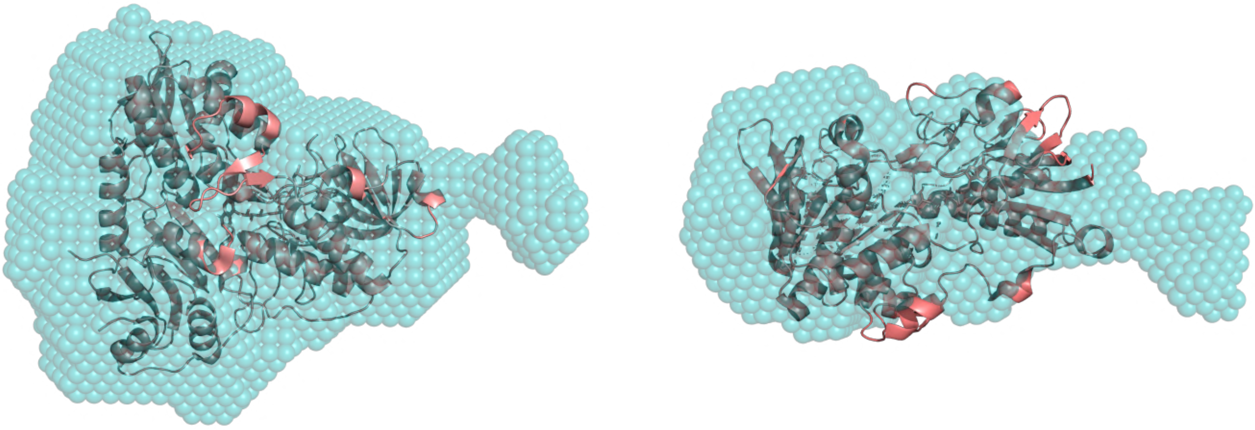

**Fig. 3.21 SAXS model of oxidized AIF.** Model generated with DAMMIF was superimposed on the crystallographic structure of oxidized AIF (PDB 3GD3) with a final NSD value of 2.3. The two panels show the same SAXS model rotated by 90° with respect to its horizontal axis.

### 3.9.2 SAXS characterization of AIF in its reduced and dimeric form

Analysis of AIF in its reduced and dimeric form was performed in the batch mode. Five serial dilutions of AIF (from 16 to 0.5 mg/ml) pre-incubated with 2 mM NADH were prepared. In Fig. 3.22A are reported the SAXS profiles at different AIF concentrations from which we selected that at 2 mg/ml (Fig. 3.22B) for further analysis and model construction. Bayesian molecular weight was found to be consistent with the dimeric assembly and other parameters calculated with PRIMUS are reported in Table 7.

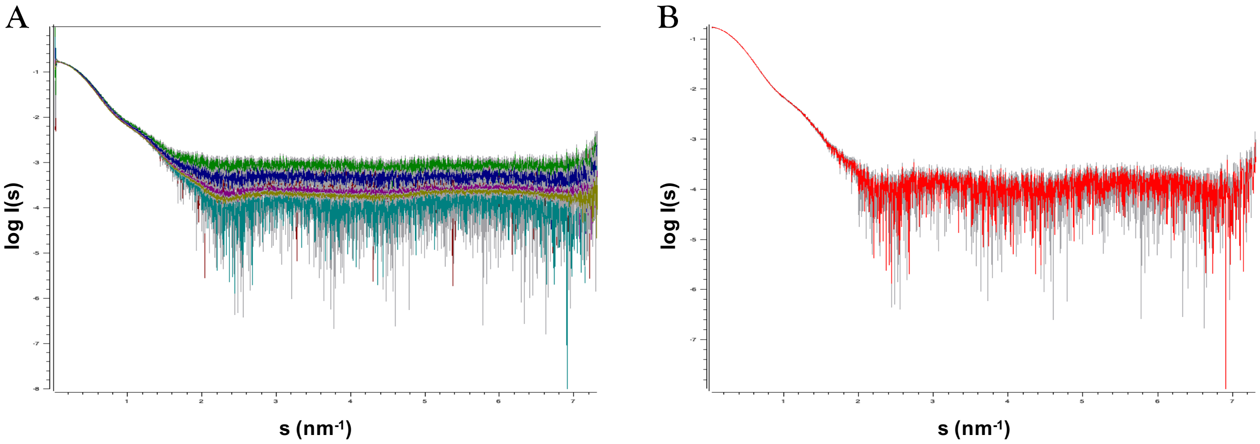

**Fig. 3.22 SAXS profiles of reduced AIF obtained in batch mode.** (**A**) SAXS profiles of sample dilutions starting from an initial concentration of 16 mg/ml to a final one of 0.5 mg/ml. (**B**) SAXS profile of the sample dilution used for further analysis and model construction (2 mg/ml).

| $R_g$ (nm) | Bayesian MW range (kDa) | Expected MW (kDa) | $D_{max}$ (nm) |
|---|---|---|---|
| 3.8 ± 0.1 | 116 – 142 | 114 | 13.1 |

**Table 7. Structural parameters of reduced AIF calculated with PRIMUS.** Data obtained through batch mode were consistent with the dimeric form of AIF.

Experimental and calculated data (from PDB 3GD4[41]) (shown in green and blue, respectively) were compared with CRYSOL software, whose results (Fig. 3.23A) showed again a significant discrepancy with a $\chi^2$ value of 75. Flexibility/unfolding degree were assessed through the Kratky plot, which resulted to be typical of multidomain proteins (Fig. 3.23B).

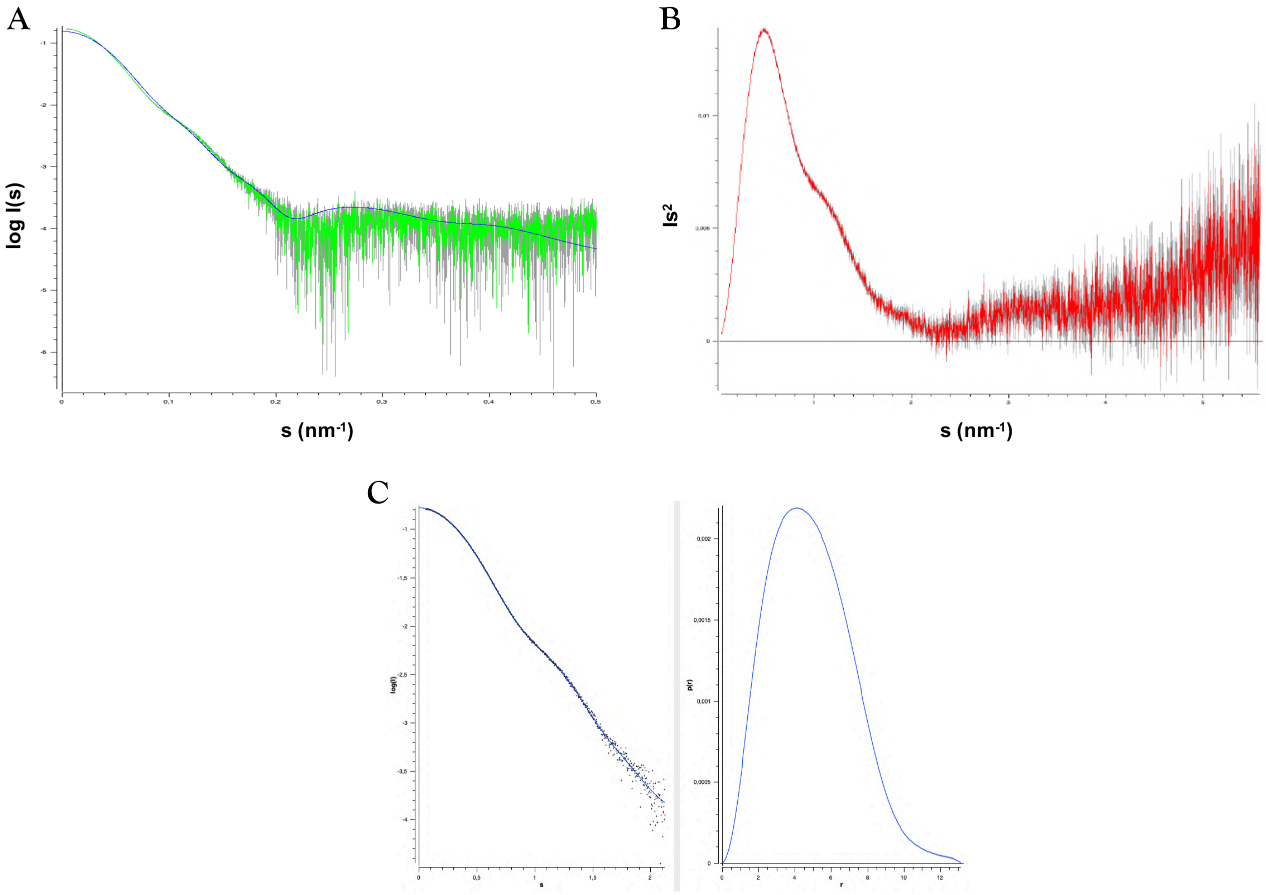

**Fig. 3.23 Crystallographic structure-SAXS data comparison and flexibility/unfolding degree analysis.** (**A**) Available crystallographic structure of reduced AIF (PDB 3GD4) was compared with SAXS data (in blue and green, respectively) through CRYSOL software, showing a significant discrepancy due likely to incompleteness of PDB coordinates. (**B**) Kratky plot was typical for globular multidomain proteins. (**C**) Pair distance distribution calculated from $D_{max}$ (right) and the corresponding fitting (left).

Similarly to the oxidized form of AIF, DAMMIF was used for construction of *ab initio* models, assuming a P1 or a P2 symmetry. The quality of the most representative models constructed in P1 and P2 symmetry was comparable but, since we expected the P2 symmetry for the dimeric form of AIF, we considered P2 symmetry models for further analysis. The most representative P2 symmetry model was superimposed on the available high resolution structure of murine reduced AIF (PDB 3GD4[41]) using SUPCOMB.

Interestingly, high resolution data fitting within SAXS models was not optimal, with NSD value of 3.3 and showing significantly large AIF regions protruding outside the model (Fig. 3.24A). This was a relevant feature suggesting that in the crystal reduced AIF adopts a different conformation, probably induced by crystallographic restrains. To verify the results obtained with the batch mode, a solution of 16 mg/ml AIF, pre-incubated with 2 mM NADH, was analyzed through SEC-SAXS measurements. The *ab initio* models built using SEC-SAXS data showed the same overall features as those obtained with the batch mode, confirming that, in solution, reduced AIF adopts a different conformation compared to the crystallographic one (Fig. 3.24B).

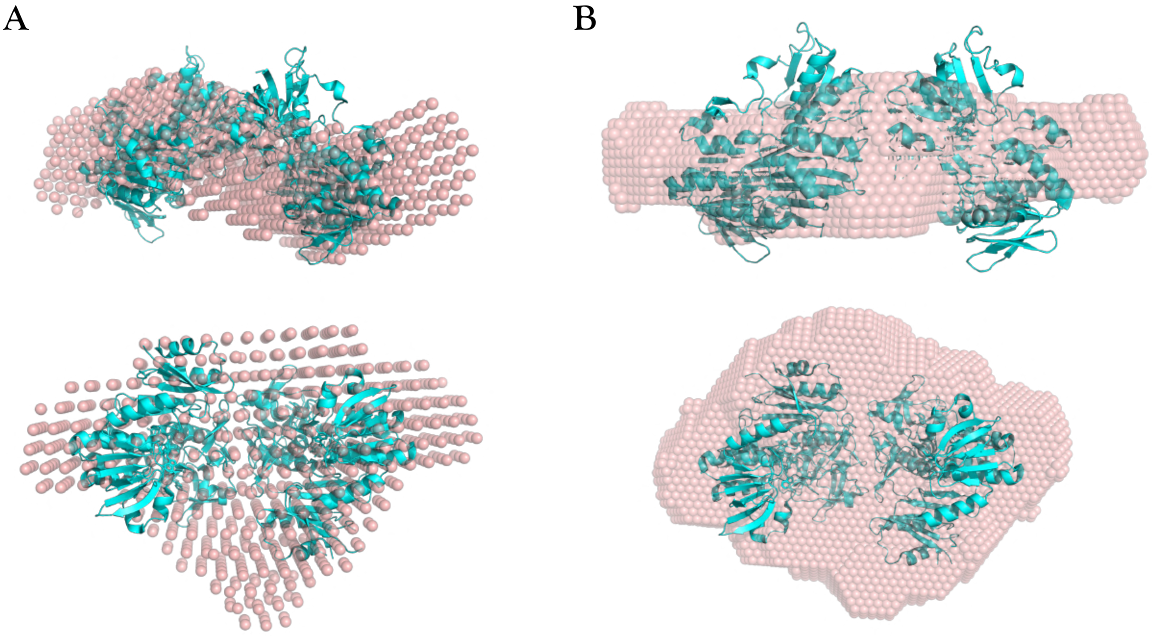

**Fig.3.24 SAXS models of reduced AIF.** Models constructed from batch mode (**A**) and SEC-SAXS experiments (**B**) were superimposed to the available crystallographic structure of reduced AIF (PDB 3GD4). In both cases, significant portions of the crystallographic structure were not described by the SAXS model, suggesting that in solution AIF could adopt a different conformation with respect to the crystallographic one. Upper and lower panels show top and front view of the SAXS model, respectively.

### 3.9.3 SAXS characterization of CHCHD4

For the first time we performed a structural characterization of murine CHCHD4 through SAXS technique. The protein was initially analyzed in the batch mode, where five serial dilutions of CHCHD4 were prepared starting from an initial concentration of 4.25 mg/ml to a final one of 0.14 mg/ml. From all tested concentrations (Fig. 3.25A) we chose that at 2.28 mg/ml for further analysis and model construction (Fig. 3.25B). Interestingly, Bayesian molecular weight calculated with PRIMUS was found to be more consistent with the dimeric form of the protein or with a monomer-dimer equilibrium (Table 8), a feature that we already reported during CHCHD4 analytical SEC and DLS experiments (*see* § 3.7). Kratky plot was typical of elongated/flexible proteins (Fig. 3.26A).

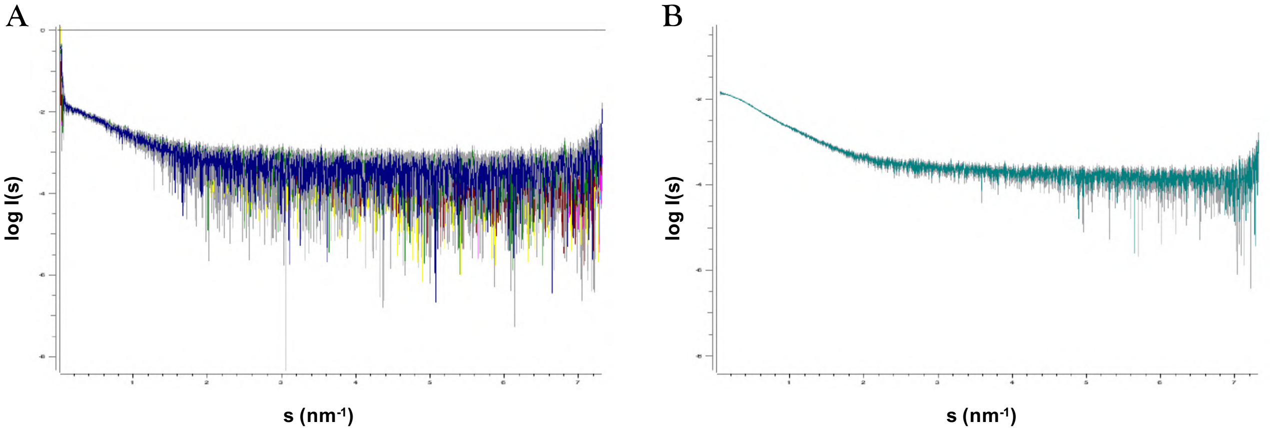

**Fig. 3.25 SAXS profiles of CHCHD4 obtained in batch mode.** (**A**) SAXS profiles of sample dilutions starting from an initial concentration of 4.25 mg/ml to a final one of 0.14 mg/ml. (**B**) SAXS profile of the sample dilution used for further analysis and model construction (2.28 mg/ml).

| $R_g$ (nm) | Bayesian MW range (kDa) | Expected MW (kDa) | $D_{max}$ (nm) |
|---|---|---|---|
| 3.1 ± 0.8 | 22 – 29 | 16 | 10.8 |

**Table 8. Structural parameters of CHCHD4 calculated with PRIMUS.** Data obtained through batch mode were more consistent with CHCHD4 in dimeric form than in a monomeric one.

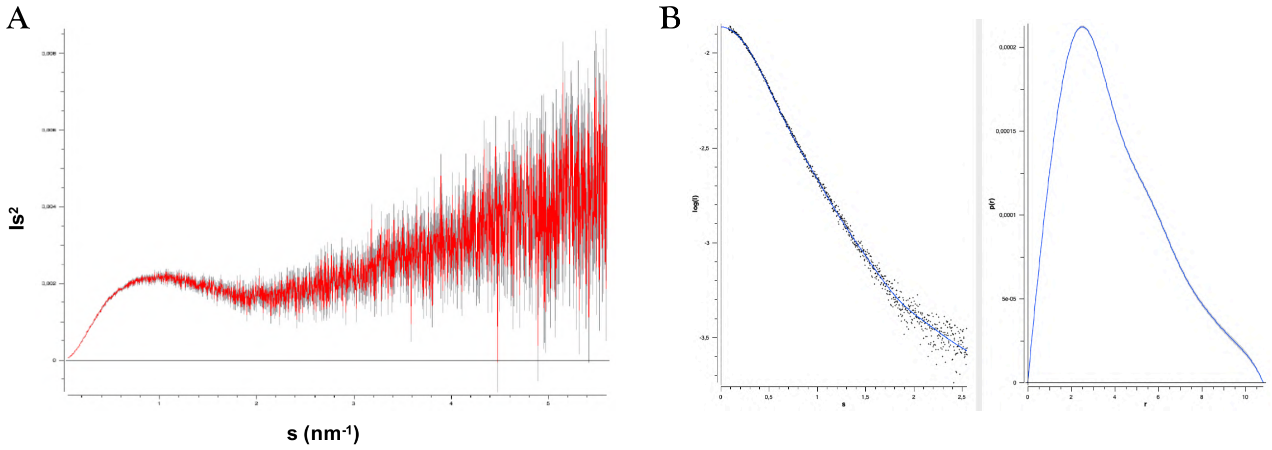

**Fig. 3.26 Flexibility/unfolding degree analysis.** (**A**) Kratky plot was typical of not compacted and possibly elongated/flexible proteins. (**B**) Pair distance distribution calculated from $D_{max}$ (right) and the corresponding fitting (left).

Multiple SAXS models were constructed using DAMMIF with P1 symmetry and superimposed with SUPCOMB with a mean NSD value of 1.1 ± 0.1 (Fig. 3.27A). The available NMR structure of human CHCHD4 (PDB 2K3J), which lacks the N-terminal and C-terminal regions, was superimposed to the most representative SAXS model ($\chi^2$ of 1.3) using SUPCOMB (Fig. 3.27B). As expected, the NMR structure did not fit within the SAXS model (NSD value of 42.9) which appeared too much extended to accommodate only one CHCHD4 molecule. To deeper investigate this result, we took advantage of CORAL[49] software, which allows rigid body modelling of proteins whose components have missing portions.

Missing residues were modeled starting from the incomplete NMR structure of human CHCHD4 and two different kind of models were constructed, one assuming that CHCHD4 was in a monomeric conformation and the other in a dimeric one. $\chi^2$ values of the resulting models clearly showed that during batch experiments CHCHD4 was present in solution as a dimer ($\chi^2$ of 1.2 against a $\chi^2$ of 5.2 obtained for monomeric CHCHD4 model). In addition, according to the model describing CHCHD4 in a dimeric conformation, the dimerization process should occur through the core region (Fig. 3.28), a very new feature of CHCHD4, here reported for the first time.

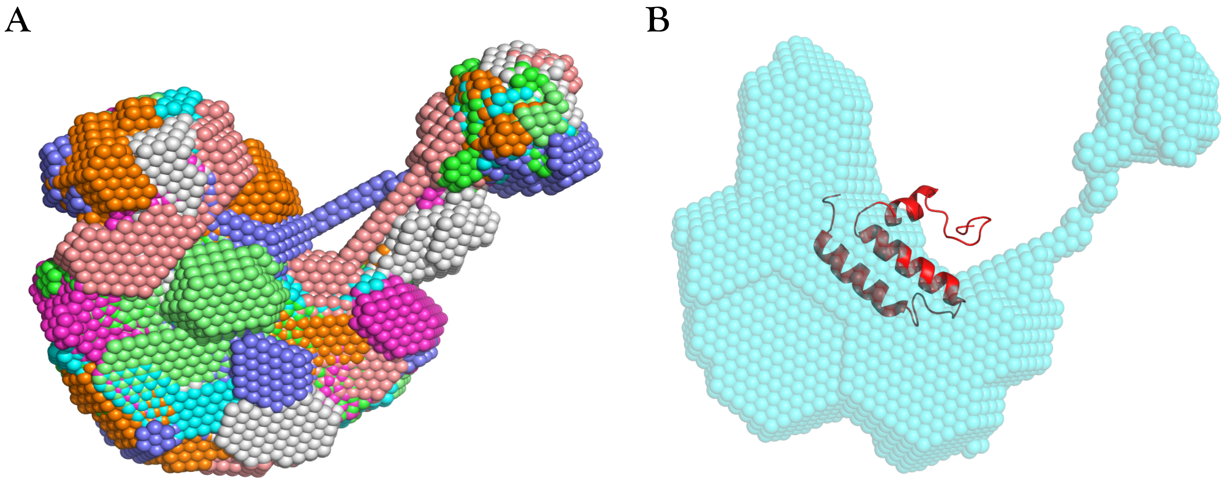

**Fig. 3.27 SAXS models of CHCHD4 form batch mode experiments.** (**A**) Superimposition of some CHCHD4 models with a main NSD value of 1.1 ± 0.1. (**B**) Superimposition of CHCHD4 most representative model with the incomplete NMR structure of CHCHD4 (PDB 2K3J). The model is too much extended to accommodate only one CHCHD4 molecule.

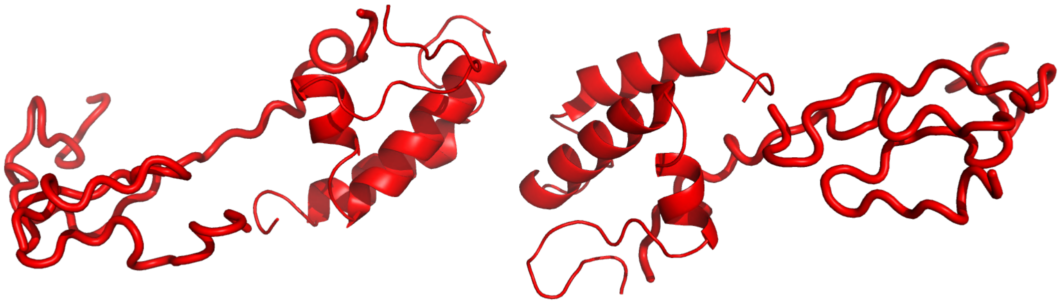

**Fig. 3.28 SAXS model of dimeric CHCHD4.** Missing amino acids from CHCHD4 NMR structure were modelled with CORAL and new models were constructed assuming CHCHD4 as a dimer, showing a much better $\chi^2$ value than previous constructed models shown in Fig. 3.27 (1.2 against 5.2, respectively).

To better investigate the oligomerization state of CHCHD4, a SEC-SAXS was performed (7.5 mg/ml) to separate the possible contribution of monomers and dimers to the protein model. The SAXS signal from the chromatogram analyzed with CHROMIXS (Fig. 3.29A) showed two unequal peaks, differently from what expected, the less intense peak corresponded to the dimer and the other to the monomer, according to the elution volumes (*see* § 3.1.2, Fig. 3.3A).

The peak corresponding to the monomeric CHCHD4 was selected for further analysis and its SAXS profile is reported in Fig. 3.29B. Calculated $R_g$ and the Bayesian molecular weight resulted more consistent with the monomeric form of the protein (Table 9), suggesting that dimerization of CHCHD4 could be concentration-dependent. Kratky plot was similar to that obtained in batch mode.

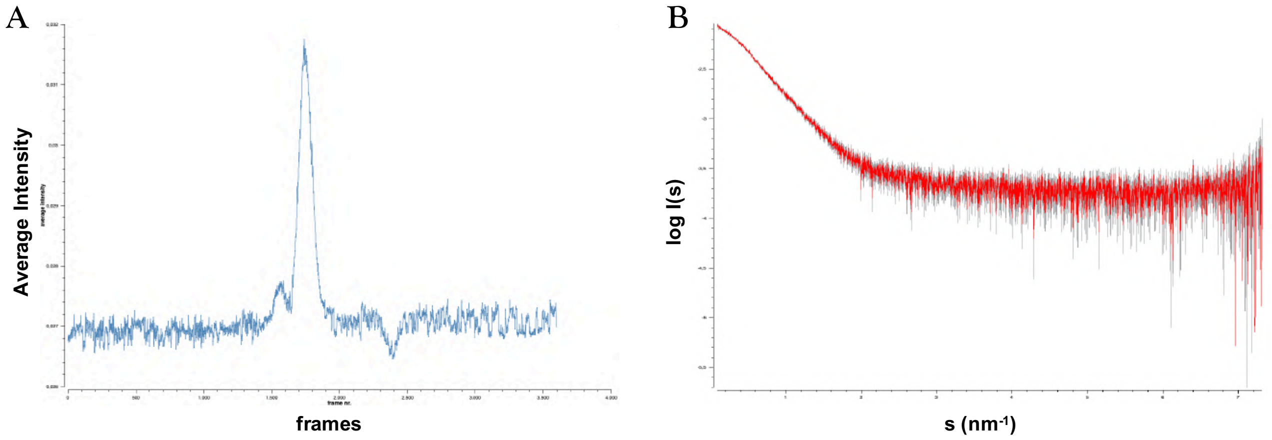

**Fig. 3.29 SEC-SAXS on CHCHD4.** (**A**) SAXS signal from the chromatogram analyzed with CHROMIXS. (**B**) SAXS profile of CHCHD4 from SEC-SAXS experiment.

| $R_g$ (nm) | Bayesian MW range (kDa) | Expected MW (kDa) | $D_{max}$ (nm) |
|---|---|---|---|
| 2.6 ± 0.4 | 13 – 18 | 16 | 7.9 |

**Table 9. Structural parameters of CHCHD4 calculated with PRIMUS.** Data obtained through SEC-SAXS were consistent with CHCHD4 in a monomeric form.

Indeed, new SAXS models of monomeric CHCHD4 were constructed (Fig. 3.30A) and their superimposition gave a mean NSD value of 0.76 ± 0.02. The most representative model ($\chi^2$ of 1.2) reported in Fig. 3.30B was superimposed with the incomplete NMR structure of CHCHD4 (PDB 2K3J). The model describes a central compact region representing the CHCHD4 portion containing disulfide bonds network, while the two external and elongated regions could be associated to the protein N- and C-terminal extensions.

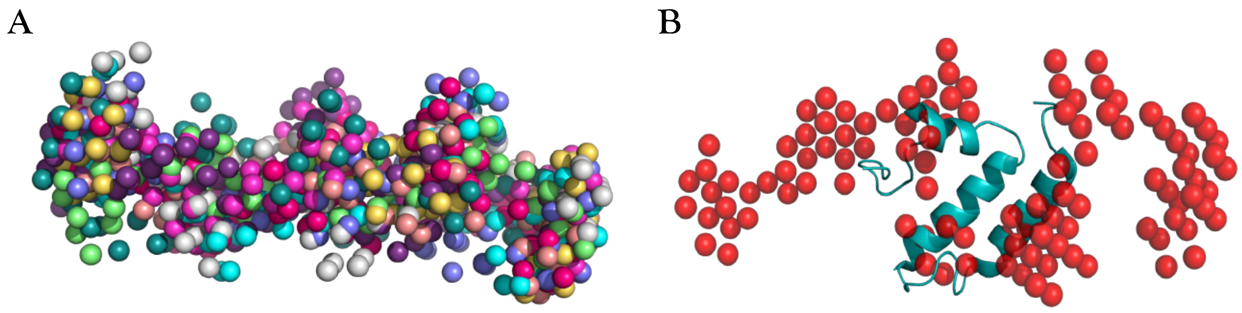

**Fig. 3.30 SAXS models of CHCHD4 form SEC-SAXS experiments.** (**A**) Superimposition of some CHCHD4 models with a main NSD value of 0.76 ± 0.02. (**B**) Superimposition of CHCHD4 most representative model (shown in red) with the incomplete NMR structure of CHCHD4 (PDB 2K3J, shown in cyan). The model appeared to be compatible with CHCHD4 in a monomeric form.

### 3.9.4 SAXS characterization of reduced AIF in complex with CHCHD4

After individual characterization of both AIF and CHCHD4, the last step was the characterization of their complex which was performed in both batch mode and SEC-SAXS. For the batch mode, five serial dilutions of AIF (9.80 to 0.31 mg/ml) pre incubated with 4 mM NADH in complex with CHCHD4 (3.1 to 0.6 mg/ml) were prepared. From all tested concentrations (Fig. 3.31A) we chose that at 2.46 mg/ml AIF for further analysis and models construction (Fig. 3.31B). Estimated structural parameters as $R_g$ and Bayesian molecular weight were consistent with the heterotetrameric complex under investigation (Table 10) and the Kratky plot was typical for multidomain protein with a flexible linker (Fig. 3.32A).

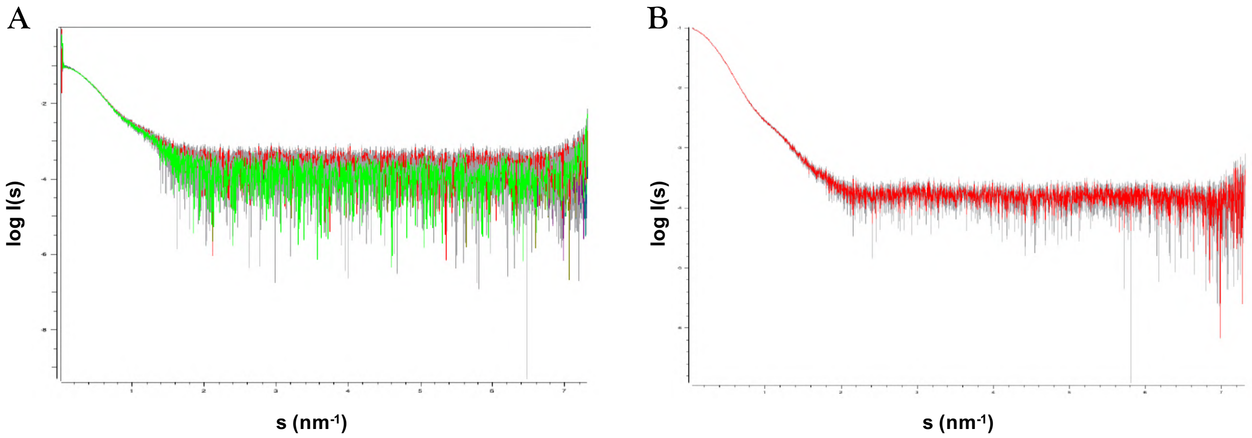

**Fig. 3.31 SAXS profiles of reduced AIF in complex with CHCHD4 obtained in batch mode.** (**A**) SAXS profiles of sample dilutions starting from an initial concentration of 9.8 mg/ml to a final one of 0.31 mg/ml. (**B**) SAXS profile of the sample dilution used for further analysis and model construction (2.46 mg/ml).

| $R_g$ (nm) | Bayesian MW range (kDa) | Expected MW (kDa) | $D_{max}$ (nm) |
|---|---|---|---|
| 4.4 ± 0.3 | 127 – 162 | 146 | 20.6 |

**Table 10. Structural parameters of reduced AIF in complex with CHCHD4 calculated with PRIMUS.** Data obtained through batch mode were consistent with the protein complex.

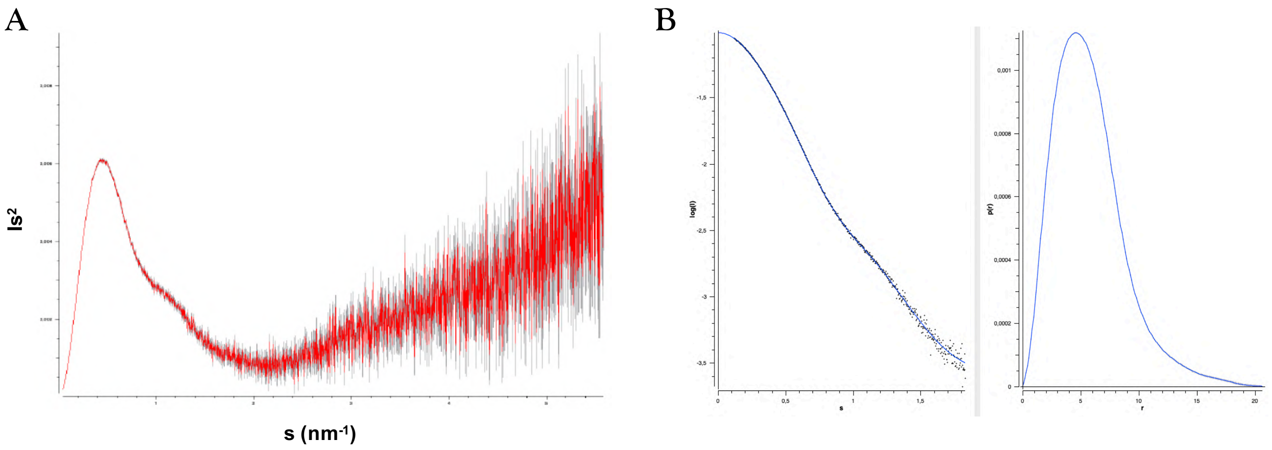

**Fig. 3.32 Flexibility/unfolding degree analysis.** (**A**) Kratky plot was typical of multidomain proteins with a flexible linker. (**B**) Pair distance distribution calculated from $D_{max}$ (right) and the corresponding fitting (left).

Models construction was performed assuming P1 or P2 symmetry. Similarly to what observed for AIF in the reduced state, the quality of the most representative models constructed in P1 and P2 symmetry were comparable but, since we expected the P2 symmetry for the protein-protein complex, we considered P2 symmetry models for further analysis. The most representative model was then superimposed to that of reduced AIF obtained in batch mode with a final NSD value of 0.9 (Fig 3.33A, in hot pink and cyan, respectively), revealing two symmetric regions exclusively present in the AIF-CHCHD4 complex model and, thus, representing a putative interaction region between the two proteins (red arrows in Fig. 3.33 A). SAXS models were then superimposed with high resolution data of reduced AIF (Fig. 3.33B) where the G337 residue, indicated by the red arrow, is located in the neighborhood of the putative AIF interacting region. Moreover, since the residue is solvent-exposed, it could contact the N-terminal 27 amino acids of CHCHD4 and/or cause local conformational rearrangements leading to a decreased affinity for CHCHD4 as a consequence of G337E replacement.

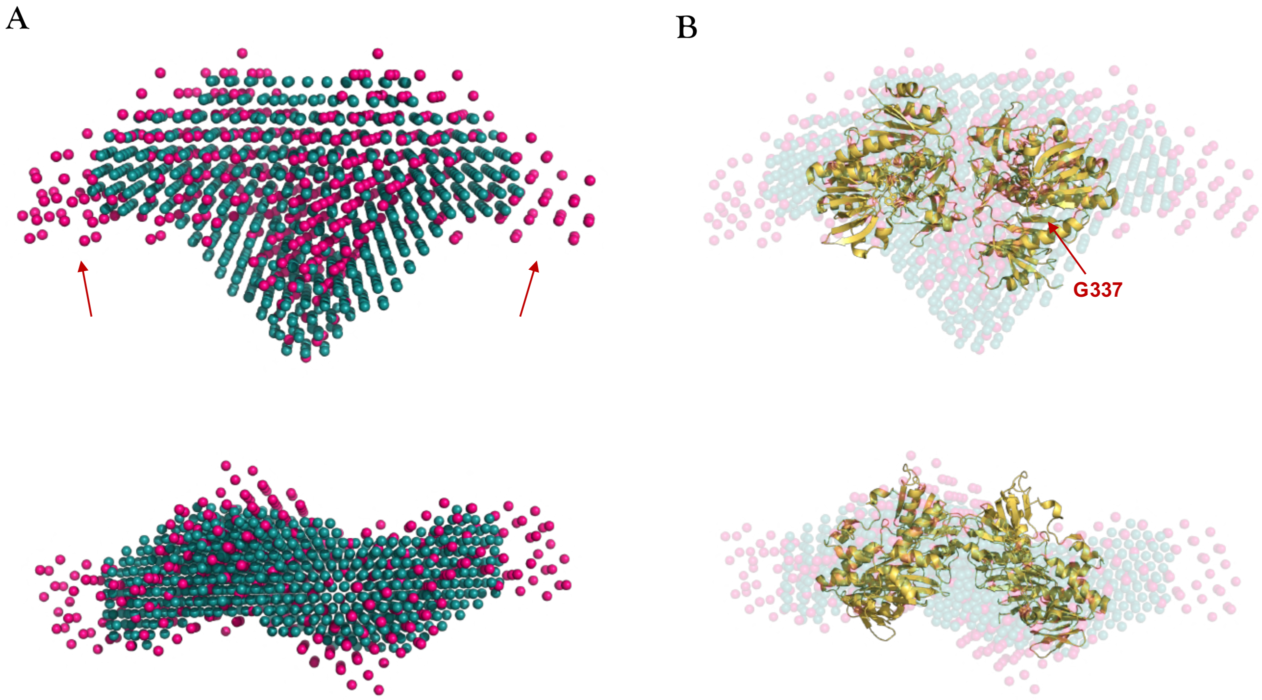

**Fig. 3.33 SAXS models superimposition of reduced AIF (cyan) and reduced AIF in complex with CHCHD4 (hot pink).** (**A**) Red arrows indicate the two specular regions exclusively present in the AIF-CHCHD4 complex model (hot pink) where CHCHD4 could be accommodated. Upper and lower panels show front and top view of the SAXS model, respectively. (**B**) Superimposition of reduced AIF-CHCHD4 complex models to reduced AIF crystallographic structure. The G337 residue is located in the neighborhood of the putative interacting region between the two proteins. Upper and lower panels show front and top view of the SAXS model, respectively.

Subsequently, to validate the data obtained in batch mode, new SEC-SAXS measurements on the reduced AIF in complex with CHCHD4 were performed (AIF at 9.8 mg/ml incubated with CHCHD4 3.1 mg/ml). SAXS signal from the chromatogram analyzed with CHROMIXS (Fig. 3.34A) showed one major peak preceded by a small shoulder. The most intense peak was considered for further analysis and the corresponding SAXS profile is reported in Fig. 3.34B.

Structural parameters reported in Table 11 were very similar to those observed for the batch mode and consistent with expected size and molecular weight of the reduced AIF-CHCHD4 complex.

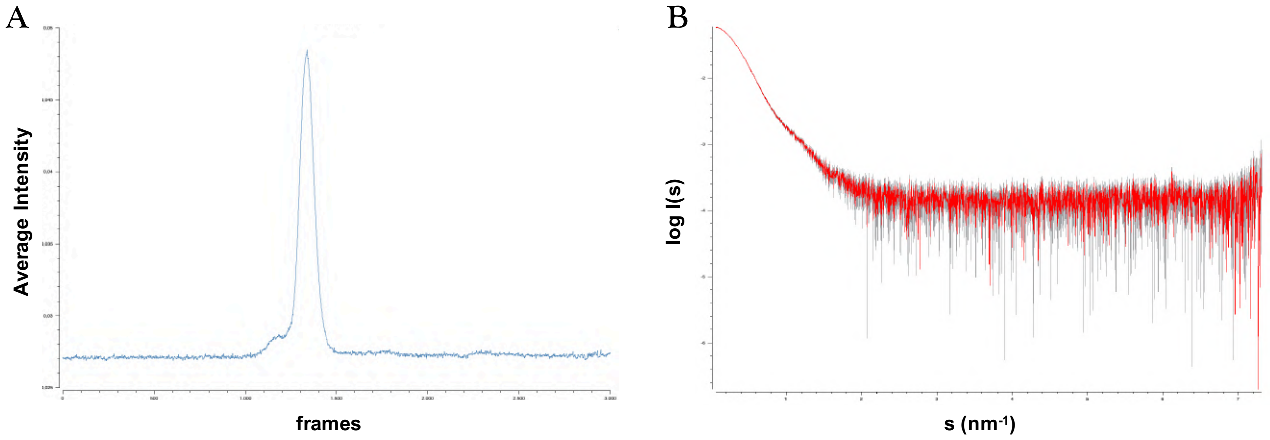

**Fig. 3.34 SEC-SAXS on reduced AIF in complex with CHCHD4.** (**A**) SAXS signal from the chromatogram analyzed with CHROMIXS. (**B**) SAXS profile of reduced AIF in complex with CHCHD4 from SEC-SAXS experiment.

| $R_g$ (nm) | Bayesian MW range (kDa) | Expected MW (kDa) | $D_{max}$ (nm) |
|---|---|---|---|
| 4.2 ± 0.2 | 127 – 162 | 146 | 17.1 |

**Table 11. Structural parameters of reduced AIF in complex with CHCHD4 calculated with PRIMUS.** Similarly batch mode results, data obtained through SEC-SAXS were consistent with the protein heterotetrameric complex.

Construction of new models performed imposing a P1 or a P2 symmetry gave similar $\chi^2$ values and only models in P2 symmetry were considered for further analysis. The most representative model was superimposed to that of reduced AIF obtained with SEC-SAXS with a final NSD value of 1.06. Very similarly to what observed in the previous model, superimposition results revealed the same two specular regions that could accommodate two CHCHD4 molecules (red arrows in Fig. 3.35A). Unfortunately, comparison of SAXS models with high resolution data (Fig. 3.35B) revealed that the crystallographic structure of reduced AIF was superimposed on the SAXS model in a different orientation with respect to the models obtained in batch mode, suggesting again that the crystal structure of reduced AIF does not completely reflect that of the protein in solution. The difference between high resolution data and SAXS models made it impossible to precisely identify the interacting region between the two proteins but, anyway, in all the models from both batch and SEC-SAXS experiments, the G337 residue was found to be located close to the putative interaction region between the two proteins. This feature is in accordance with previously described MST data showing a 5-fold decreased affinity for CHCHD4 induced by G337E replacement (*see* § 3.8.3).

In addition, SAXS models of the AIF-CHCHD4 complex constructed both in P1 and P2 symmetry revealed two different and specular regions where CHCHD4 could interact with AIF. This suggests a molar ratio of 1:1 between oxidized and monomeric AIF with one molecule of CHCHD4, in accordance with our predictions based on previously described analytical SEC experiments (*see* § 3.8.4).

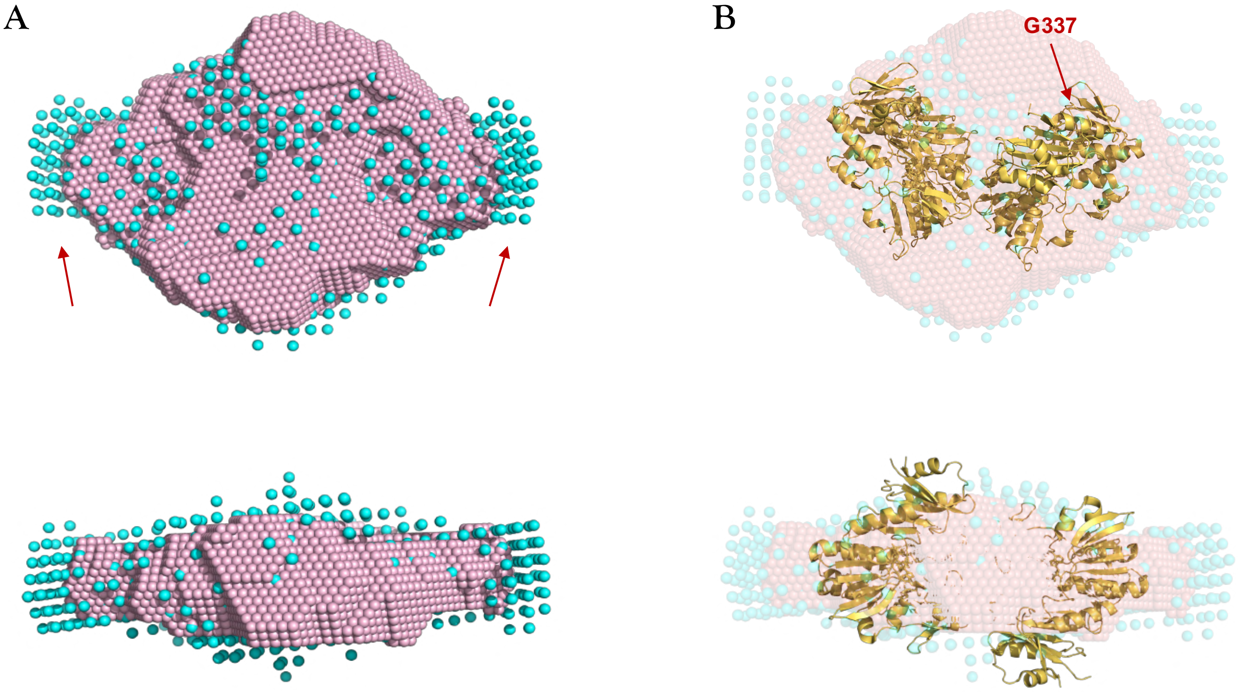

**Fig. 3.35 SEC-SAXS models superimposition of reduced AIF (salmon) and reduced AIF in complex with CHCHD4 (light blue).** (**A**) Red arrows indicate the two specular regions exclusively present in the AIF-CHCHD4 complex model (light blue) where CHCHD4 could be accommodated. Upper and lower panels show front and top view of the SAXS model, respectively. (**B**) Superimposition of reduced AIF-CHCHD4 complex models to reduced AIF crystallographic structure which, although, was oriented differently with respect to batch mode results. This suggest again that high resolution data of reduced AIF do not reflect completely its conformation in solution. Anyway, the G337 residue is located again in the neighborhood of the putative interacting region between the two proteins. Upper and lower panels show front and top view of the SAXS model, respectively.

# 4. Conclusions and future perspectives

The apoptosis inducing factor (AIF) is an important mitochondrial FAD-dependent flavoprotein, known to play opposite roles in eukaryotic cells: while when released into the cytoplasm it triggers caspase-independent apoptosis, within mitochondria it is needed to maintain the correct morphology of the organelle and OXPHOS functioning through interaction with CHCHD4. Unfortunately, AIF intramitochondrial role is still largely unknown in its molecular details, even though the formation of a surprisingly air-stable dimeric CT complex with NAD(H) and the direct interaction with CHCHD4, a key regulator of the import and assembly of respiratory complexes subunits, seem to be pivotal processes in its function. Over the last years, nine individual point mutations of the AIFM1 gene were found to be associated with severe human mitochondriopathies, with neurodegeneration as common feature. To better understand how AIF is implicated in cellular maintenance and pathology onset, we selected a set of four pathogenic mutants of the murine protein (G337E, D236G, G261S and F133L, equivalent to G338E, D237G, G262S and F134L in human AIF) that still lack a complete biophysical/biochemical characterization. Therefore, the present PhD project was mainly focused on the effect of pathogenic replacements on AIF biochemical properties with a special focus on its interaction with CHCHD4.

The first step of the project was the production of the apoptogenic form of murine AIF carrying the equivalent amino acid replacements of the human protein. The four variants were overexpressed in *E. coli* and purified using the same protocol described for the wild type protein[10]. Subsequently, the four AIF variants were biochemically and biophysically characterized. In first place, thermal stability analysis revealed the same destabilizing effect upon NAD(H) binding and CT complex formation for all studied AIF mutants, as previously described for the wild type protein[39]. Interestingly, the G337E mutation was found to significantly destabilize the CT complex state by 6 °C with respect to the wild type protein. A larger destabilization effect was observed for the G261S mutation, which, even in the presence of NADH excess, showed an extremely unstable CT complex state. Conformational stability results were then confirmed through several spectrophotometric and kinetic studies. Indeed, CT complex stability towards $O_2$ clearly showed the inability of the G261S mutant to maintain an air-stable CT complex, which was lost in few seconds after NADH excess removal. A slighter but significant instability towards $O_2$ was observed also for the CT complex engaged by the G337E mutant, whose reoxidation was 8-fold faster with respect to the wild type protein.

However, kinetic studies revealed only mild effects on the AIF redox catalytic properties induced by the mutations under study. In detail, the G337E replacement was found to cause a 3-fold decrease and a 2-fold increase in the $k_{\mathrm{cat}}$ and $K_{\mathrm{M}}$ for NADH in the NADH-DCIP diaphorase reaction, respectively, while the newly discovered F133L mutations led to a 3-fold increased $K_{\mathrm{M}}$. To validate these data from a structural point of view, we obtained the three-dimensional structure of the F133L mutant in both oxidized and reduced state (2.2 and 3.2 Å, respectively) and that of the D236G in the oxidized state at 3.5 Å resolution. However, the obtained structures did not highlight significant conformational changes with respect to the wild type protein.

Thus, we focused on the newly discovered interaction between AIF and CHCHD4, evaluating the impact of pathogenic AIF mutations on the complex formation with the partner protein with a combination of biophysical techniques, namely Microscale Thermophoresis (MST) and structural biology. We set up and optimized a production and purification protocol for CHCHD4 in *E. coli* with final yields of 1.25 mg protein/g of cells. Through analytical SEC we verified the interaction between AIF and CHCHD4, showing for the first time that, in addition to its reduced state, also oxidized AIF can also form a complex with CHCHD4. Hence, MST experiments were performed to measure the affinity of AIF forms, both in the oxidized and the reduced state, for CHCHD4. MST results showed that, upon reduction, AIF acquires a 100-fold increased affinity for CHCHD4, confirming that AIF is a physiological partner of CHCHD4, that their interaction is strongly controlled by the AIF redox state, and that they form a very tight complex when AIF adopts its CT complex/dimeric state. In addition, the G337E replacement impaired significantly this pivotal interaction, showing a 5-fold decreased affinity for the protein partner. This altered feature, coupled to a decreased CT complex stability and a higher susceptibility towards $O_2$, could be viewed as the molecular cause at the basis of the pathogenetic effect of the AIF G337E variant, providing for the first time a possible explanation for the onset of this pathology. To validate the abovementioned data from a structural point of view, we first tried to obtain the structure of AIF-CHCHD4 complex through a crystallographic approach but, probably due the intrinsic disorder of CHCHD4, without success. Next, we tried to gain structural information about the protein complex through the Small-Angle X-ray Scattering (SAXS) technique. SAXS analysis revealed some crucial features about AIF, CHCHD4 and their complex that here we report for the first time.

In first place, AIF SAXS models clearly showed that the crystallographic structure of reduced and dimeric AIF does not reflect the native one in solution, suggesting that probably the protein is forced to crystallize similarly to the oxidized and monomeric form by crystallization conditions. CHCHD4 SAXS models revealed a totally new feature of the protein, showing that it can dimerize and the dimerization process, probably concentration-dependent, occurs through the protein core. Finally, SAXS models of the AIF-CHCHD4 complex revealed a putative interaction region between the proteins, another feature that, until now, was unknown. However, the crystallographic structure of reduced AIF could not be uniquely oriented in the constructed models, making it impossible to identify a precise interaction interface. Nevertheless, in all SAXS models of the protein complex the G337 residue was found in the neighborhood of the identified interacting region, in accordance to MST experiments. In conclusion, our thorough biochemical and biophysical analysis allowed us to indicate the possible molecular bases of the AIF G337E-related mitochondriopathy. In addition, in the course of this study, we set up a protocol that could be used in the future to assess whether new AIF mutations impair the interaction with CHCHD4, a crucial feature for cellular maintenance. The future perspectives of this work include the design small molecules able to interact and stabilize AIF-CHCHD4 complex through *in silico* docking experiments, with a subsequent validation through the MST approach. A second crucial point will be to elucidate the discrepancy between the high-resolution crystal structure and SAXS models of dimeric AIF that emerged during this study. To this aim, we planned to construct hybrid models using high-resolution models either as rigid bodies or adding loops/termini that are not present in the crystal structure.

Such kind of analysis can be performed through software like SASREF[50], CREDO[51], BUNCH[50], EOM[52], SREFLEX[53]. With the same approach we planned also to construct new models of the AIF-CHCHD4 complex, possibly obtaining further structural insights into the protein-protein interacting interface.

Moreover, we planned to identify the possible CHCHD4-interacting region of AIF through a Covalent Labeling approach coupled to Mass Spectrometry, an innovative technique widely used to identify molecular regions engaged in protein-protein complex formation, which could shed new light on the AIF-CHCHD4 interaction.

We hope that our present and future studies will help to provide a better understanding of AIF molecular properties and of its physiopathology, improving the chance to develop therapies for the growing number of diseases to which this important flavoprotein is associated.

# 5. Materials and Methods

***Murine AIF variants production and purification*** - The pKK233-3 vector-based construct for the bacterial overproduction of the wild-type Δ1−101 form of mouse AIF as a fusion with a C-terminal His tag, here named as pKK-AIFΔ101, was described previously[10]. To obtain the D236G, G337E, G261S and the F133L variants of the protein, the corresponding codon changes were introduced into the AIF coding region, using the QuikChange Lightning Site-Directed Mutagenesis Kit (Agilent). Inserts of resulting plasmids were entirely sequenced to verify that mutations were properly introduced and to ensure the absence of unwanted ones. The wild type and mutant forms of His-tagged AIFΔ1−101 were overproduced in *E. coli* strain BL21(DE3) and purified according to the protocol previously reported[10,39] using an ÄKTA-FPLC system (GE Healthcare). The concentration of all AIF forms was determined spectrophotometrically on the basis of an $\varepsilon_{452}$ of 12.54 mM$^{-1}$ cm$^{-1}$.

***Murine CHCHD4 production and purification*** - CHCHD4 cDNA was purchased by Eurofins Genomics and subcloned into a modified pET-21a(+) vector (Novagen, Fig 5.1) carrying the thrombin recognition site and the His-tag at its C-terminal.

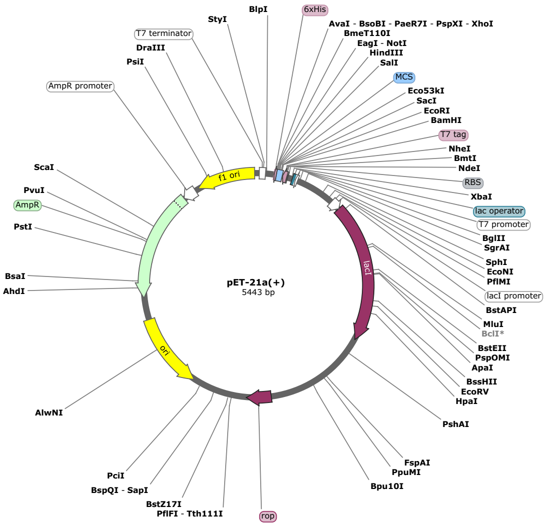

**Fig. 5.1 Map of the pET-21a(+).**

From expression trials, we selected *E. coli* SHuffle strain, which promotes disulfide bond formation in the cytoplasm, for final large scale protein production. Plasmid DNA was amplified and purified through QIAprep Spin Miniprep Kit (QIAGEN), at a final concentration of 102 ng/µl.

SHuffle cells were made competent through the $CaCl_2$ method[54] and transformed adding1 µl of plasmid DNA. Cells were plated at 37 °C overnight in the presence of appropriate antibiotic. Grown cells were used to start a 4.5 L culture at 37 °C. Once it was reached an O.D. of 0.5, protein production was induced with 500 µM IPTG and the cellular growth was performed overnight at a temperature of 25 °C, 220 rpm.

In a typical purification, bacterial cells harvested by centrifugation were resuspended in 20 ml of 50 mM Tris-HCl, pH 8.0, 200 mM NaCl containing 10 mM imidazole (solvent A), supplemented with 1 mM dithiothreitol and 1 mM phenylmethanesulfonyl fluoride (PMSF), and disrupted by sonication. All following purification steps were performed using an ÄKTA-FPLC system (GE Healthcare). The resulting extract was clarified by high-speed centrifugation and applied on two a Ni Sepharose HP column (GE Healthcare) of 5 ml volume each connected in series, equilibrated with solvent A. After extensive washing, initially with solvent A and subsequently with 2% solvent B ( equal to solvent A containing 500 mM imidazole), elution of the recombinant protein was achieved by applying a 2 to 100% gradient of solvent B over 100 mL at a flow rate of 1 ml/min. 2 mM DTT was added to collected fractions. The protein was then loaded on a Superdex 75 10/300 GL column (GE Healthcare) for imidazole/contaminants removal using a 50 mM Tris-HCl, pH 8.0, 200 mM NaCl containing 2 mM DTT at a flow rate of 0.8 ml/min. Protein concentration was spectrophotometrically measured using a $\varepsilon_{280}$ of 11.32 $mM^{-1}$ $cm^{-1}$. CHCHD4 His-tag was removed with thrombin (10 enzymatic units per mg of protein) for 2 h at 37 °C. The reaction was stopped adding 1 mM PMSF. The protein was applied on a Ni Sepharose HP column (GE Healthcare) of 5 ml volume equilibrated with solvent A at a flow rate 1 ml/min. For the final purification step CHCHD4 was loaded on a Superdex 75 10/300 GL column (GE Healthcare) equilibrated with 50 mM Tris-HCl, pH 8.0, 200 mM, 2 mM DTT for imidazole removal and the fractions were concentrated using Amicon Ultra 15 ml Centrifugal Filters (Merck Millipore).

***Spectrophotometric studies*** - A 8453 diode-array spectrophotometer (Agilent) was used for all measurements. Photoreduction experiments were performed at 25 °C using solutions of 15 µM AIF forms in 50 mM sodium phosphate (pH 7.5) containing 15 mM EDTA, 2 µM 5-deaza-5-carba-riboflavin, and 5 µM methyl viologen, as described elsewhere[1] in the presence of 20 µM $NAD^+$. Solutions were made anaerobic within sealed cuvettes by several cycles of vacuum application and $N_2$ flushing and then subjected to successive light irradiation periods using a slide projector lamp. Spectra were recorded after each reduction step, as equilibrium conditions were established under dark conditions.

Pathogenic mutations effect on the AIF CT complex reactivity towards $O_2$ was evaluated incubating a 100 µM AIF solution with 1 mM NADH for 30 min (CT complex formation), then excess of NADH was removed through a PD MidiTrap G-25 (GE Healthcare) and CT complexes reoxidation was spectrophotometrically monitored both at 452 nm and 750 nm. Data analysis performed through the program Grafit 5 (Erithacus Software Ltd.).

***Kinetic studies*** - The NADH—DCIP diaphorase reaction catalyzed by various AIF forms was studied under steady-state conditions at 25 °C in 50 mM sodium phosphate buffer (pH 7.5) and in 100 mM sodium phosphate buffer (pH 8.0). To estimate the kinetic parameters, 1 µM AIF forms were incubated with a varying concentration of NADH (between 0.1 and 3 mM), while that of DCIP was kept constant at 30 µM. The reactions were monitored spectrophotometrically at a wavelength of 600 nm, following DCIP reduction.

All steady-state data, i.e., initial velocity values (v) as a function of the reductant concentration ([S]), were analyzed using Grafit 5 by nonlinear fitting to either of the following equations:

$$v = \frac{\mathrm{V[S]}}{\mathrm{K+[S]}} \qquad \text{eq. 1}$$

and

$$v = \frac{\frac{V}{K}V[S]}{\mathrm{V}+\frac{V}{K}[S]} \qquad \text{eq. 2}$$

Equation 1 was used to analyze data sets showing a conventional saturation behavior, where both the maximal rate (V) and the Michaelis constant (K) could be estimated with reasonable accuracy. Instead, equation 2 was used to analyze data sets in which the ligand concentration was limited to values too much lower than K to allow determination of V, but suitable to accurately estimate the apparent second-order kinetic constant of the process (V/K).

***Analytical SEC and DLS experiments*** - To compare the quaternary structures of the oxidized and $NAD^+$-bound CT complexes of the wild type and pathogenic variants of AIF, protein solutions (40 µM) in 20 mM Tris-HCl buffer (pH 7.5) containing 200 mM NaCl, were incubated in the absence or presence of 1 mM NADH.

Protein samples (~4 nmol) were analyzed on a Superdex 200 increase 10/30 gel filtration column (GE Healthcare) at 8 °C using the same buffer as the mobile phase and a flow rate of 0.5 mL/min (Fig. 5.2). Elution volumes of all AIF variants, in both oxidized and reduced forms, were very similar to those obtained for the wild type protein.

Analytical SEC experiments on the AIF-CHCHD4 were performed using a Superdex 200 increase 10/30 gel filtration column (GE Healthcare). Solutions of 40 µM of wild type AIF were incubated with 50 µM of CHCHD4 in the presence or in the absence of 2 mM NADH.

Analytical SEC experiments to determine the molar ratio of AIF-CHCHD4 association were performed starting from two different wild type AIF aliquots, one at a final concentration of 20 µM and the other of 80µM, which were pre-incubated with 2 mM NADH and then with CHCHD4 at a final concentration of 40 µM. All experiments were performed in 50 mM Tris-HCl, pH 8.0, 200 mM NaCl, 2 mM DTT buffer at a flow rate of 0.5 ml/min.

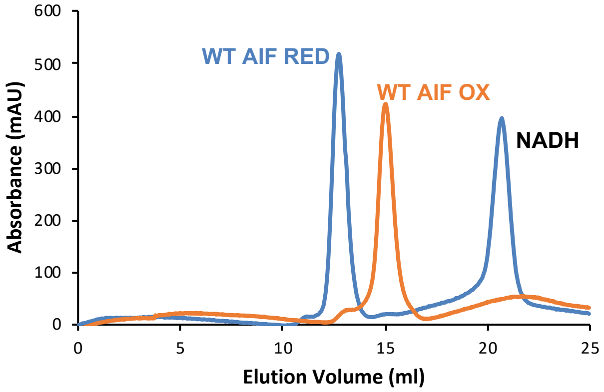

**Fig. 5.2 Analytical SEC performed on wild type AIF.** In the figure the chromatograms of wild type AIF in the oxidized and reduced state (orange and light blue, respectively) are shown. Elution volumes obtained for all tested AIF variants were very similar to those obtained for the wild type protein, suggesting that pathogenic mutations do not alter AIF dimerization.

DLS experiments were performed with a DynaPro instrument (ProteinSolutions, Wyatt Technology Corp.), using solutions of 40 µM AIF forms in phosphate buffer (pH 7.5), at 10 °C in the absence or the presence of 1 µM of NADH (Fig. 5.3A and 5.3B, respectively).

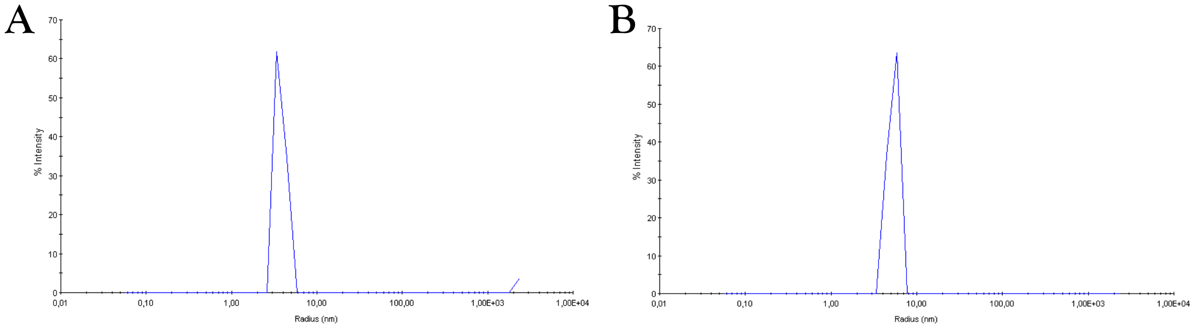

**Fig. 5.3 Dynamic Light Scattering (DLS) experiments performed on wild type AIF.** (**A**) DLS measurements on wild type oxidized AIF showed a hydrodynamic radius of 3.8 nm (estimated molecular weight of 60 kDa). (**B**) DLS measurements on wild type reduced AIF showed a hydrodynamic radius of 5.4 nm (estimated molecular weight of 130 kDa). Hydrodynamic radius values for all tested AIF variants were very similar to those obtained for the wild type protein, suggesting that pathogenic mutations do not alter AIF dimerization.

DLS experiments performed with CHCHD4 were performed preparing a 1 mg/ml protein solution tested in 50 mM Tris-HCl, pH 8.0, 200 mM NaCl, 2 mM DTT at 10 °C. The low temperature for these experiments was chosen to improve the signal-to-noise ratio of DLS measurements.

***Thermal denaturation*** - The conformational stability of the AIF forms was investigated by the ThermoFAD technique[40] using a MiniOpticon System (Bio-Rad Laboratories). Solutions of 13 μM AIF forms in 50 mM sodium phosphate buffer (pH 7.5), both in the absence and in the presence of 1 mM NADH, were subjected to thermal denaturation by increasing the temperature from 15 to 99 °C at a constant rate of 3.33 °C/min. The release of endogenous FAD resulting from protein unfolding was monitored as the increase in fluorescence emission in the range of 540—700 nm.

AIF thermal stability in the presence of CHCHD4/synthetic peptide was evaluated incubating a final concentration of 13 µM AIF with 15 µM CHCHD4/synthetic peptide while, in the case of the reduced form, AIF was pre-incubated with 1 mM NADH for 1 h.

***Crystallization trials*** - Crystallization trials were performed using available commercial crystal screens, using an Oryx-8 crystallization robot (Douglas Instruments). For sitting drop experiments three droplets were dispensed with a final volume of 0.4 µl where protein concentrations were 30%, 50% and 70%, while, in the case of microbatch, one droplet of 0.4 µl final volume with 50% protein.

***Circular Dichroism (CD)*** - CD measurements were performed with a J-810 spectropolarimeter (JASCO Corp., Tokyo, Japan) equipped with a Peltier system for temperature control. All measurements were performed in 50 mM Tris-HCl, pH 8.0, 200 mM NaCl, 2 mM DTT at 0.2 mg/ml protein concentration. All temperature ramps were recorded from 10 to 95 °C (temperature slope 50 °C/hour) in a 0.1 cm path length cuvette and monitored at 220 nm wavelength. Melting temperature was calculated as the minimum of the first-derivative of the traces. Spectra before and after unfolding ramp were recorded (260–190 nm).

***MicroScale Thermophoresis (MST)*** - Experiments were performed using the Monolith NT.155 apparatus (NanoTemper Technologies GmbH, Munich, Germany) and the MO. Affinity Analysis software (NanoTemper Technologies GmbH). We decided to label AIF His-tag with the red fluorescent dye NT-647 using the Monolith NT His-Tag Labeling Kit RAD-tris-NTA (Nano Temper Technologies) according to manufacturer directions, while CHCHD4 was used as the unlabeled titrant.

The titration is predicted to proceed as a classical protein–ligand process, which under equilibrium follows the general equation of a 1:1 complex dissociation:

$$[PL] = \frac{[P]_T + [L]_T + K_d - \sqrt{([P]_T + [L]_T + K_d)^2 - 4[P]_T[L]_T}}{2}$$

where [PL] represents the concentration of the AIF-CHCHD4 complex, $[P]_T$ that of total AIF (both free and ligand bound) and [L] that of total CHCHD4. The His-tagged forms of AIFΔ1-101 were labelled with the red fluorescent dye NT-647 using the Monolith NT His-Tag Labeling Kit RAD-tris-NTA (Nano Temper Technologies) according to manufacturer directions.

AIF was labeled under both its oxidized monomeric and reduced dimeric states. Dye solution was prepared by diluting 1:50 the concentrated dye in 1× PBS-T. AIF was diluted to 200 nM final concentration in 1× PBS-T. Two 100 µl aliquots were prepared containing either no nucleotide or NADH at the final concentration of 500 µM.

After 1 h incubation on ice to allow completion of the reaction between AIF and NADH to generate the CT-complex, 100 µl diluted label solution was added to each protein sample. The labeling reaction was carried out by 30 min incubation at room temperature. The two solution were clarified by centrifugation at 15,000 ×g for 10 min at 4 °C in microfuge.

For each titration experiment, 16 microfuge tubes were prepared and numbered from 1 to 16. In each tube, with the exception of tube 1, a volume of 10 µl of 50 mM Tris-HCl, pH 8.0, 200 mM NaCl, 4 mM DTT was placed. In tube 1, 20 µl of untagged CHCHD4 was added. Next, 10 µl of the content of tube nr. 1 was transferred to tube nr. 2 and its content carefully mixed by pipetting. Then, the operation was repeated by transferring 10 µl of the content of tube nr. 2 to tube nr. 3, and so on until tube nr. 16 was reached. At this point, 10 µl of the solution of tube nr. 16 were discarded in order to have 10 µl 1:1 serial dilutions of CHCHD4 in all test tubes. To complete the samples, 10 µl labeled AIF, in oxidized or in CT complex states, were added to each of the 16 tubes. After extensive mixing by pipetting, the mixtures were transferred to a set of 16 Monolith NT.115 standard treated capillaries (Nano Temper Technologies). MST measurements were performed at the baseline temperature of 24 °C with a fixed concentration of 50 nM AIF, and concentrations of CHCHD4 varied in the 3.85 nM – 126 µM range. Laser excitation power and MST power were set to 20% and 40%, respectively. Concerning the MST experiments performed on reduced AIF in complex with CHCHD4, to unambiguously distinguish between fluorescence changes caused by interaction and those caused by non-specific effects, we performed the EPC test (Fig. 5.4). In the case of His-tag labeling non-specific effects can be caused by interaction of a ligand with the His-tag bound tris-NTA dye (control peptide test) or by ligand-induced aggregation or adsorption to labware (EDTA test). Initial fluorescence was measured for the same samples used during MST experiments (Original Experiment Panel), after EDTA incubation (EDTA panel) and for His6-control peptide incubated with CHCHD4 (Control Peptide panel). Initial fluorescence changes were only detected for samples used during MST measurements, showing a ligand-specific effect.

Synthetic peptide of the first N-terminal 27 residues of CHCHD4 used for MST experiments was synthetized in collaboration with the Department of biochemistry of Milan with the following sequence: MSYCRQEGKDRIIFVTKEDHETPSSAE.

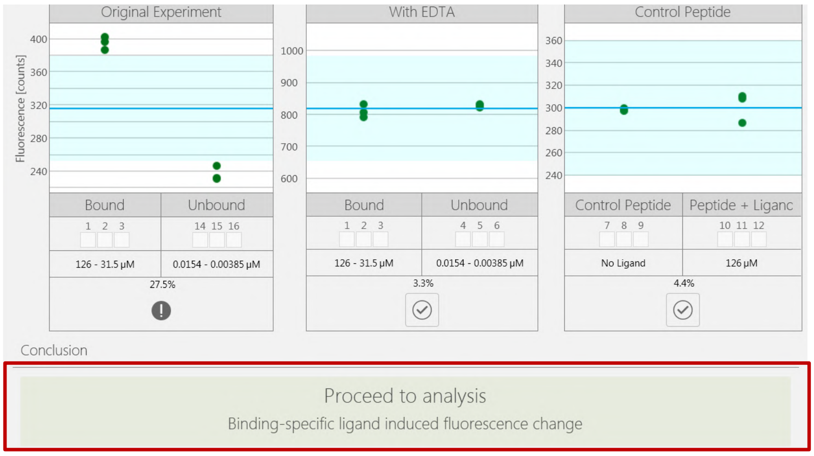

Proceed to analysis

Binding-specific ligand induced fluorescence change

**Fig. 5.4 EPC test performed during MST experiments on reduced wild type AIF in complex with CHCHD4.** Initial fluorescence was measured for the same samples used during MST experiments (Original Experiment Panel), after EDTA incubation (EDTA panel) and for His6-control peptide incubated with CHCHD4 (Control Peptide panel). Initial fluorescence changes were only detected for samples used during MST measurements, showing a ligand-specific effect.

***Small-Angle X-ray Scattering (SAXS) measurements*** - All experiments were performed at the Deutsches Elektronen-Synchrotron (DESY)[55] of Hamburg, Germany. CHCHD4 conservation buffer, 50 mM tris-HCl, pH 8.0, 200 mM NaCl, 2 mM DTT and for SEC-SAXS it was used a Superdex 75 10/300 GL column (GE Healthcare). SAXS data were analyzed with PRIMUS[46] software of ATSAS suite[56] and SEC-SAXS data analysis were performed with CHROMIXS[45]. For each sample, twenty different models were constructed using DAMMIN/F[57,58] software.

Manuscript in preparation

# Alteration of Apoptosis Inducing Factor (AIF)/CHCHD4 interaction: the possible connection to AIF G338E-linked mitochondriopathy

Paolo Cocomazzi[1], Luca Sorrentino[1], Federica Cossu[2], Mario Milani[2], Eloise Mastrangelo[2], Alessandro Aliverti[1]

[1]Department of Biosciences, Università degli Studi di Milano, via Celoria 26, 20133 Milano, Italy.
[2]Biophysics Institute, National Research Council c/o Department of Biosciences, Università degli Studi di Milano, via Celoria 26, 20133 Milano, Italy.

## Abstract

Beside its well characterized apoptotic function, the Apoptosis Inducing Factor (AIF), a highly conserved mitochondrial flavoprotein, can play a pro-vital role in eukaryotic cells interacting with CHCHD4, a mitochondrial protein that regulates oxidative folding of respiratory complexes' subunits. A unique feature of AIF is the ability to form a tight, air-stable charge-transfer complex (CT complex) upon reaction with NAD(H) which leads to protein dimerization, proposed to be pivotal in the AIF signal-transduction pathway. To date, nine point mutations in the human AIF gene (*AIFM1*) were found to cause rare neurodegenerative mitochondriopathies. Here we investigate the molecular basis of the AIF G338E pathogenic mutation, whose connection with pathology onset still has to be clarified. To this aim, a combination of biophysical techniques, Microscale Thermophoresis (MST) and structural biology was used on murine AIF homolog carrying the equivalent mutation (G337E). Our results highlighted a significant faster reoxidation and a lower conformation stability of the G337E mutant with respect to the wild type protein, showing a lower stability of the CT complex species. Through MST approach, for the first time, we quantitatively studied the redox-dependent effects of AIF forms on their affinity for CHCHD4, revealing a possible involvement of the G337 residue in protein complex formation.

We characterized the AIF-CHCHD4 complex also from a structural point of view using the Small-Angle X-ray Scattering (SAXS) analysis, through which we identified a putative interaction region between the two proteins.

In addition, all SAXS models revealed that the solvent-exposed G337 residue is localized in the neighborhood of the identified region, suggesting a possible role of this residue in the protein-protein complex formation. Our results not only provide insights on AIF-CHCHD4 interaction but also shed new light on AIF G338E-linked human mitochondriopathy.

# Introduction

Cellular redox reactions are involved in most forms of neurodegeneration and flavoproteins, ubiquitous redox enzymes, have been implicated in the onset of many of such disorders. The Apoptosis Inducing Factor (AIF)[5,6] is a highly conserved mitochondrial flavoprotein[3,6] that belongs to the glutathione reductase (GR) structural superfamily[59,60] and, in humans, it is encoded by the *AIFM1* gene, located on the X chromosome[20]. The protein is initially synthetized as a precursor apoprotein containing a N-terminal mitochondrial localization sequence[5]. Once in the mitochondrial intermembrane space (IMS), AIF folds and acquires FAD adopting a three-domain structure[7,8]. Mature AIF resides in the IMS tethered to the inner membrane through its N-terminal segment. Upon apoptotic stimuli the AIF membrane-anchoring peptide is cleaved off by cathepsins or calpains, allowing the flavoprotein release from mitochondria and its translocation to the nucleus[61]. Here, AIF binds DNA and recruits various nucleases that lead to chromatin condensation and large-scale DNA degradation in a caspase-independent apoptotic pathway known as parthanatos[62,63]. In addition to its well characterized pro-apoptotic role, there are many evidences of AIF importance for efficient oxidative phosphorylation (OXPHOS)[11,64] and, in this context, the formation of an air-stable $(FADH^-)$-$NAD^+$ charge-transfer complex (CT complex) between AIF and NAD(H) seems to play a pivotal role. CT complex formation triggers major conformational rearrangements causing AIF dimerization, showing that FAD reduction is strictly coupled to the monomer-dimer transition[39]. This led to the hypothesis of a possible AIF role as a redox sensor in the mitochondrial intermembrane space (IMS), an hypothesis validated by the discovery of the interaction between AIF and CHCHD4[9], a mitochondrial protein involved in the import and assembly of substrates implicated in the biogenesis of respiratory chain complexes[26]. However, no specific AIF domains were found to be involved, indicating that the interaction site of the flavoprotein could be conformational. On the other hand, the first N-terminal 27-residues of CHCHD4 were found to be necessary and sufficient for interaction with AIF.

AIF depletion is associated with respiratory chain defects coupled to post-translational downregulation of respiratory chain complexes I, III and VI subunits[22,65–67]. OXPHOS failure is particularly deleterious for the nervous system, being typically associated with neurodegeneration[28,68]. As far as AIF-linked diseases are concerned, to date nine distinct point mutations in the *AIFM1* gene were found as the cause of mitochondriopathies, displaying neurodegeneration as a common symptom[29–31,33–37].

Among them, the G338E replacement[32] was subjected to a previous structural characterization, although the correlation between the point mutation and pathology onset still remains elusive[38]. However, the amino acid replacement was predicted to have functional consequences because it involves residues that interact with the regulatory 510–550 peptide region, whose conformation is regulated by AIF redox state changes and is thought to regulate protein localization, lifetime, post-translational modifications and interactions with other proteins and DNA[32]. In this study, we investigated the effect of the G338E mutation on the biochemical properties of murine AIF, especially on CT complex stability, redox properties and conformational stability. The murine homologue was chosen because its sequence is 92% identical to that of the human one, it is better expressed in *Escherichia coli* and has been more extensively characterized[6].

In addition, we studied AIF interaction with murine CHCHD4 using a combination of biophysical techniques, Microscale Thermophoresis (MST) and structural biology.

Here we report that monomeric and oxidized flavoprotein is able to interact with CHCHD4 and, upon reduction, it acquires an increased affinity for the partner protein. In the reduced and dimeric form of the flavoprotein, the G337E mutation (equivalent to G338E in human) was found to decrease AIF affinity for CHCHD4 by 5-fold. This discovery was further confirmed through Small-Angle X-ray Scattering (SAXS) measurements. In fact, besides providing for the first time a putative AIF interacting region for CHCHD4, the solvent-exposed G337 residue was localized in the neighborhood of the identified region, suggesting its possible implication in AIF-CHCHD4 complex formation.

# Results

We used two different approaches to investigate the effect of the pathogenic G338E replacement[32] on biochemical/biophysical properties of mammalian AIF, using the corresponding mutation in murine AIF (G337E). First, we characterized AIF mutant from a biochemical point of view, studying its CT complex stability towards $O_2$, redox properties and conformational stability. We then focused on the AIF-CHCHD4 interaction combining biophysical technique, MicroScale Thermophoresis (MST) and structural biology. Both wild type and G337E murine AIF forms were produced in *E. coli* cells with comparable yields[39], indicating that the amino acyl replacement does not strongly affect AIF folding. Briefly, the two proteins were purified through two chromatographic steps, a first $Ni^{2+}$ affinity chromatography followed by an anion exchange.

Murine CHCHD4 was overproduced using *E. coli* SHuffle cells (*see* § Material and Methods). The protein was then purified through a $Ni^{2+}$ affinity chromatographic step followed by a size exclusion chromatography (SEC). CHCHD4 His-tag was then cleaved with Thrombin digestion, followed by further purification through $Ni^{2+}$ affinity chromatography.

## Steady-state kinetics of the NADH-diaphorase reaction catalyzed by AIF forms.

AIF is able to catalyze electron transfer from NAD(P)H to 2,6-dichlorophenolindophenol (DCIP), an artificial acceptor, with a modest but significant turnover[10]. We determined the kinetic parameters of the aforementioned reaction as previously reported[39], to investigate the possible impact of the G337E replacement on AIF redox activity. Our results showed a slight perturbation of both the $k_{cat}$ and $K_M$ parameters that resulted 3-fold decreased and 2-fold increased, respectively, with respect to the wild type protein (Fig. 1 and Table 1).

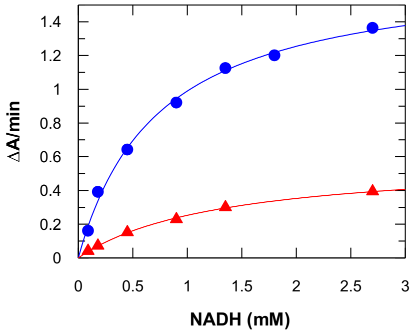

**Fig. 1. NADH-DCIP diaphorase reaction catalyzed by AIF forms.** Kinetics data of the G337E and wild type AIF were collected following DCIP reduction (600 nm) and are depicted in red and blue, respectively.

**Table 1. AIF forms kinetic parameters.**

| AIF | $k_{cat}$ (s$^{-1}$) | $K_m$ (mM) |
|---|---|---|
| Wild type | 1.31 ± 0.04 | 0.73 ± 0.07 |
| G337E | 0.43 ± 0.01 | 1.32 ± 0.08 |

**Kinetics of CT complex oxidation.** It is known that AIF CT complex engaged with NAD(H) is very stable to $O_2$ oxidation. We studied the effect of the G337E replacement on CT complex reactivity towards $O_2$ as described elsewhere[39]. Our results showed that, upon removal of NADH excess, the CT complex reoxidation occurs 8-fold faster with respect to the wild type protein, suggesting an involvement of this residue in CT complex species stabilization (Fig. 2 and Table 2).

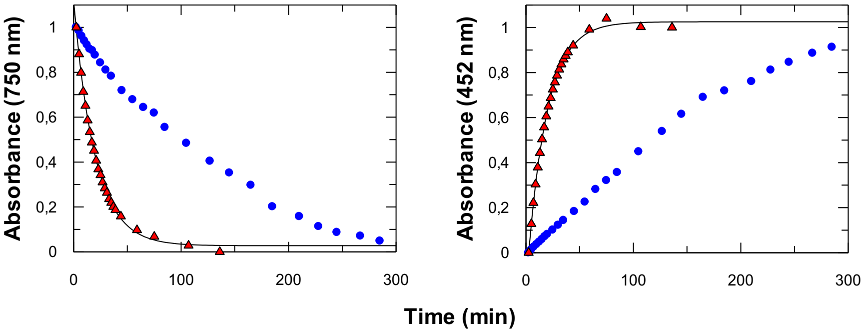

**Fig. 2. AIF forms CT complex stability towards $O_2$.** Upon removal of NADH excess, CT complexes reoxidation was spectrophotometrically monitored at 750 nm for oxidized AIF (**left**) and at 452 nm for AIF in the CT complex state (**right**). AIF G337E and wild type forms are shown in red and blue, respectively.

*Table 2. Half-life of AIF forms CT complex upon NADH removal.*

| AIF | t/2 (min) |
|---|---|
| Wild type | 125 |
| G337E | 15 |

**Thermostability of the CT complex engaged by AIF forms.** We assessed AIF forms conformational stability through the ThermoFAD technique[40]. Thermal denaturation studies showed a slightly decreased conformational stability for the G337E variant in its monomeric oxidized state, corresponding to a melting temperature lower than that of the wild type protein by 2 °C (Fig. 3A). Instead, formation of the CT complex upon reaction between AIF G337E and NADH was accompanied by a 6 °C decrease in the melting temperature if compared to that of the wild type protein (Fig. 3B). Thermal stability evaluation (Table 3) showed that redox-dependent conformational changes have a significant destabilizing impact on conformation stability of reduced AIF, in accordance with our results on CT complex oxidation rate.

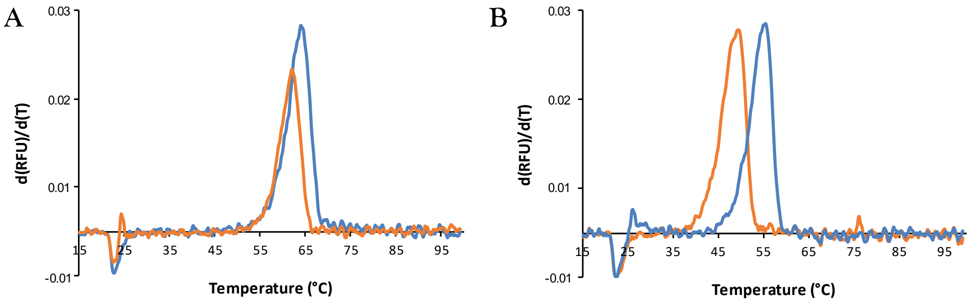

**Fig. 3. Conformational stability of the AIF forms.** (**A**) In the oxidized state, the G337E mutant (orange curve) showed a decreased melting temperature by 2 °C when compared to the oxidized wild type one (light blue curve). (**B**) In the presence of NADH excess, the mutant (orange curve) showed a decreased melting temperature by 6 °C with respect to the oxidized wild type one (light blue curve).

**Table 3. AIF forms melting temperatures measured through the ThermoFAD technique.**

| AIF | $T_m^{OX}$ (°C) | $T_m^{RED}$ (°C) |
|---|---|---|
| Wild type | 63.8 ± 0.1 | 55.4 ± 0.2 |
| G337E | 61.8 ± 0.2 | 49.4 ± 0.1 |

**Analytical SEC of AIF-CHCHD4 complexes.** Since the biochemical and biophysical characterization of the AIF G337E variant did not reveal a clear cause for its pathogenic effect, we focused our attention on the recently discovered interaction between AIF and CHCHD4. As a first approach, complex formation between AIF and CHCHD4 was investigated by analytical SEC. For this analysis, wild-type AIF, in both its oxidized and reduced state, was incubated in the absence or in the presence of a small molar excess of CHCHD4. Fig. 4A reports the superposed chromatograms of the oxidized/monomeric AIF alone and after incubation with CHCHD4 (light blue and orange traces, respectively). As it can be seen, the significant shift of about 500 µl induced by the presence of CHCHD4 in the elution volume of AIF suggests that the interaction between the two proteins occurred, yielding a relatively tight, long-lived complex that persisted during chromatography. The experiment was replicated using AIF pre-incubated with NADH, to induce its CT complex/dimeric state. The superposed chromatograms of reduced AIF alone and after incubation with CHCHD4 (light blue and orange, respectively) are reported in Fig. 4 B. In this case, a larger shift of about 1 ml in the elution volume was detected, confirming that also reduced/dimeric AIF is able to interact with its partner protein.

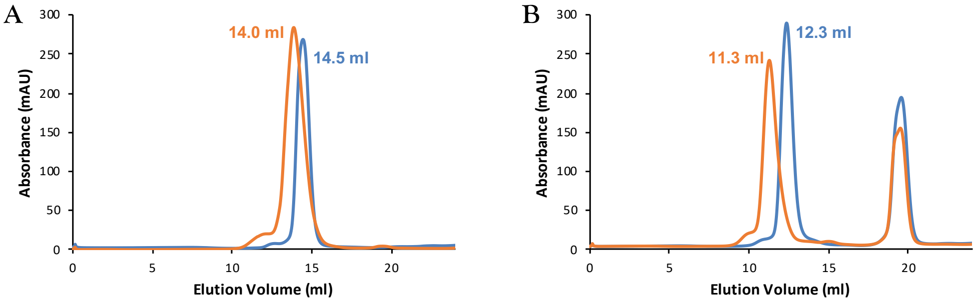

**Fig. 4. Analytical SEC experiments on wild type AIF-CHCHD4 interaction.** (**A**) Superposed chromatograms of oxidized AIF (light blue) and oxidized AIF in complex with CHCHD4 (orange). (**B**) Superposed chromatograms of reduced AIF (light blue) and reduced AIF in complex with CHCHD4 (orange). Elution volumes are reported close to the corresponding peak.

**Effect of CHCHD4 binding on wild type AIF conformational stability.** We investigated possible alterations induced by CHCHD4 binding on the conformational stability of wild type AIF, both in the oxidized and the in the reduced forms, through the ThermoFAD technique. Fig. 5 clearly shows that CHCHD4 binding had a significant destabilizing effect on AIF, whose melting temperature resulted 8 °C lower with respect to oxidized AIF alone. Instead, no differences in thermal stability terms were detected in the case of reduced AIF after incubation with the partner protein (Fig. 5B, orange and blue curves, respectively).

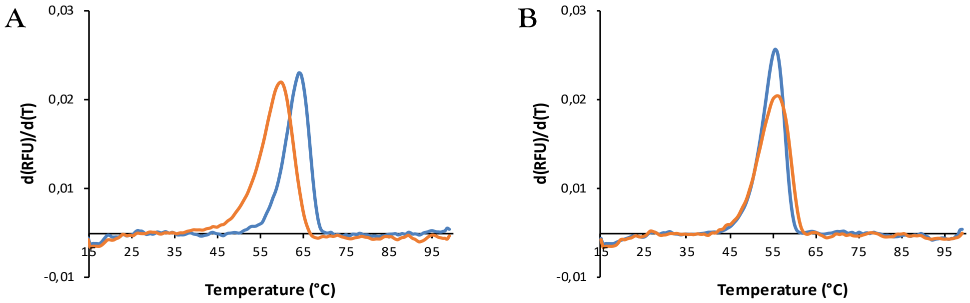

**Fig. 5. Effect of CHCHD4 binding on AIF conformational stability.** (**A**) Thermal denaturation profiles of oxidized AIF and oxidized AIF incubated with CHCHD4 are represented in light blue and orange, respectively. (**B**) Thermal denaturation profiles of reduced AIF and reduced AIF incubated with CHCHD4 are represented in light blue and orange, respectively.

**MicroScale Thermophoresis (MST).** Since we confirmed that the two proteins were able to form a protein-protein complex through analytical SEC and ThermoFAD technique, we investigated the strength of their interaction using MST measurements. More in detail, we verified the interaction of wild type and G337E AIF forms, both in the oxidized and reduced state, with CHCHD4. In Fig. 6A the capillary scan of CHCHD4 titration of wild type AIF in its oxidized and monomeric state is reported, showing that protein-protein interaction induced no fluorescence quenching while a clear effect on MST was detected in a dose-dependent fashion (Fig. 6B). Interpolation of MST data (Fig. 6C) yielded a $K_d$ value of 13 ± 2 µM for oxidized AIF/CHCHD4 protein complex. Identical results were obtained using the G337E AIF variant (Table 4).

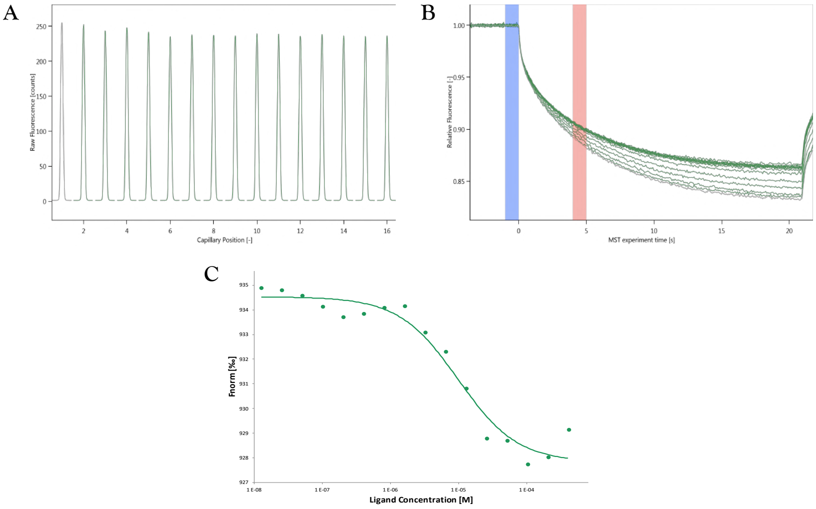

**Fig. 6. MicroScale Thermophoresis on wild type AIF in the oxidized form in complex with CHCHD4.** (**A**) Capillary scan showed constant initial fluorescence along all MST samples. (**B**) MST traces. From light blue interval was measured initial fluorescence intensity during capillary scan while the salmon red interval represents the region where the thermophoretic effect was exploited for $K_d$ calculation. (**C**) Interpolation of MST data.

The same procedure was repeated in the presence of an excess of NADH, to trigger AIF reduced homodimeric quaternary structure. However, in this case, a significant enhancement in fluorescence emission induced by CHCHD4 binding was detected during capillary scan (Fig. 7A), suggesting a change in the fluorophore environment caused by protein-protein interaction. In this case, the raw fluorescence variation recorded during the capillary scan was exploited for data interpolation. Nevertheless, also in this case, CHCHD4 binding induced a significant thermophoretic effect (Fig. 7B). Interpolation of data points (Fig. 7C) yielded a $K_d$ value of 85 ± 15 nM for reduced AIF/CHCHD4 complex, i.e. a 100-fold increased affinity for CHCHD4 upon AIF reduction and dimerization. Similarly, we tested the affinity of the G337E variant for CHCHD4, revealing a 5-fold decreased affinity for CHCHD4 when the mutant is in the reduced and dimeric form, with a $K_d$ of 425 ± 75 nM.

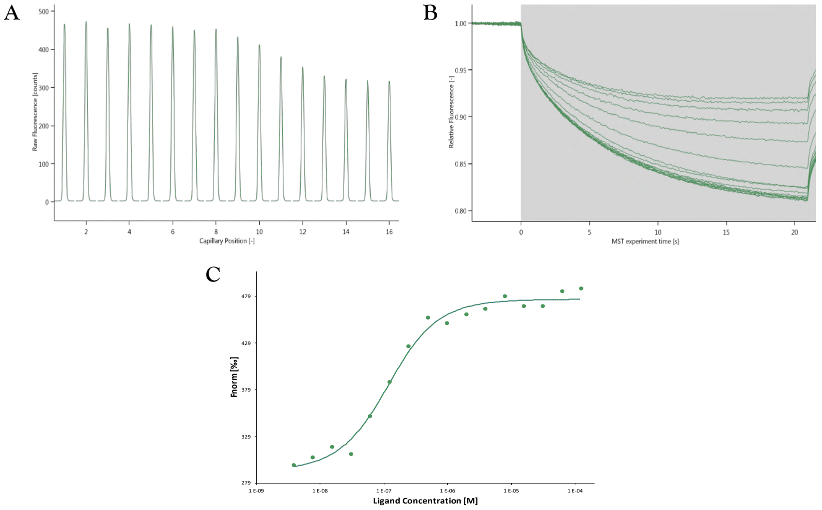

**Fig. 7. MicroScale Thermophoresis on wild type AIF in the reduced form in complex with CHCHD4.** (**A**) Capillary scan showed an initial fluorescence variation induced by ligand binding. (**B**) Initial fluorescence variation was used for $K_d$ calculation instead of MST, although the thermophoretic effect is clearly detectable. (**C**) Interpolation of initial fluorescence data from which a $K_d$ of 85 ± 15 nM was estimated.

**Table 4. $K_d$ values of AIF variants in both their oxidized and reduced forms for HCHCD4.** The reduced G337E mutant showed a 5-fold decreased affinity for CHCHD4.

| AIF | $K_d^{OX}$ (µM) | $K_d^{RED}$ (nM) |
|---|---|---|
| Wild type | 13 ± 2 | 85 ± 15 |
| G337E | 13 ± 4 | 425 ± 75 |

**Small-Angle X-ray Scattering (SAXS) analysis.** To validate MST data from a structural point of view and to identify a putative AIF interacting region for the partner protein, we studied the wild type AIF-CHCHD4 complex through the Small-Angle X-ray Scattering (SAXS) technique. More in detail, we used both batch mode and SEC-SAXS to construct low resolution models of dimeric AIF and dimeric AIF complexed with CHCHD4. We then superimposed the two models to highlight regions where CHCHD4 molecule(s) could be accommodate.

## SAXS characterization of AIF in its reduced and dimeric form

We first analyzed AIF in its reduced and dimeric form through the batch mode, preparing five serial dilutions of AIF (from 16 to 0.5 mg/ml) all pre-incubated with 2 mM NADH. We selected the 2 mg/ml protein concentration for further analyses and model construction. Bayesian molecular weight was consistent with the dimeric assembly and other parameters calculated with PRIMUS are reported in Table 5.

**Table 5. Structural parameters of reduced CT complex AIF calculated with PRIMUS.** Data obtained through batch mode were consistent with the dimeric form of AIF.

| $R_g$ (nm) | Bayesian MW range (kDa) | Expected MW (kDa) | $D_{max}$ (nm) |
|---|---|---|---|
| 3.8 ± 0.1 | 116 – 142 | 114 | 13.1 |

We compared experimental and calculated data (from PDB 3GD4[41]) (shown in green and blue, respectively) with CRYSOL software, whose results (Fig. 8A) showed a significant discrepancy with a $\chi^2$ value of 75, probably due to incompleteness of PDB coordinates. Analysis of flexibility/unfolding degree through the Kratky plot resulted to be typical of globular multidomain proteins (Fig. 8B).

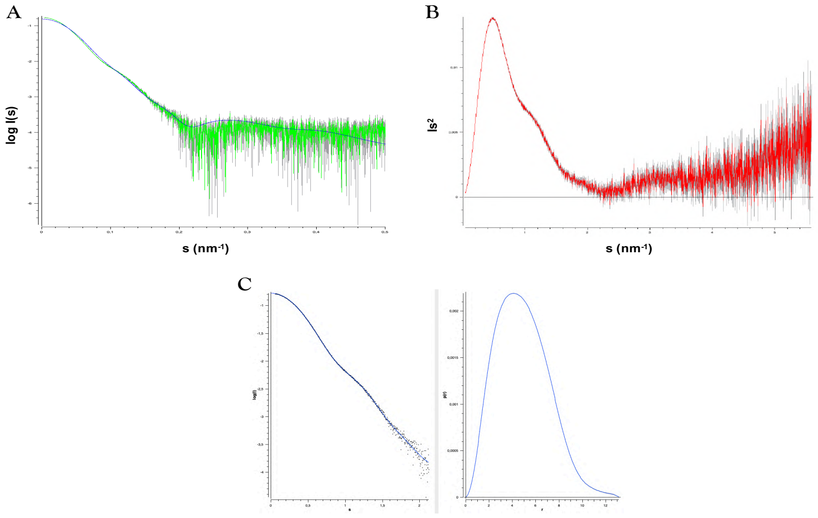

**Fig. 8. Crystallographic structure-SAXS data comparison and flexibility/unfolding degree analysis.** (**A**) Available crystallographic structure of reduced AIF (PDB: 3GD4) was compared with SAXS data (in blue and green, respectively) through CRYSOL software. (**B**) Kratky plot. (**C**) Pair distance distribution calculated from $D_{max}$ (right) and the corresponding fitting (left).

We used DAMMIF for construction of *ab initio* models, assuming a P1 or P2 symmetry. The quality of the most representative model constructed in P1 and P2 symmetry was comparable but, since we expected the P2 symmetry for the dimeric form of AIF, we considered P2 symmetry models for further analysis. We superimposed the most representative P2 symmetry model on the available high resolution structure of murine reduced AIF (PDB 3GD4[41]) using SUPCOMB. Superimposition was evaluated through the Normalized Spatial Discrepancy (NSD) which tends to 1 for ideally superimposed similar objects. Interestingly, high resolution data fitting within SAXS models was not optimal, with NSD value of 3.3 and showing significantly large AIF regions protruding outside the model (Fig. 9A).

This was a relevant feature suggesting that, in the crystal structure, reduced AIF adopts a different conformation, probably induced by crystallographic restraints. To verify the results obtained with the batch mode, a solution of 16 mg/ml AIF, pre-incubated with 2 mM NADH, was analyzed through SEC-SAXS measurements. The *ab initio* models built using SEC-SAXS data showed the same overall features as those obtained with the batch mode (data not shown), confirming that in solution reduced AIF adopts a different conformation with respect to the crystallographic one (Fig. 9B).

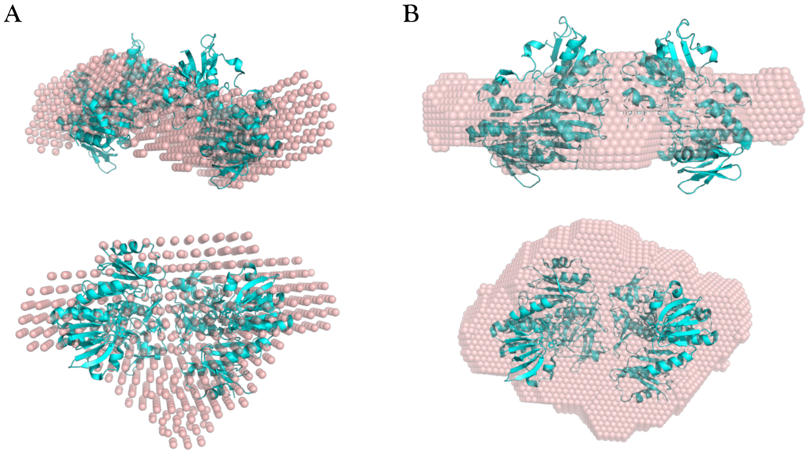

**Fig.9. SAXS models of reduced AIF.** Models constructed from batch mode (**A**) and SEC-SAXS experiments (**B**) were superimposed to the available crystallographic structure of reduced AIF (PDB 3GD4). In both cases, significant portions of the crystallographic structure were not described by the SAXS model, suggesting that in solution AIF could adopt a different conformation with respect to the crystallographic one. Upper and lower panels show top and front view of the SAXS model, respectively.

## SAXS characterization of reduced AIF in complex with CHCHD4

We characterized the AIF-CHCHD4 complex using both batch mode and SEC-SAXS. For the batch mode, five serial dilutions of AIF (9.80 to 0.31 mg/ml, all pre incubated with 4 mM NADH) in complex with CHCHD4 (3.1 to 0.6 mg/ml) were prepared. We selected that at 2.46 mg/ml AIF for further analyses and models construction. Estimated structural parameters as $R_g$ and Bayesian molecular weight were consistent with the heterotetrameric complex under investigation (Table 6) and the Kratky plot was typical for multidomain proteins with a flexible linker (Fig. 10A).

**Table 6. Structural parameters of reduced AIF in complex with CHCHD4 calculated with PRIMUS.** Data obtained through batch mode were consistent with the protein complex.

| **$R_g$ (nm)** | **Bayesian MW range (kDa)** | **Expected MW (kDa)** | **$D_{max}$ (nm)** |
|---|---|---|---|
| 4.4 ± 0.3 | 127 – 162 | 146 | 20.6 |

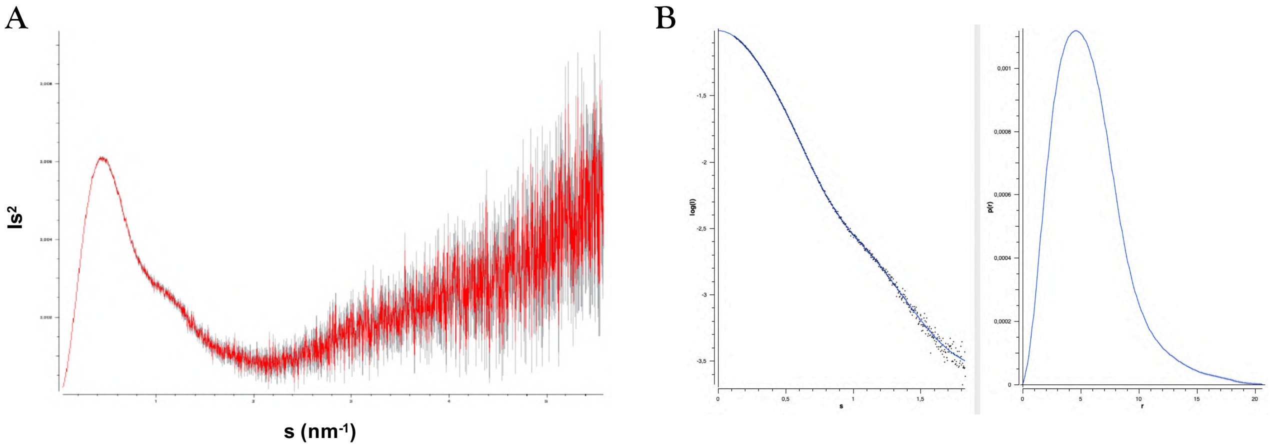

**Fig. 10. Flexibility/unfolding degree analysis.** (**A**) Kratky plot was typical of multidomain proteins with a flexible linker. (**B**) Pair distance distribution calculated from $D_{max}$ (right) and the corresponding fitting (left).

Models construction was performed assuming P1 or P2 symmetry. Similarly to what observed for AIF in the dimeric form, the quality of the most representative model constructed in P1 and P2 symmetry was comparable but, since we expected the P2 symmetry for the protein-protein complex, we considered P2 symmetry models for further analysis.

Superimposition of the most representative model to that of reduced AIF obtained in batch mode, with a final NSD value of 0.9 (Fig 11A, in hot pink and cyan, respectively), revealed two symmetric regions exclusively present in the AIF-CHCHD4 complex model and, thus, possibly representing a putative interaction region between the two proteins (red arrows in Fig. 11A). We then superimposed SAXS models with high resolution data of reduced AIF (Fig. 11B) noting that the G337 residue, indicated by the red arrow, is located in the neighborhood of the putative AIF/CHCHD4 interacting region.

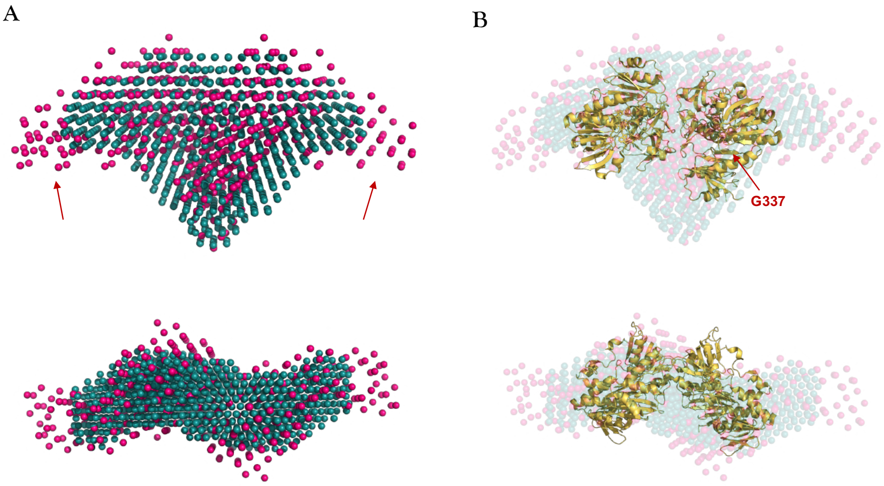

**Fig. 11. SAXS models superimposition of reduced AIF (cyan) and reduced AIF in complex with CHCHD4 (hot pink).** (**A**) Red arrows indicate the two specular regions exclusively present in the AIF-CHCHD4 complex model (hot pink) where CHCHD4 could be accommodated. (**B**) Superimposition of reduced AIF-CHCHD4 complex models to reduced AIF crystallographic structure. The G337 residue is located in the neighborhood of the putative interacting region between the two proteins. Upper and lower panels show front and top view of the SAXS model, respectively.

Subsequently, to validate the data obtained in batch mode, new SEC-SAXS measurements on the reduced AIF in complex with CHCHD4 were performed (AIF at 9.8 mg/ml incubated with CHCHD4 3.1 mg/ml). Structural parameters reported in Table 7 were very similar to those observed for the batch mode and consistent with the expected size and molecular weight of the reduced AIF-CHCHD4 complex.

| $R_g$ (nm) | Bayesian MW range (kDa) | Expected MW (kDa) | $D_{max}$ (nm) |
|---|---|---|---|
| 4.2 ± 0.2 | 127 – 162 | 146 | 17.1 |

**Table 7. Structural parameters of reduced AIF in complex with CHCHD4 calculated with PRIMUS.** Similarly batch mode results, data obtained through SEC-SAXS were consistent with the protein heterotetrameric complex.

Construction of new models performed imposing a P1 or a P2 symmetry gave similar $\chi^2$ values of 1.09 and 1.08, respectively. Nevertheless, only models in P2 symmetry were considered for further analyses. The most representative model was superimposed to that of reduced AIF obtained with SEC-SAXS with a final NSD value of 1.06. Very similarly to what observed in the previous model, superimposition revealed the same two specular regions that could accommodate two CHCHD4 monomers (red arrows in Fig. 12A). Unfortunately, comparison of SAXS models with high resolution data (Fig. 12B) revealed a different orientation of reduced AIF crystallographic structure, suggesting again that the crystal structure of reduced AIF does not completely reflect that of the protein in solution.

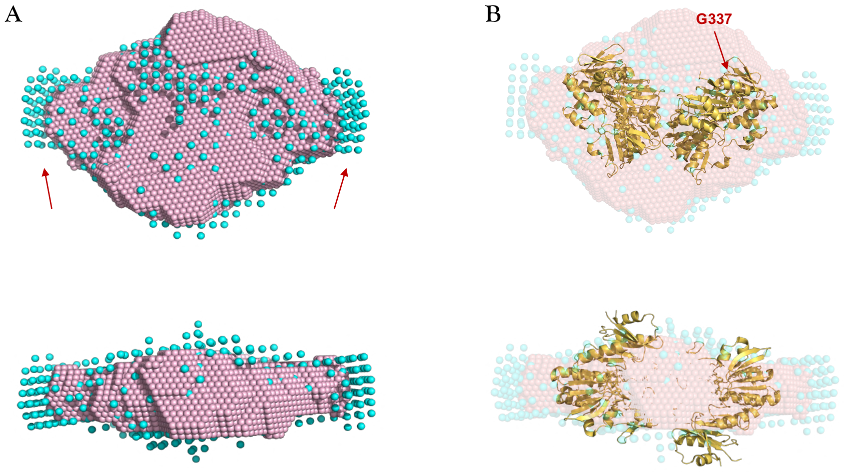

**Fig. 12. SEC-SAXS models superimposition of reduced AIF (salmon) and reduced AIF in complex with CHCHD4 (light blue).** (**A**) Red arrows indicate the two specular regions exclusively present in the AIF-CHCHD4 complex model (light blue) where CHCHD4 could be accommodated. (**B**) Superimposition of reduced AIF-CHCHD4 complex models to reduced AIF crystallographic structure which, although, was oriented differently with respect to batch mode results. This suggest again that high resolution data of reduced AIF do not reflect completely its conformation in solution. Nevertheless, the G337 residue is located again in the neighborhood of the putative interacting region between the two proteins. Upper and lower panels show front and top view of the SAXS model, respectively.

## Discussion

Through this study we were able to gain new insights into the little-known AIF pro-survival role and into the molecular mechanisms that drive its interaction with CHCHD4. Our results show that AIF G338E pathogenic mutation leads to only slight alterations on the biochemical properties of the protein, suggesting that the molecular basis of mitochondriopathy onset have a more complicated pathway. In fact, our results showed slight perturbation induced by the murine AIF G337E mutation on both $k_{\mathrm{cat}}$ and $K_{\mathrm{M}}$ parameters that, in comparison to the wild type protein, resulted 3-fold decreased and 2-fold increased, respectively. However, these changes in the biochemical parameters were comparable to those of the wild type protein, suggesting that the pathogenic mutation does not significantly alter AIF redox activity. Evaluation of CT complex reactivity towards $O_2$ revealed an 8-fold faster reoxidation of AIF G337E mutant with respect to the wild type protein. This significant effect suggests that the G337E mutation alters the dissociation rate of $NAD^+$, possibly leading to a lower half-life of reduced species. Thermal denaturation studies showed a decreased melting temperature for the reduced form of the mutated protein, suggesting that mutant redox-dependent conformational changes have a larger destabilizing impact on conformation stability in comparison to the wild type protein. These results are in accordance with our result on CT complex oxidation rate, showing that the G337E replacement affects CT complex stability rather than its formation. However, a decreased conformational stability and a lower CT complex stability can partially hamper AIF pro-survival functions, but they do not fully provide an explanation for mitochondriopathy onset. Since the biochemical characterization of the G337E mutant was not sufficient to find out a clear connection between the mutation and the associated human mitochondriopathy, we focused on the recently discovered interaction between AIF and CHCHD4. To verify the interaction between the two proteins we performed analytical SEC experiments incubating wild type AIF, both in the oxidized and reduced forms, with CHCHD4. Our results clearly showed that AIF, in both redox states, is able to form a stable protein complex with CHCHD4 as significant variations in the elution volumes were detected in both cases. We also assessed the impact of CHCHD4 binding on the AIF conformational stability through the ThermoFAD technique. The melting temperature of oxidized AIF resulted 8 °C lower with respect to oxidized AIF alone, showing that CHCHD4 binding has a similar destabilizing effect of that induced by NADH binding. Instead, no differences in thermal stability terms were detected in the case of reduced AIF incubated with CHCHD4 with respect to reduced AIF alone.

The latter result is coherent with background information: reduced AIF should be the physiologic partner of CHCHD4 to promote cell survival and, thus, we did not expect a significant destabilizing effect as seen for the oxidized form of the protein. Since we verified the interaction between wild type AIF and CHCHD4, we investigated the strength of their association through the MicroScale Thermophoresis. MST results revealed that monomeric oxidized AIF has an affinity of 13 ± 2 μM for CHCHD4 while, upon reduction, it acquires a 100-fold increased affinity ($K_d$:85 ± 15 nM). Such a significant change in the affinity for CHCHD4 strongly suggests that this interaction is mainly driven by AIF regions which undergo conformational rearrangements upon CT complex formation as, for example, its C-terminal domain.

MST results of the G337E mutant, performed in the same conditions as the wild type protein, highlighted a 5-fold decreased affinity for CHCHD4 when the mutant is in the reduced and dimeric form, with a calculated $K_d$ value of 425 ± 75 nM. Such an effect is not a drastic one, suggesting that the G337 residue is not directly involved in the interaction region but rather in its neighborhood.

We validated this hypothesis from a structural point of view using the Small-Angle X-ray Scattering (SAXS) technique. The comparison of SAXS models constructed for reduced dimeric AIF and reduced AIF in complex with CHCHD4 revealed for the first time a putative interaction region between the two proteins. However, high resolution data fitting within SAXS models was not optimal, showing significantly large AIF regions protruding outside the model. This was a relevant feature suggesting that, in the crystal structure, reduced AIF adopts a different conformation, probably induced by crystallographic restraints. In addition, comparison of SEC-SAXS and batch mode models with high resolution data showed that the crystallographic structure of reduced AIF was superimposed on the SAXS model in a different orientation, suggesting again that the crystal structure of reduced AIF does not completely reflect that of the protein in solution. Discrepancy between high resolution data and SAXS models made it impossible to precisely identify the interacting region between the two proteins. Nevertheless, in all the models from both batch and SEC-SAXS experiments, the G337 residue was found to be located in the neighborhood of the putative interaction region between the two proteins. Since the residue is solvent-exposed, it could contact the N-terminal 27 amino acids of CHCHD4 and/or cause local conformational rearrangements leading to a decreased affinity for CHCHD4 as a consequence of the G337E replacement. Interestingly, SAXS models of the AIF-CHCHD4 complex constructed both in P1 and P2 symmetry revealed two different and specular regions where CHCHD4 could interact with AIF.

This suggests a molar ratio of 1:1 between oxidized monomeric AIF and CHCHD4, in accordance with our predictions based on previously described analytical SEC experiments. Taken together, our results strongly suggest that the G338E replacement in human AIF leads to a combination of effects (a lower affinity for CHCHD4, a decreased CT complex stability and a higher CT complex susceptibility towards $O_2$) that could trigger or exasperate the clinical symptoms the associated neurodegenerative mitochondriopathy.

## Materials and methods (Manuscript)

***Murine AIF variants production and purification*** - The pKK233-3 vector-based construct for the bacterial overproduction of the wild type Δ1−101 form of mouse AIF as a fusion with a C-terminal His tag, here named as pKK-AIFΔ101, was described previously[10]. To obtain the D236G, G337E, G261S and the F133L variants of the protein, the corresponding codon changes were introduced into the AIF coding region, using the QuikChange Lightning Site-Directed Mutagenesis Kit (Agilent). Inserts of resulting plasmids were entirely sequenced to verify that mutations were properly introduced and to ensure the absence of unwanted ones. The wild type and mutant forms of His-tagged AIFΔ1−101 were overproduced in *E. coli* strain BL21(DE3) and purified according to the protocol previously reported[10,14] using an ÄKTA-FPLC system (GE Healthcare). The concentration of all AIF forms was determined spectrophotometrically on the basis of an $\varepsilon_{452}$ of 12.54 $mM^{-1}$ $cm^{-1}$.

***Murine CHCHD4 production and purification*** - CHCHD4 cDNA was purchased by Eurofins Genomics and subcloned into a modified pET-21a(+) vector (Novagen, Fig. 13) carrying the thrombin recognition site and the His-tag at its C-terminal. From expression trials, we selected *E. coli* Shuffle strain for final large scale protein production, which promotes disulfide bond formation in the cytoplasm. Plasmid DNA was amplified and purified through QIAprep Spin Miniprep Kit (QIAGEN), at a final concentration of 102 ng/µl. SHuffle cells were made competent through the $CaCl_2$ method[54] and transformed adding1 µl of plasmid DNA. Cells were plated at 37 °C overnight in the presence of appropriate antibiotic. Grown cells were used to start a 4.5 L culture at 37 °C. Once it was reached an O.D. of 0.5, protein production was induced with 500 µM IPTG and the cellular growth was performed overnight at a temperature of 25 °C, 220 rpm.

In a typical purification, bacterial cells harvested by centrifugation were resuspended in 20 ml of 50 mM Tris-HCl, pH 8.0, 200 mM NaCl containing 10 mM imidazole (solvent A), supplemented with 1 mM dithiothreitol and 1 mM phenylmethanesulfonyl fluoride (PMSF), and disrupted by sonication. All following purification steps were performed using an ÄKTA-FPLC system (GE Healthcare). The resulting extract was clarified by high-speed centrifugation and applied on two a Ni Sepharose HP column (GE Healthcare) of 5 ml volume each connected in series, equilibrated with solvent A.

After extensive washing, initially with solvent A and subsequently with 2% solvent B ( equal to solvent A containing 500 mM imidazole), elution of the recombinant protein was achieved by applying a 2 to 100% gradient of solvent B over 100 mL at a flow rate of 1 ml/min. 2 mM DTT was added to collected fractions. The protein was then loaded on a Superdex 75 10/300 GL column (GE Healthcare) for imidazole/contaminants removal using a 50 mM Tris-HCl, pH 8.0, 200 mM NaCl containing 2 mM DTT at a flow rate of 0.8 ml/min. Protein concentration was spectrophotometrically measured using a $\varepsilon_{280}$ of 11.32 $mM^{-1}$ $cm^{-1}$. CHCHD4 His-tag was removed with thrombin (10 enzymatic units per mg of protein) for 2 h at 37 °C. The reaction was stopped adding 1 mM PMSF. The protein was applied on a Ni Sepharose HP column (GE Healthcare) of 5 ml volume equilibrated with solvent A at a flow rate 1 ml/min.

For the final purification step CHCHD4 was loaded on a Superdex 75 10/300 GL column (GE Healthcare) equilibrated with 50 mM Tris-HCl, pH 8.0, 200 mM, 2 mM DTT for imidazole removal and the fractions were concentrated using Amicon Ultra 15 ml Centrifugal Filters (Merck Millipore).

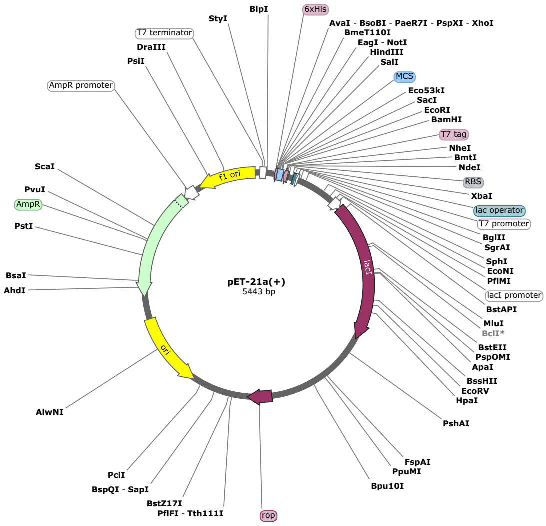

**Fig. 13. Map of the pET-21a(+).**

***Spectrophotometric studies*** - A 8453 diode-array spectrophotometer (Agilent) was used for all measurements. Pathogenic mutations effect on the AIF CT complex reactivity towards $O_2$ was evaluated incubating a 100 μM AIF solution with 1 mM NADH for 30 min (CT complex formation), then excess of NADH was removed through a PD MidiTrap G-25 (GE Healthcare) and CT complexes reoxidation was spectrophotometrically monitored both at 452 nm and 750 nm. Data analysis performed through the program Grafit 5 (Erithacus Software Ltd.).

***Kinetic studies*** - The NADH−DCIP diaphorase reaction catalyzed by various AIF forms was studied under steady-state conditions at 25 °C in 50 mM sodium phosphate buffer (pH 7.5) and in 100 mM sodium phosphate buffer (pH 8.0). To estimate the kinetic parameters, 1 µM AIF forms were incubated with a varying concentration of NADH (between 0.1 and 3 mM), while that of DCIP was kept constant at 30 µM. All steady-state data, i.e., initial velocity values (v) as a function of the reductant concentration ([S]), were analyzed using Grafit 5 by nonlinear fitting to either of the following equations:

$$v = \frac{\mathrm{V[S]}}{\mathrm{K+[S]}} \qquad \text{eq. 1}$$

and

$$v = \frac{\frac{V}{K}V[S]}{\mathrm{V}+\frac{V}{K}[S]} \qquad \text{eq. 2}$$

Equation 1 was used to analyze data sets showing a conventional saturation behavior, where both the maximal rate (V) and the Michaelis constant (K) could be estimated with reasonable accuracy. Equation 2 was instead used to analyze data sets in which the ligand concentration was limited to values too much lower than K to allow determination of V, but suitable to accurately estimate the apparent second-order kinetic constant of the process (V/K).

***Analytical SEC experiments*** - To compare the quaternary structures of the oxidized and NAD$^+$-bound CT complexes of the wild type and pathogenic variants of AIF, protein solutions (40 µM) in 20 mM Tris-HCl buffer (pH 7.5) containing 200 mM NaCl, were incubated in the absence or presence of 1 mM NADH. Protein samples (~4 nmol) were analyzed on a Superdex 200 increase 10/30 gel filtration column (GE Healthcare) at 8 °C using the same buffer as the mobile phase and a flow rate of 0.5 mL/min.

Analytical SEC experiments on the AIF-CHCHD4 complex were performed using a Superdex 200 increase 10/30 gel filtration column (GE Healthcare). Solutions of 40 µM of wild type AIF were incubated with 50 µM of CHCHD4 in the presence or in the absence of 2 mM NADH.

***Thermal denaturation*** - The conformational stability of the AIF forms was investigated by the ThermoFAD technique[40] using a MiniOpticon System (Bio-Rad Laboratories). Solutions of 13 μM AIF forms in 50 mM sodium phosphate buffer (pH 7.5), both in the absence and in the presence of 1 mM NADH, were subjected to thermal denaturation by increasing the temperature from 15 to 99 °C at a constant rate of 3.33 °C/min. The release of endogenous FAD resulting from protein unfolding was monitored as the increase in fluorescence emission in the range of 540—700 nm.

AIF thermal stability in the presence of CHCHD4 was evaluated incubating a final concentration of 13 µM AIF with 15 µM CHCHD4/synthetic peptide while, in the case of the reduced form, AIF was pre-incubated with 1 mM NADH for 1 h.

***MicroScale Thermophoresis (MST)*** - Experiments were performed using the Monolith NT.155 apparatus (NanoTemper Technologies GmbH, Munich, Germany) and the MO. Affinity Analysis software (NanoTemper Technologies GmbH). We decided to label AIF His-tag with the red fluorescent dye NT-647 using the Monolith NT His-Tag Labeling Kit RAD-tris-NTA (Nano Temper Technologies) according to manufacturer directions, while CHCHD4 was used as the unlabeled titrant.

The titration is predicted to proceed as a classical protein–ligand process, which under equilibrium follows the general equation of a 1:1 complex dissociation:

$$[PL] = \frac{[P]_T + [L]_T + K_d - \sqrt{([P]_T + [L]_T + K_d)^2 - 4[P]_T[L]_T}}{2}$$

where [PL] represents the concentration of the AIF-CHCHD4 complex, $[P]_T$ that of total AIF (both free and ligand bound) and [L] that of total CHCHD4.

The His-tagged forms of AIFΔ1-101 were labelled with the red fluorescent dye NT-647 using the Monolith NT His-Tag Labeling Kit RAD-tris-NTA (Nano Temper Technologies) according to manufacturer directions.

AIF was labeled under both its oxidized monomeric and reduced dimeric states. Dye solution was prepared by diluting 1:50 the concentrated dye in 1× PBS-T. AIF was diluted to 200 nM final concentration in 1× PBS-T. Two 100 μl aliquots were prepared containing either no nucleotide or NADH at the final concentration of 500 μM.

After 1 h incubation on ice to allow completion of the reaction between AIF and NADH to generate the CT complex, 100 µl diluted label solution was added to each protein sample. The labeling reaction was carried out by 30 min incubation at room temperature. The two solution were clarified by centrifugation at 15,000 ×g for 10 min at 4 °C in microfuge.

For each titration experiment, 16 microfuge tubes were prepared and numbered from 1 to 16. In each tube, with the exception of tube 1, a volume of 10 µl of 50 mM Tris-HCl, pH 8.0, 200 mM NaCl, 4 mM DTT was placed. In tube 1, 20 µ of untagged CHCHD4 was added. Next, 10 µl of the content of tube nr. 1 was transferred to tube nr. 2 and its content carefully mixed by pipetting. Then, the operation was repeated by transferring 10 µl of the content of tube nr. 2 to tube nr. 3, and so on until tube nr. 16 was reached. At this point, 10 µl of the solution of tube nr. 16 were discarded in order to have 10 µl 1:1 serial dilutions of CHCHD4 in all test tubes. To complete the samples, 10 µl labeled AIF, in oxidized or in CT complex states, were added to each of the 16 tubes. After extensive mixing by pipetting, the mixtures were transferred to a set of 16 Monolith NT.115 standard treated capillaries (Nano Temper Technologies).

MST measurements were performed at the baseline temperature of 24 °C with a fixed concentration of 50 nM AIF, and concentrations of CHCHD4 varied in the 3.85 nM – 126 µM range. Laser excitation power and MST power were set to 20% and 40%, respectively.

***Small-Angle X-ray Scattering (SAXS) measurements*** - All experiments were performed at the Deutsches Elektronen-Synchrotron (DESY)[55] of Hamburg, Germany. CHCHD4 conservation buffer, 50 mM tris-HCl, pH 8.0, 200 mM NaCl, 2 mM DTT and for SEC-SAXS it was used a Superdex 75 10/300 GL column (GE Healthcare). SAXS data were analyzed with PRIMUS[46] software of ATSAS suite[56] and SEC-SAXS data analysis were performed with CHROMIXS[45]. For each sample, twenty different models were constructed using DAMMIN/F[57,58] software.

# References

1. Massey, V. & Hemmerich, P. A photochemical procedure for reduction of oxidation-reduction proteins employing deazariboflavin as catalyst. *J. Biol. Chem.* **252**, 5612–4 (1977).
2. Fraaije, M. W. & Mattevi, A. Flavoenzymes: diverse catalysts with recurrent features. *Trends Biochem. Sci.* **25**, 126–32 (2000).
3. Lorenzo, H. K., Susin, S. A., Penninger, J. & Kroemer, G. Apoptosis inducing factor (AIF): a phylogenetically old, caspase-independent effector of cell death. *Cell Death Differ.* **6**, 516–524 (1999).
4. Daugas, E. *et al.* Apoptosis-inducing factor (AIF): a ubiquitous mitochondrial oxidoreductase involved in apoptosis. *FEBS Lett.* **476**, 118–23 (2000).
5. Susin, S. A. *et al.* Molecular characterization of mitochondrial apoptosis-inducing factor. *Nature* **397**, 441–446 (1999).
6. Sevrioukova, I. F. Apoptosis-Inducing Factor: Structure, Function, and Redox Regulation. *Antioxid. Redox Signal.* **14**, 2545–2579 (2011).
7. Maté, M. J. *et al.* The crystal structure of the mouse apoptosis-inducing factor AIF. *Nat. Struct. Biol.* **9**, 442–446 (2002).
8. Ye, H. *et al.* DNA binding is required for the apoptogenic action of apoptosis inducing factor. *Nat. Struct. Biol.* **9**, 680–684 (2002).
9. Hangen, E. *et al.* Interaction between AIF and CHCHD4 Regulates Respiratory Chain Biogenesis. *Mol. Cell* **58**, 1001–1014 (2015).
10. Churbanova, I. Y. & Sevrioukova, I. F. Redox-dependent Changes in Molecular Properties of Mitochondrial Apoptosis-inducing Factor. *J. Biol. Chem.* **283**, 5622–5631 (2008).
11. Joza, N. *et al.* AIF: Not Just an Apoptosis-Inducing Factor. *Ann. N. Y. Acad. Sci.* **1171**, 2–11 (2009).

12. Czabotar, P. E., Lessene, G., Strasser, A. & Adams, J. M. Control of apoptosis by the BCL-2 protein family: implications for physiology and therapy. *Nat. Rev. Mol. Cell Biol.* **15**, 49–63 (2014).

13. Newmeyer, D. D. *et al.* Bcl-xL does not inhibit the function of Apaf-1. *Cell Death Differ.* **7**, 402–407 (2000).

14. Yuste, V. J. *et al.* Cysteine protease inhibition prevents mitochondrial apoptosis-inducing factor (AIF) release. *Cell Death Differ.* **12**, 1445–1448 (2005).

15. Wang, X., Yang, C., Chai, J., Shi, Y. & Xue, D. Mechanisms of AIF-Mediated Apoptotic DNA Degradation in Caenorhabditis elegans. *Science (80-. ).* **298**, 1587–1592 (2002).

16. Artus, C. *et al.* AIF promotes chromatinolysis and caspase-independent programmed necrosis by interacting with histone H2AX. *EMBO J.* **29**, 1585–1599 (2010).

17. Joza, N. *et al.* Essential role of the mitochondrial apoptosis-inducing factor in programmed cell death. *Nature* **410**, 549–554 (2001).

18. Feraud, O., Debili, N., Penninger, J. M. & Kroemer, G. Cavitation of embryoid bodies requires optimal oxidative phosphorylation and AIF. *Cell Death Differ.* **14**, 385–387 (2007).

19. Klein, J. A. *et al.* The harlequin mouse mutation downregulates apoptosis-inducing factor. *Nature* **419**, 367–74 (2002).

20. Chinta, S. J. *et al.* Reactive oxygen species regulation by AIF- and complex I-depleted brain mitochondria. *Free Radic. Biol. Med.* **46**, 939–947 (2009).

21. Cheung, E. C. C. *et al.* Dissociating the dual roles of apoptosis-inducing factor in maintaining mitochondrial structure and apoptosis. *EMBO J.* **25**, 4061–4073 (2006).

22. Vahsen, N. *et al.* AIF deficiency compromises oxidative phosphorylation. *EMBO J.* **23**, 4679–4689 (2004).

23. Sickmann, A. *et al.* The proteome of Saccharomyces cerevisiae mitochondria. *Proc. Natl. Acad. Sci.* **100**, 13207–13212 (2003).

24. Chacinska, A. *et al.* Essential role of Mia40 in import and assembly of mitochondrial intermembrane space proteins. *EMBO J.* **23**, 3735–3746 (2004).

25. Naoé, M. *et al.* Identification of Tim40 that mediates protein sorting to the mitochondrial intermembrane space. *J. Biol. Chem.* **279**, 47815–21 (2004).

26. Banci, L. *et al.* MIA40 is an oxidoreductase that catalyzes oxidative protein folding in mitochondria. *Nat. Struct. Mol. Biol.* **16**, 198–206 (2009).

27. Sideris, D. P. *et al.* A novel intermembrane space–targeting signal docks cysteines onto Mia40 during mitochondrial oxidative folding. *J. Cell Biol.* **187**, 1007–1022 (2009).

28. Breuer, M. E. *et al.* The role of mitochondrial OXPHOS dysfunction in the development of neurologic diseases. *Neurobiol. Dis.* **51**, 27–34 (2013).

29. Ghezzi, D. *et al.* Severe X-linked mitochondrial encephalomyopathy associated with a mutation in apoptosis-inducing factor. *Am. J. Hum. Genet.* **86**, 639–49 (2010).

30. Berger, I. *et al.* Early prenatal ventriculomegaly due to an AIFM1 mutation identified by linkage analysis and whole exome sequencing. *Mol. Genet. Metab.* **104**, 517–520 (2011).

31. Ardissone, A. *et al.* A slowly progressive mitochondrial encephalomyopathy widens the spectrum of AIFM1 disorders. *Neurology* **84**, 2193–2195 (2015).

32. Diodato, D. *et al.* A novel AIFM1 mutation expands the phenotype to an infantile motor neuron disease. *Eur. J. Hum. Genet.* **24**, 463–466 (2016).

33. Heimer, G. *et al.* Mutations in AIFM1 cause an X-linked childhood cerebellar ataxia partially responsive to riboflavin. *Eur. J. Paediatr. Neurol.* **22**, 93–101 (2018).

34. Kettwig, M. *et al.* From ventriculomegaly to severe muscular atrophy: expansion of the clinical spectrum related to mutations in AIFM1. *Mitochondrion* **21**, 12–8 (2015).

35. Sancho, P. *et al.* A newly distal hereditary motor neuropathy caused by a rare AIFM1 mutation. *Neurogenetics* **18**, 245–250 (2017).

36. Rinaldi, C. *et al.* Cowchock Syndrome Is Associated with a Mutation in Apoptosis-Inducing Factor. *Am. J. Hum. Genet.* **91**, 1095–1102 (2012).

37. Mierzewska, H. *et al.* Spondyloepimetaphyseal dysplasia with neurodegeneration associated with *AIFM1* mutation - a novel phenotype of the mitochondrial disease. *Clin. Genet.* **91**, 30–37 (2017).

38. Sevrioukova, I. F. Structure/Function Relations in AIFM1 Variants Associated with Neurodegenerative Disorders. *J. Mol. Biol.* **428**, 3650–65 (2016).

39. Sorrentino, L. *et al.* Key Role of the Adenylate Moiety and Integrity of the Adenylate-Binding Site for the NAD $^+$ /H Binding to Mitochondrial Apoptosis-Inducing Factor. *Biochemistry* **54**, 6996–7009 (2015).

40. Forneris, F., Orru, R., Bonivento, D., Chiarelli, L. R. & Mattevi, A. *Thermo* FAD, a *Thermofluor* ® -adapted flavin *ad hoc* detection system for protein folding and ligand binding. *FEBS J.* **276**, 2833–2840 (2009).

41. Sevrioukova, I. F. Redox-Linked Conformational Dynamics in Apoptosis-Inducing Factor. *J. Mol. Biol.* **390**, 924–938 (2009).

42. Greenfield, N. J. Using circular dichroism spectra to estimate protein secondary structure. *Nat. Protoc.* **1**, 2876–2890 (2006).

43. Duhr, S. & Braun, D. Why molecules move along a temperature gradient. *Proc. Natl. Acad. Sci.* **103**, 19678–19682 (2006).

44. Wienken, C. J., Baaske, P., Rothbauer, U., Braun, D. & Duhr, S. Protein-binding assays in biological liquids using microscale thermophoresis. *Nat. Commun.* **1**, 100 (2010).

45. Panjkovich, A. & Svergun, D. I. CHROMIXS: automatic and interactive analysis of chromatography-coupled small-angle X-ray scattering data. *Bioinformatics* **34**, 1944–1946 (2018).

46. Konarev, P. V. *et al.* *PRIMUS*: a Windows PC-based system for small-angle scattering data analysis. *J. Appl. Crystallogr.* **36**, 1277–1282 (2003).

47. Svergun, D., Barberato, C., Koch, M. H. J. & IUCr. *CRYSOL* – a Program to Evaluate X-ray Solution Scattering of Biological Macromolecules from Atomic Coordinates. *J. Appl. Crystallogr.* **28**, 768–773 (1995).

48. Kozin, M. B., Svergun, D. I. & IUCr. Automated matching of high- and low-resolution structural models. *J. Appl. Crystallogr.* **34**, 33–41 (2001).

49. Petoukhov, M. V. *et al.* New developments in the *ATSAS* program package for small-angle scattering data analysis. *J. Appl. Crystallogr.* **45**, 342–350 (2012).

50. Petoukhov, M. V. & Svergun, D. I. Global rigid body modeling of macromolecular complexes against small-angle scattering data. *Biophys. J.* **89**, 1237–1250 (2005).

51. Petoukhov, M. V., Eady, N. A. J., Brown, K. A. & Svergun, D. I. Addition of missing loops and domains to protein models by x-ray solution scattering. *Biophys. J.* **83**, 3113–3125 (2002).

52. Tria, G., Mertens, H. D. T., Kachala, M. & Svergun, D. I. Advanced ensemble modelling of flexible macromolecules using X-ray solution scattering. *IUCrJ* **2**, 207–217 (2015).

53. Panjkovich, A. & Svergun, D. I. Deciphering conformational transitions of proteins by small angle X-ray scattering and normal mode analysis. *Phys. Chem. Chem. Phys.* **18**, 5707–5719 (2016).

54. Sambrook, J. & Russell, D. W. Preparation and Transformation of Competent *E. coli* Using Calcium Chloride. *Cold Spring Harb. Protoc.* **2006**, pdb.prot3932 (2006).

55. Blanchet, C. E. *et al.* Versatile sample environments and automation for biological solution X-ray scattering experiments at the P12 beamline (PETRA III, DESY). *J. Appl. Crystallogr.* **48**, 431–443 (2015).

56. Franke, D. *et al.* ATSAS 2.8: A comprehensive data analysis suite for small-angle scattering from macromolecular solutions. *J. Appl. Crystallogr.* (2017). doi:10.1107/S1600576717007786

57. Svergun, D. I. Restoring low resolution structure of biological macromolecules from solution scattering using simulated annealing. *Biophys. J.* **76**, 2879–86 (1999).

58. Franke, D. & Svergun, D. I. *DAMMIF* , a program for rapid *ab-initio* shape determination in small-angle scattering. *J. Appl. Crystallogr.* **42**, 342–346 (2009).

59. Dym, O. & Eisenberg, D. Sequence-structure analysis of FAD-containing proteins. *Protein Sci.* **10**, 1712–1728 (2001).

60. Aliverti, A., Pandini, V., Pennati, A., de Rosa, M. & Zanetti, G. Structural and functional diversity of ferredoxin-NADP+ reductases. *Arch. Biochem. Biophys.* **474**, 283–291 (2008).

61. Otera, H., Ohsakaya, S., Nagaura, Z.-I., Ishihara, N. & Mihara, K. Export of mitochondrial AIF in response to proapoptotic stimuli depends on processing at the intermembrane space. *EMBO J.* **24**, 1375–86 (2005).

62. Aredia, F. & Scovassi, A. I. Poly(ADP-ribose): A signaling molecule in different paradigms of cell death. *Biochem. Pharmacol.* **92**, 157–163 (2014).

63. Susin, S. A. *et al.* Two Distinct Pathways Leading to Nuclear Apoptosis. *J. Exp. Med.* **192**, 571–580 (2000).

64. Norberg, E., Orrenius, S. & Zhivotovsky, B. Mitochondrial regulation of cell death: Processing of apoptosis-inducing factor (AIF). *Biochem. Biophys. Res. Commun.* **396**, 95–100 (2010).

65. Brown, D. *et al.* Loss of Aif function causes cell death in the mouse embryo, but the temporal progression of patterning is normal. *Proc. Natl. Acad. Sci.* **103**, 9918–9923 (2006).

66. Bénit, P., Goncalves, S., Dassa, E. P., Brière, J.-J. & Rustin, P. The Variability of the Harlequin Mouse Phenotype Resembles that of Human Mitochondrial-Complex I-Deficiency Syndromes. *PLoS One* **3**, e3208 (2008).

67. Pospisilik, J. A. *et al.* Targeted Deletion of AIF Decreases Mitochondrial Oxidative Phosphorylation and Protects from Obesity and Diabetes. *Cell* **131**, 476–491 (2007).

68. Swerdlow, R. H. The neurodegenerative mitochondriopathies. *J. Alzheimers. Dis.* **17**, 737–51 (2009).

# List of papers included

Ligand binding in allosteric flavoproteins, Part 1. Quantitative analysis of the interaction with NAD$^+$ of the apoptosis inducing factor (AIF) harboring FAD in the reduced state

Ligand binding in allosteric flavoproteins, Part 2. Quantitative analysis of the redox-dependent interaction of the apoptosis inducing factor (AIF) with its protein partner

Ligand binding in allosteric flavoproteins, Part 1.

# Quantitative analysis of the interaction with NAD$^+$ of the apoptosis inducing factor (AIF) harboring FAD in the reduced state

Paolo Cocomazzi[1], Luca Sorrentino[1,2], Federica Cossu[3], and Alessandro Aliverti[1*]

[1]Department of Biosciences, Università degli Studi di Milano, via Celoria 26, 20133 Milano, Italy.

[2]Current address: Department of Chemistry, Università degli Studi di Milano, via Golgi 19, 20133 Milano, Italy.

[3]CNR-IBF, Consiglio Nazionale delle Ricerche – Istituto di Biofisica, via Celoria 26, 20133 Milano, Italy.

*Corresponding author: email alessandro.aliverti@unimi.it

Running head: ligand binding affinities in allosteric flavoproteins

# Ligand binding in allosteric flavoproteins, Part 1. Quantitative analysis of the interaction with NAD$^+$ of the apoptosis inducing factor (AIF) harboring FAD in reduced state

Paolo Cocomazzi, Luca Sorrentino, Federica Cossu, and Alessandro Aliverti

## Abstract

To perform their action usually flavoproteins interact with a variety of low molecular weight partners, including electron transporters, yielding transient complexes whose tightness is often controlled by the redox state of the bound flavin cofactor. As a case study, here we describe the quantitative analysis of the redox-dependent interaction of the mammalian apoptosis inducing factor (AIF) with its NAD$^+$ ligand. In particular, we report a protocol for the spectrophotometric titration of AIF in its reduced state under anaerobic conditions with NAD$^+$, in order to determine the dissociation constant of the resulting complex.

## Key words

Protein-ligand interaction, Dissociation constant, Electron carrier, Charge-transfer complex, Anaerobiosis, Photoreduction, Spectrophotometric titration.

## 1. Introduction

In flavoenzymes, allostery is often displayed as the modulation of the affinity of the ligand binding sites of the protein determined by the redox state of the bound flavin cofactor.

The apoptosis-inducing factor (AIF), a mitochondrial intermembrane-space FAD-containing protein, is paradigmatic in such behavior [1]. AIF possesses a three-domain organization, comprising FAD-binding, NAD-binding and C-terminal domains [2]. FAD reduction dramatically increases AIF affinity for $NAD^+$, whose binding yield a very tight $FADH^-$-$NAD^+$ charge-transfer (CT) complex, extremely resistant to oxidation by $O_2$. In addition to lock the protein in the reduced state, CT formation triggers a general rearrangement of the protein tertiary structure, which induce a change also in its quaternary level of organization [1,2]. Indeed, FAD reduction is strictly coupled to the transition from the monomeric to the dimeric state of AIF [3]. The ability of AIF to adopt a CT/dimeric state is crucial for its functions and, in particular, for its role in assisting the biogenesis and maintenance of respiratory complexes. This is testified by the observation that pathogenic variants of human AIF, hampered in undergoing such transition, are the cause of mitochondriopaties with often severe neurological and muscular symptoms [4].

The ability to adopt the CT/dimeric state has been recently shown to be crucial for the role of AIF, in conjunction with its CHCHD4/MIA40 [5] partner, in assisting the import and folding of nuclear-encoded mitochondrial-targeted proteins, as well as their maturation by the formation of disulfide bonds [6].

Thus, the study of the interaction of AIF in different redox states with $NAD^+$/H is of paramount importance to investigate its action at the molecular level and to interpret the pathological effects of some of its allelic variants.

Here, we describe a protocol for the characterization on a quantitative basis of the complex between the reduced form of AIF and NAD$^+$. Usually, flavin nucleotides and flavoproteins are reactive towards molecular oxygen, so that, to preserve their reduced state during *in vitro* experiments, anaerobic conditions are required. Thus, a specifically designed anaerobiosis apparatus and vacuum glassware items are required to apply this method. The experimental procedure here described to analyze AIF-NAD$^+$ interaction, with the appropriate modifications, could find applications in the study of other flavoproteins. In a separate chapter of this book we report a titration procedure to determine the dissociation constants of the complexes formed by AIF under different redox states with its protein partner CHCHD4/MIA40.

## 2. Materials

NAD$^+$ and NADH were purchased from Sigma-Aldrich. All other chemicals were analytical grade. Water used for the preparation of all solutions was purified using Elix and Milli-Q systems connected in series to attain a final conductivity of about 18 MΩ × cm at 25 °C. All solutions were filtered through low-extractable 0.22 μm filters (*see* **Note 1**).

### 2.1. Instrumentation and other devices

1. Desalting cartridge: 10 ml PD10 cartridge (GE Healthcare).

Spectrophotometer: any UV-Vis spectrophotometer suitable to accommodate an anaerobiosis cuvette may be used. In our case, a diode-array 8453 spectrophotometer (Agilent) is used to record all spectra during the entire procedure.

3. Anaerobiosis apparatus: vacuum-nitrogen manifold system.

4. Anaerobiosis cuvette: in our case, a customized spectrophotometric anaerobic cuvette (Fig. 1A), purchased from a local scientific glassblower (Arbore Cataldo, Milano, Italy), based on a quartz 1 ml optical cell, is used.
5. Vacuum flask: in our case, a 50 ml vacuum flask (Fig. 1B) was obtained from the above provider, specifically designed to be suitable to make the titrant solution anaerobic and to transfer it to a graduated microsyringe (*see* **Note 2**).
6. Gas-tight microsyringe: 100 μl gas-tight graduated microsyringe with a glass adaptor for the connection to the side arm of the anaerobiosis cuvette (Fig. 1A).
7. Vacuum grease: high-vacuum grease (Apiezon, type N) to lubricate glass-to-glass connections.
8. Infrared light filtration device: in our case, a thin-layer-chromatography glass container about 10 cm wide filled with water is used.
9. Light source: in our case, a conventional slide projector is used.
10. Data analysis and graphing software: any scientific data analysis software able to perform non-linear regression using equations provided by the user can be used. In our case, GraFit 5.0 (Erithacus Software Ltd, Wilmington, Sussex, Great Britain) for Microsoft Windows is adopted.

### 2.2. Solutions

1. Target flavoprotein stock solution: in our case, recombinant mouse AIFΔ1-101 (hereafter indicated as AIF) is overproduced in *Escherichia coli* as a fusion with a C-terminal His-tag, using a plasmid based on the pKK223-3 vector.

Expression and purification of AIF are reported elsewhere [3]. The protein is typically obtained at the final concentration of about 0.5 mM, determined spectrophotometrically on the basis of $\varepsilon_{452} = 12.84$ mM$^{-1}$cm$^{-1}$ and stored at -20 °C in 50 mM Tris-HCl, pH 7.4 (at 25 °C), 10% glycerol (*see* **Note 1**).

2. Protein medium: the composition of the protein solution medium depends on the physico-chemical feature of the target protein. For AIF, 2 × protein medium is 100 mM Na-phosphate, pH 7.5 (*see* **Note 1**).
3. EDTA solution: 150 mM EDTA, pH 7.5. The pH of the solution should match that of the protein medium.
4. 5-deazariboflavin solution: 70 mM 5-deazariboflavin in $H_2O$. The chemical is not available from commercial suppliers: in our case, it was a gift of Dr. Sandro Ghisla. The compound can be quantified spectrophotometrically using $\varepsilon_{390} = 12.39$ mM$^{-1}$cm$^{-1}$.
5. Titrant solution: the chemical nature and concertation of the titrant depends of the protein and the ligand under study. In the case of AIF, the solution is 400 μM $NAD^+$ in $H_2O$. The pH of the solution should be adjusted to match that of the protein medium (*see* **Note 3**).

## 3. Methods

### 3.1. Spectrophotometric titration with $NAD^+$ of the reduced form of AIF under anaerobic conditions: theoretical background

Reaction of AIF with NADH occurs through an equilibrium strongly shifted towards FAD reduction generating a particularly stable $FADH^{-}$-$NAD^+$ CT complex.

Despite its virtually irreversible nature, the reaction is particularly slow, requiring up to one hour at low NADH concentration [2,3]. We found that reaction of AIF bearing reduced FAD and NAD$^+$ generates the same end-product at a considerably higher rate [3], thus requiring much lower reaction time. Based on these observations, we devised a titration procedure to analyze the interaction of AIF with its dinucleotide ligand, suitable for the determination of the dissociation constant of the resulting CT complex. The protocol consists in the photochemical reduction of the AIF-bound FAD under anaerobic conditions, using the procedure devised by Massey and Hemmerich [7], followed by the stepwise addition of a NAD$^+$ solution up to fully conversion of the protein to the corresponding CT-transfer complex. The procedure is carried out in a sealed anaerobic cuvette and the titration is monitored spectrophotometrically (Fig. 2A).

In the case of AIF, protein-ligand complex formation is assumed to occur *via* the following reaction:

$$\mathrm{AIF(FADH^-)} + \mathrm{NAD^+} = \mathrm{AIF(FADH^-\text{-}NAD^+)_{CT}}, \qquad \text{Eq. 1}$$

where AIF(FADH$^-$) indicates AIF harboring the reduced form of FAD, and AIF(FADH$^-$-NAD$^+$)$_{\mathrm{CT}}$ its CT complex with NAD$^+$, and whose equilibrium is described by the dissociation constant $K_{\mathrm{d}}$, as follows:

$$K_d = \frac{[\mathrm{AIF(FADH^-)}]\times[\mathrm{NAD^+}]}{[\mathrm{AIF(FADH^- - NAD^+)}_{CT}]} \qquad \text{Eq. 2}$$

The titration is predicted to proceed as a classical protein–ligand process, which under equilibrium follows the general equation of a 1:1 complex dissociation:

$$[PL] = \frac{[P]_T+[L]_T+K_d-\sqrt{([P]_T+[L]_T+K_d)^2-4[P]_T[L]_T}}{2}, \qquad \text{Eq. 3}$$

where [PL] here represents the concentration of the CT complex, $[P]_T$ that of total AIF(FADH—) – both free and ligand bound – and [L] that of total NAD$^+$ – both free and ligand bound.

### 3.2. Titration procedure

1. Desalt an aliquot of purified target protein by gel filtration on the PD10 cartridge to change its solvent to the selected protein medium (*see* **Note 1**).
2. Mix the protein with the appropriate amounts of stock solutions of EDTA, 5-deazariboflavin, and protein medium within the main body of the anaerobic cuvette (Fig. 1A) in order to obtain a total volume of 1.2 ml of a solution containing *ca.* 20 μM AIF, 15 mM EDTA, 1.5 mM 5-deazariboflavin, and $H_2O$ in 1 × protein medium.
3. Cover the side opening of the anaerobiosis cuvette with the glass stopper and close its upper turncock.
4. Connect the cuvette to the vacuum-nitrogen manifold system through a rubber tubing, open the upper turncock, and make the content of the cuvette anaerobic operating several cycles of vacuum application and nitrogen flushing.
5. Close the upper turncock of the cuvette.

6. Place the $NAD^+$ solution (*see* **Note 3** and **Note 4**) into the vacuum flask (Fig. 1B), connect it to the vacuum-nitrogen manifold system and flush the content of the flask with nitrogen for *ca.* 30 min to make it anaerobic.
7. Repeatedly rinse a gas-tight 100 μl glass microsyringe with the anaerobic $NAD^+$ solution and then fill up the syringe with this solution, while keeping the solution under nitrogen flux.
8. Assess the actual $NAD^+$ concentration spectrophotometrically on another aliquot of the solution, on the basis of $\varepsilon_{260} = 17.6$ $mM^{-1}cm^{-1}$.
9. Open the upper turncock of the anaerobiosis cuvette, flush its with nitrogen and open the cuvette side arm.
10. Connect the microsyringe, filled the titrant, to the side opening of the anaerobiosis cuvette through its terminal conic glass fitting, while keeping the cuvette content under constant nitrogen stream.
11. Close the upper turncock of the cuvette and disconnect it from the vacuum-nitrogen manifold system.
12. Place the cuvette-syringe assembly in the thermostatic cell holder of the spectrophotometer, and record the absorbance spectrum of the protein solution.
13. Irradiate of the protein solution using the light source to obtain photoreduction of the FAD prosthetic group, while keeping the cuvette at room temperature in vertical position at a distance of about 15 cm from the light source, separated from it by the glass container filled with water, in order to eliminate infrared radiation.

Irradiate the solution for single periods of 1-3 min, and gently mix the solution after each treatment. Record the absorbance spectrum after each illumination, allowing about 3 min equilibration before the measure. Repeated the operation until complete FAD reduction is obtained, which usually requires up to 15 min total irradiation time (*see* **Note 5**). For fully reduced AIF, the extinction coefficient $\varepsilon_{452} = 1.77\ \text{mM}^{-1}\text{cm}^{-1}$ is considered.

12. Make ten successive additions of 10 μl $NAD^+$ solution each. Gently mix the solution after each of them and record the spectrum after 3-10 min equilibration at 25 °C, as no further spectral changes are detectable (Fig. 2A). Figure 2A shows selected spectra recorded during a typical titration of AIF. At the end of the titration, open the upper turncock in and admit air into the cuvette. Mix the solution, and allow FAD to gain full re-oxidation, in order to verify that the original spectrum is recovered, indicating that no protein denaturation and/or FAD release had occurred. In the case of wild-type AIF, complete CT complex disappearance requires more than 1 h.

### 3.3. Data analysis

Usually ligand binding to flavoproteins induces changes in their absorption spectrum, which can be exploited to calculate complex concentration. In the case of AIF, the absorbance of the solution at 750 nm represents an effective measurement of the protein-ligand CT complex concentration, since other species present in the sample provide no contribution to $A_{750}$. Thus, we have:

$$A_{750} = \varepsilon_{750}^{PL} \times [PL], \qquad \text{Eq. 4}$$

Where $\varepsilon_{750}^{PL}$ is the molar extinction coefficient of the CT complex and [PL] its concentration.

To take into consideration sample dilution due to titrant addition, we must consider that:

$$[L]_T = \frac{V_a}{V_i+V_a}[L]_S \text{ and} \qquad \text{Eq. 5}$$

$$[P]_T = \frac{V_i}{V_i+V_a}[P]_i, \qquad \text{Eq. 6}$$

where $[L]_T$ and $[P]_T$ are total NAD$^+$ and total AIF concentration, respectively, $[L]_s$ the concentration of the NAD$^+$ titrant stock solution, $[P]_i$ the concentration of the target protein in the reaction mixture before the first addition of the titrant, and $V_i$ and $V_a$ the initial volume of the reaction mixture and the total titrant volume added, respectively. Equations 3, 4, 5 and 6 are combined to obtain the parametric expression of $A_{750}$ as a function of $V_a$, which is used to fit the titration data points. Non-linear regression analysis is performed by the data analysis software GraFit 5.0. The best fitting equation yields the estimate for both $\varepsilon_{750}^{PL}$ and $K_d$ (Eq. 3 and 4) of the complex. In Figure 2B a typical result of data analysis is shown. While this experimental approach allows only a gross estimate of the $K_d$ of the CT complex involving wild-type AIF, which is too low for an accurate determination (<50 nM), it proved extremely valuable for the analysis of variants of the protein displaying lower ligand affinity [3].

## 4. Notes

1. The assumption that the total amounts of target protein and titrant are known must be satisfied for the validity of Eq. 3. In addition, spectrophotometric data are strongly biased by particulate or aggregates suspended in the solution under analysis.

For these reasons, it is recommended to clarify protein solutions just before use by centrifugation or microfiltration. Moreover, protein storage media and titration conditions should be chosen in order to prevent protein denaturation and/or aggregation. Possible solution additives to be considered to these aims are glycerol and/or mild detergents. Physico-chemical parameters, like pH and ionic strength should be considered as well. A useful approach for the rapid screening of several conditions is the ThermoFAD technique [8].

2. For the maintenance of the vacuum glassware, we suggest to clean it immediately after use first by removing most part of the grease with paper wipes, next by throughoutly rinsing it water, and finally by eliminating residual grease traces by extensive rinsing with an organic solvent, such as cyclohexane. Occasionally, for deep cleaning, overnight treatment with a concentrated nitric acid solution is very effective.
3. It is important that the composition of the reaction mixture is not altered during the titration. Thus, the composition of the solvent of the titrant working stock solution should match that of the reaction mixture.
4. $NAD^+$ is relatively stable in solution at pH 6.0, but less stable under more basic conditions. If a series of titration experiments is planned, a single concentrated $NAD^+$ stock may be prepared in water adjusting its pH to about 6.0. Next, individual working solutions of the titrant in the appropriate buffer can be prepared for each experiment, just before use.
5. Some flavoproteins can turn out particularly hard to be reduced photochemically.

In these cases, the inclusion of micromolar amounts of an additional electron-transfer mediator can be considered. We found effective the use of methyl- or benzyl-viologen, which are colorless in the oxidized state, and whose low redox potential avoid the accumulation of their visible-light absorbing reduced forms during the photoreduction process.

## Acknowledgements

This work was supported by grants Linea 2, 2017 and 2018, from Università degli Studi di Milano to A. A..

## References

1. Brosey CA, Ho C, Long WZ, Singh S, Burnett K, Hura GL, Nix JC, Bowman GR, Ellenberger T, Tainer JA (2016) Defining NADH-driven allostery regulating apoptosis-inducing factor. Structure 24:2067-2079
2. Sevrioukova IF (2011) Apoptosis-inducing factor: structure, function, and redox regulation. Antioxid Redox Signal 14:2545-79
3. Sorrentino L, Calogero AM, Pandini V, Vanoni MA, Sevrioukova IF, Aliverti A (2015) Key Role of the Adenylate Moiety and Integrity of the Adenylate-Binding Site for the NAD(+)/H Binding to Mitochondrial Apoptosis-Inducing Factor. Biochemistry 54:6996-7009
4. Sevrioukova IF (2016) Structure/Function Relations in AIFM1 Variants Associated with Neurodegenerative Disorders. J Mol Biol 428:3650-3665
5. Hangen E, Feraud O, Lachkar S, Mou H, Doti N, Fimia GM, Lam NV, Zhu C, Godin I, Muller K, et al (2015) Interaction between AIF and CHCHD4 regulates respiratory chain biogenesis. Mol Cell 58:1001-1014

6. Modjtahedi N, Tokatlidis K, Dessen P, Kroemer G (2016) Mitochondrial Proteins Containing Coiled-Coil-Helix-Coiled-Coil-Helix (CHCH) Domains in Health and Disease. Trends Biochem Sci 41:245-260
7. Massey V, Hemmerich, P (1977) A photochemical procedure for reduction of oxidation-reduction proteins employing deazariboflavin as catalyst. J Biol Chem 252:5612−5614
8. Forneris F, Orru R, Bonivento D, Chiarelli LR, Mattevi A (2009) ThermoFAD, a Thermofluor-adapted flavin ad hoc detection system for protein folding and ligand binding. FEBS J 276:2833-2840

## Figure legends

**Figure 1. Special glassware for spectrophotometric measurements and related liquid handling under anaerobiosis conditions.** (**A**) Set for anaerobic titration, including anaerobiosis cuvette and gas-tight microsyringe. The syringe can be connected to the cuvette body in place of the side cap. (**B**) Vacuum flask. Solutions made anaerobic within the flask can be withdrawn trough the side opening using a gas-tight syringe.

**Figure 2. Representative titration of reduced AIF with NAD$^+$, under anaerobiosis.** (**A**) Selected absorption spectra, recorded as equilibrium conditions were established, before and after each stepwise titrant solution addition. The spectrum of the oxidized protein is shown for comparison (thin solid line). The arrow indicates the direction of the absorbance change upon increase of NAD$^+$ concentration. (**B**) Values of $A_{750}$, reflecting CT complex concentration, as a function of total titrant volume. Dots represent experimental data, while the solid line is the best-fitting curve corresponding to the interpolating equation.

**Figure 1. Special glassware for spectrophotometric measurements and related liquid handling under anaerobiosis conditions.** (**A**) Set for anaerobic titration, including anaerobiosis cuvette and gas-tight microsyringe. The syringe can be connected to the cuvette body in place of the side cap. (**B**) Vacuum flask. Solutions made anaerobic within the flask can be withdrawn trough the side opening using a gas-tight syringe.

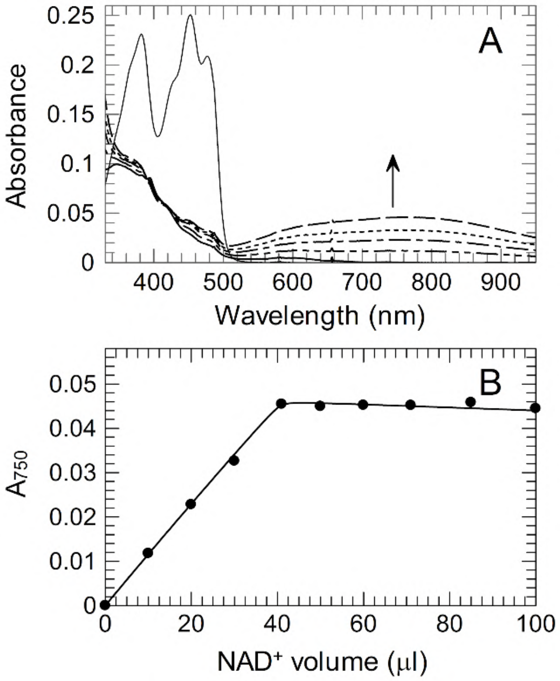

**Figure 2. Representative titration of reduced AIF with NAD$^+$, under anaerobiosis.** (**A**) Selected absorption spectra, recorded as equilibrium conditions were established, before and after each stepwise titrant solution addition. The spectrum of the oxidized protein is shown for comparison (thin solid line). The arrow indicates the direction of the absorbance change upon increase of NAD$^+$ concentration. (**B**) Values of $A_{750}$, reflecting CT complex concentration, as a function of total titrant volume. Dots represent experimental data, while the solid line is the best-fitting curve corresponding to the interpolating equation.

Ligand binding in allosteric flavoproteins, Part 2.

# Quantitative analysis of the redox-dependent interaction of the apoptosis inducing factor (AIF) with its protein partner

Paolo Cocomazzi[1], Delia Tarantino[1,2], Eloise Mastrangelo[3], and Alessandro Aliverti[1*]

[1]Department of Biosciences, Università degli Studi di Milano, via Celoria 26, 20133 Milano, Italy.

[2]Deceased. This paper is dedicated to her memory.

[3]CNR-IBF, Consiglio Nazionale delle Ricerche – Istituto di Biofisica, via Celoria 26, 20133 Milano, Italy.

*Corresponding author: email alessandro.aliverti@unimi.it

Running head: ligand binding affinities in allosteric flavoproteins

# Ligand binding in allosteric flavoproteins, Part 2. Quantitative analysis of the redox-dependent interaction of the apoptosis inducing factor (AIF) with its protein partner

Paolo Cocomazzi, Delia Tarantino, Eloise Mastrangelo, and Alessandro Aliverti

## Abstract

To perform their action usually flavoproteins interact transiently with a variety of molecular partners, whose binding is reciprocally affected and often controlled by the redox state of the bound flavin cofactor. As a case study, here we describe an approach for the quantitative characterization of the redox-controlled interaction of the mammalian apoptosis inducing factor (AIF) with one of its known protein partners, namely, the mitochondrial coiled-coil-helix-coiled-coil-helix domain-containing protein 4 (CHCHD4). In particular, we report a protocol for the titration of the flavoprotein in both in its oxidized and reduced states with CHCHD4, using an implementation of the MicroScale Thermophoresis (MST) technique.

## Key words

Protein-ligand interaction, Protein-protein interaction, Redox-linked binding, Microscale thermophoresis.

# 1. Introduction

Allostery, the conformational coupling of distant sites in a macromolecule, is a common feature of proteins, and flavoenzymes are no exception. In particular, the redox state of the bound flavin cofactor can induce long-range conformational changes in a flavoprotein, which, in turn, can affect the affinity of the binding sites for its ligands. The apoptosis-inducing factor (AIF), a mitochondrial intermembrane-space FAD-containing protein, is paradigmatic in such behavior [1]. AIF possesses a three-domain organization, comprising a FAD-binding, a NAD-binding, and a C-terminal domain [2]. FAD reduction dramatically increases affinity for $NAD^+$, whose binding yield a very tight $FADH^-$-$NAD^+$ charge-transfer (CT) complex, extremely resistant to oxidation by $O_2$. In addition to lock the protein in the reduced state, CT formation triggers a general rearrangement of the protein tertiary structure, which induce a change also in its quaternary level of organization [1,2]. Indeed, FAD reduction is strictly coupled to the transition from the monomeric to the dimeric state of AIF [3]. The ability of AIF to adopt a CT/dimeric state is crucial for its functions and, in particular, for its role in assisting the biogenesis and maintenance of respiratory complexes. This is testified by the observation that pathogenic variants of human AIF, hampered in undergoing such transition, are the cause of mitochondriopaties with often severe neurological and muscular symptoms [4]. Recently, it has been discovered that, in its CT/dimeric state, AIF forms a firm complex with another mitochondrial intermembrane-space protein, namely the mitochondrial intermembrane space import and assembly protein 40 (MIA40), also known as the coiled-coil-helix-coiled-coil-helix domain-containing protein 4 (CHCHD4) [5].

CHCHD4/MIA40 acts as a chaperone, assisting the import and folding of nuclear-encoded mitochondrial-targeted proteins as well as their maturation by the formation of disulfide bonds [6].

Thus, the detailed study of the interaction of AIF in different redox states with its protein ligand is of paramount importance to investigate its action at the molecular level and to interpret the pathological effects of some of its allelic variants. Here, we describe a protocol for the functional characterization on a quantitative basis of complex formation between both the oxidized/monomeric and CT/dimeric forms of AIF and its protein partner CHCHD4. This experimental procedure, with the appropriate modifications, could find applications in the study of other flavoproteins. In a separate chapter of this book, we report a titration procedure to determine the dissociation constants of the complex between AIF in reduced state and its dinucleotide ligand $NAD^+$.

## 2. Materials

NADH was purchased from Sigma-Aldrich. All other chemicals were analytical grade. Water used for the preparation of all solutions was purified using Elix and Milli-Q systems connected in series to attain a final conductivity of about 18 MΩ × cm at 25 °C. All solutions were filtered through low-extractable 0.22 μm filters.

### 2.1. Instrumentation and other devices

1. Metal-chelate chromatography cartridge: 5 ml HisTrap HP cartridge (GE Healthcare).
2. Desalting cartridge: 5 ml HiTrap HP Cartridge (GE Healthcare).

3. Microfuge: Any refrigerated bench centrifuge suitable to accommodate Eppendorf-type tubes.
3. Ultrafiltration device: any centrifugation-based ultrafiltration device with the appropriate molecular cut-off.
5. MicroScale Thermophoresis (MST) apparatus: Monolith NT.115 (NanoTemper Technologies GmbH, Munich, Germany).
6. Data analysis software: MO.Affinity Analysis software (NanoTemper Technologies GmbH).
7. Capillaries for MST: Monolith NT.115 standard treated capillaries (Nano Temper Technologies GmbH, Munich, Germany) (*see* **Note 1**).

### 2.2. Solutions

1. Target flavoprotein and ligand stock solutions: in our case, recombinant mouse AIFΔ1-101 (hereafter indicated as AIF) and its protein ligand CHCHD4 are both overproduced in *Escherichia coli* as protein fusion linked to a C-terminal His-tag, removable by thrombin proteolysis, using plasmids based on pKK223-3 and pET21a vectors, respectively. For AIF, expression and purification procedures are reported elsewhere [3]. The protein is typically obtained at a final concentration of about 0.5 mM in 50 mM Tris-HCl, pH 7.4 (at 25 °C), 10% glycerol. CHCHD4 is expressed in SHuffle T7 strain and isolated by nickel-chelate chromatography followed by gel filtration. Concentrations of AIF and CHCHD4 are determined spectrophotometrically on the basis of $\varepsilon_{452} = 12.84\ \mathrm{mM^{-1}cm^{-1}}$ and $\varepsilon_{280} = 13.325\ \mathrm{mM^{-1}cm^{-1}}$, respectively (*see* **Note 2**).

2. Protein labeling solutions: Labeling Kit RAD-tris-NTA (NanoTemper Technologies GmbH). The kit includes 50 × concentrated dye solution and 10 × concentrated PBS-T buffer (*see* **Note 3**).
3. NADH stock solution: 10 mM NADH in 10 mM Tris-HCl, pH 8.0. (*see* **Note 4**).
4. Thrombin stock solution: thrombin is available from different suppliers. We purchase it from Sigma-Aldrich. The lyophilized powder, which includes salt and Tris-HCl, pH 7.0, is dissolved in water before use (*see* **Note 5**).
5. PMSF stock solution: 200 mM PMSF in methanol (*see* **Note 6**).
6. Protein digestion medium: the composition of the thrombin digestion medium is a compromise between the conditions required for protease activity and those compatible with the stability of the fusion protein. For CHCHD4, 50 mM Tris-HCl, pH 8.0, 200 mM NaCl, 2 mM DTT is used.
7. Metal-chelate chromatography mobile phase: for CHCHD4, 50 mM Tris-HCl, pH 8.0, 200 mM NaCl, 10 mM imidazole is used.
8. Titration medium: the composition depends on the system under study. In the case of the AIF/CHCHD5 couple, 50 mM Tris-HCl, pH 8.0, 200 mM NaCl, 4 mM DTT (*see* **Note 2**).

## 3. Methods

### 3.1. Principle of the method

The technique is based on the measure of the concentrations of ligand-free and ligand bound forms of the target protein in solution through the record of the fluorescence emission intensity of sample mixtures.

To obtain such data, the target protein must be intrinsically fluorescent or labeled with an appropriate dye. MST measurements are performed on proteins and their ligands free in solution, using virtually any solvent, and allow the determination of dissociation constants over a very wide range of values. Strengths of the technique are the low concentration required for the target protein, the very small sample volumes – which are lower than 4 μl per titration point – and the confinement of samples within tiny glass capillaries that protect them from the contact with air. In brief, the instrument generates a locally restricted, highly precise temperature change in the sample by infrared laser light and monitors the resulting change in fluorescence [7,8].

Fluorescence change under irradiation is expected to follow an exponential decay time-course because of the progressive temperature increase of the monitored solution portion. Such change is due the combination of two different physical effects: temperature-related intensity change and thermophoresis, both of which are potentially affected by ligand binding. Thermophoresis is the movement of a chemical species along a temperature gradient, resulting in a change of its concentration as a function of temperature. To analyze the effect of protein-ligand interaction on the temperature dependent emission change, the normalized fluorescence ($F_{\text{norm}}$) is considered, *i.e.* the ratio between the emission at a definite time after laser activation ($F_1$) and that recorded at the baseline, before the irradiation start ($F_0$):

$$F_{norm} = \frac{F_1}{F_0} \qquad \text{Eq. 1}$$

The ligand-free protein and the protein-ligand complex contribute to $F_{norm}$ at different extents, so that:

$$F_{norm} = f_{norm}^{P} \times (1 - [PL]) + f_{norm}^{PL} \times [PL], \qquad \text{Eq. 2}$$

where [PL] is the protein-ligand complex concentration while $f^{P}_{norm}$ and $f^{PL}_{norm}$ are the specific normalized emission intensities of the free and bound protein, respectively.

Based on a 1:1 binding stoichiometry, the dependence of [PL] from the total ligand concentration $[L]_T$ is expected to obey to the following equation:

$$[PL] = \frac{[P]_T + [L]_T + K_d - \sqrt{([P]_T + [L]_T + K_d)^2 - 4[P]_T[L]_T}}{2}, \qquad \text{Eq. 3}$$

where [PL] represents the concentration of the protein-ligand complex, $[P]_T$ that of total target protein – both free and ligand bound – and $[L]_T$ that of total ligand – both free and protein bound.

In our case, purified recombinant AIF and CHCHD4 need to be chemically modified in order to be suitable as the target protein and the ligand, respectively, in MST titrations. AIF is labeled with a fluorescent dye, taking advantage from its His-tag (*see* **Note 3**), while the tag of CHCHD4 is removed to prevent possible interference in subsequent analyses due to sequestration of the label.

### 3.2. AIF labeling

The His-tagged form of AIF is labelled with the red fluorescent dye NT-647 using the Monolith NT His-Tag Labeling Kit RAD-tris-NTA according to the manufacturer directions. AIF is labeled under both its oxidized/monomeric and reduced CT/dimeric states.

1. Prepare the working dye solution by diluting 1:50 in 1 × PBS-T the concentrated dye solution.
2. Prepare two 100 μl incubation mixtures in 1 × PBS-T, each containing 200 nM AIF and either no nucleotide or 500 μM NADH, respectively.
3. Incubate the two AIF mixtures 1 h on ice to allow completion of the reaction yielding the CT/dimeric form of AIF, where NADH is present.
4. Add 100 μl working label solution to each AIF incubation mixture.
5. Incubate the two labeling mixtures for 30 min at room temperature in the dark.
6. Clarify the two labelled protein solutions by centrifugation at 15,000 × g for 10 min at 4 °C in a microfuge.

### 3.3. Preparation of tag-free CHCHD4

1. For tag removal, incubate purified CHCHD4 for 2 h at 37 °C with thrombin at a ratio of 10 units protease per milligram substrate in protein digestion medium (*see* **Note 5**).
2. Stop the proteolytic reaction by adding PMSF stock solution to obtain 1 mM final inhibitor concentration.
3. In order to remove residual tagged CHCHD4, separate the reaction mixture on a HisTrap HP cartridge using the metal-chelate chromatography mobile phase.
4. Change the buffer of the untagged protein solution by gel filtration on the HiTrap HP cartridge equilibrated in titration medium (*see* **Note 7**).
5. Concentrate the purified protein ligand by ultrafiltration to about 200 μM protein.

6. Clarify the ligand solution by centrifugation at 15,000 × g for 10 min at 4 °C in a microfuge, just before use.

### 3.3. Binding assays

1. For each titration experiment, prepare 16 microfuge tubes, numbered from 1 to 16.
2. In each tube, with the exception of tube 1, place a volume of 10 μl titration medium.
3. Add 20 μ untagged titrant CHCHD4 solution to tube nr. 1.
4. Transfer 10 μl of the content of tube nr. 1 to tube nr. 2 and carefully mix its content by pipetting.
5. Repeat the operation by transferring 10 μl of the content of tube nr. 2 to tube nr. 3, and so on, until tube nr. 16 is reached.
6. Discard 10 μl of the solution of tube nr. 16 is in order to have 10 μl 1:1 progressive serial dilutions of the titrant CHCHD4 in all test tubes.
7. To complete the samples, add 10 μl labeled target flavoprotein AIF – in either oxidized or CT complex state – to each of the 16 tubes of the titration series.
8. After extensive mixing by pipetting, transfer the content of each of the 16 tubes to a set of 16 Monolith NT.115 standard treated capillaries (*see* **Note 1**).

In the following two paragraphs, the typical results of two titration experiments on the AIF/CHCHD4 couple are reported, aimed to show expected possible outcomes of the application of the method. In the first case, the thermophoresis effect is used to quantify ligand binding, while in the second the observed ligand-induced fluorescence enhancement is exploited as the binding signal to cast the titration plot.

### 3.3.1. CHCHD4 titration of AIF in its oxidized monomeric state

MST measurements are performed at the baseline temperature of 24 °C with a fixed concentration of 50 nM AIF, and concentrations of CHCHD4 varied in the 3.85 nM – 126 μM range. Laser excitation power and MST power were set to 20% and 40%, respectively (*see* **Note 8**).

The capillary scan clearly shows that protein-protein interaction provides no fluorescence quenching or enhancing (Fig. 1A), while a clear ligand dose-dependent thermophoresis effect is evident from the recorded MST traces (Fig. 1B), where the normalized fluorescence change ($F_{\text{norm}} = F_1/F_0$) is reported as a function of irradiation time. To cast the titration plot, baseline emission ($F_0$) and measured emission selected over a specific irradiation time interval ($F_1$), selected in order to maximize signal-to-noise ratio (Fig. 1B), are considered. The effect of ligand binding generates a 14.4‰ maximal variation of the thermophoretic effect (Fig. 1C). Interpolation of data points with the theoretical equation for a 1:1 binding stoichiometry (Fig. 1C), obtained by combining Eq. 2 and Eq. 3, yields a $K_d$ value of 10.7 ± 2.4 μM for the AIF-CHCHD4 complex.

### 3.3.2. CHCHD4 titration of AIF in the reduced dimeric state

This experiment is performed at the fixed concentration of 50 mM AIF, also in this case. Here, the presence of 125 μM final concentration of NADH keeps the FAD prosthetic group of the protein in its reduced state as a CT complex with NAD$^+$. Under these conditions, AIF is known to adopt a homodimeric quaternary structure.

The low reactivity of the AIF CT complex towards $O_2$ and the embedment of the solutions within small-caliber glass capillaries prevents protein-bound reduced FAD to be re-oxidized during the experiment. CHCHD4 concentration is varied within the 3.85 nM – 126 μM range, as before. Laser excitation power and MST power are adjusted to 60% and 40%, respectively (*see* **Note 8**). However, in this case, the capillary scan at the baseline 24 °C temperature reveals that ligand binding induced a significant enhancement in fluorescence emission (Fig. 2A), suggesting a change in the fluorophore environment upon ligand binding. Thus, as suggested by the instrument manufacturer in such circumstances, the raw fluorescence change recorded before infrared irradiation is used to monitor protein-protein interaction. Anyway, also in our case, CHCHD4 binding induced a significant thermophoresis effect (not shown). Interpolation of data points with the same equation as before (Fig. 2B) yields a $K_d$ value of 92 ± 16 nM.

## 4. Notes

1. Different types of glass capillaries for MST are available, either uncoated or modified with various coatings. The choice should be oriented to avoid protein and/or ligand interaction with the glass surface. A capillary selection kit is available from Nano Temper Technologies GmbH, comprising three different kinds of capillaries.
2. The assumption that the total amounts of target protein and titrant are known must be satisfied for the validity of Eq. 3. In addition, spectrophotometric data are strongly biased by particulate or aggregates suspended in the solution under analysis.

For these reasons, it is recommended to clarify protein solutions just before use by centrifugation or microfiltration. Moreover, protein storage media and titration conditions should be chosen in order to prevent protein denaturation and/or aggregation. Possible solution additives to be considered to these aims are glycerol and/or mild detergents. Physico-chemical parameters, like pH and ionic strength should be considered as well. A useful approach for the rapid screening of several conditions is the ThermoFAD technique [9].

3. In the case the target protein does not display a suitable intrinsic fluorescence, it must be labeled. A large variety of strategies are available. The choice of the best solution should be guided by the feature of the protein itself – such as the presence of an affinity tag or reactive amino acid side chains on the protein surface, whose modification is not expected to interfere with ligand binding. Nano Temper Technologies GmbH offers different labeling kits covering a variety of modification chemistries.
4. NADH solutions are relatively stable at pH 8.0. We routinely prepare NADH stock solutions in 10 mM Tris-HCl, pH 8.0.
5. Digestion conditions should be experimentally found for each individual fusion protein.
6. PMSF solutions in absolute methanol or ethanol are stable at 4° or below, and can be safely stored for weeks.
7. It is important that the composition of the medium of the ligand working solution matches that of the titration medium in order to guarantee that the composition of titration mixtures is constant as the concertation of the titrant is varied.

8. Instrument settings should be empirically determined for each individual protein.

## Acknowledgements

This work was supported by grants Linea 2, 2017 and 2018, from Università degli Studi di Milano to A. A..

## References

1. Brosey CA, Ho C, Long WZ, Singh S, Burnett K, Hura GL, Nix JC, Bowman GR, Ellenberger T, Tainer JA (2016) Defining NADH-driven allostery regulating apoptosis-inducing factor. Structure 24:2067-2079
2. Sevrioukova IF (2011) Apoptosis-inducing factor: structure, function, and redox regulation. Antioxid Redox Signal 14:2545-79
3. Sorrentino L, Calogero AM, Pandini V, Vanoni MA, Sevrioukova IF, Aliverti A (2015) Key Role of the Adenylate Moiety and Integrity of the Adenylate-Binding Site for the NAD(+)/H Binding to Mitochondrial Apoptosis-Inducing Factor. Biochemistry 54:6996-7009
4. Sevrioukova IF (2016) Structure/Function Relations in AIFM1 Variants Associated with Neurodegenerative Disorders. J Mol Biol 428:3650-3665
5. Hangen E, Feraud O, Lachkar S, Mou H, Doti N, Fimia GM, Lam NV, Zhu C, Godin I, Muller K, et al (2015) Interaction between AIF and CHCHD4 regulates respiratory chain biogenesis. Mol Cell 58:1001-1014
6. Modjtahedi N, Tokatlidis K, Dessen P, Kroemer G (2016) Mitochondrial Proteins Containing Coiled-Coil-Helix-Coiled-Coil-Helix (CHCH) Domains in Health and Disease. Trends Biochem Sci 41:245-260

7. Duhr S, Braun D (2006) Why molecules move along a temperature gradient. Proc Natl Acad Sci USA 103:19678-19682
8. Wienken CJ, Baaske P, Rothbauer U, Braun D, Duhr S (2010) Protein-binding assays in biological liquids using microscale thermophoresis. Nat Commun 1:100
9. Forneris F, Orru R, Bonivento D, Chiarelli LR, Mattevi A (2009) ThermoFAD, a Thermofluor-adapted flavin ad hoc detection system for protein folding and ligand binding. FEBS J 276:2833-2840

## Figure legends

**Figure 1. Titration of AIF in its oxidized monomeric state with CHCHD4 using the MicroScale Monolith procedure.** (**A**) Lateral fluorescence emission scan of the capillary set recorded at baseline temperature, before laser irradiation. The number identifying the position of each of the 16 capillaries is reported below the horizontal axis. (**B**) MST traces of the 16 samples, showing the time-course of AIF concentration decrease as a consequence of the local increase in solution temperature, as well as the effect of the ligand concentration on thermophoresis. The two shadowed vertical bands represent the regions from which raw fluorescence emission data ($F_0$ and $F_1$, respectively) were obtained. (**C**) Titration plot reporting normalized fluorescence change ($F_{\mathrm{norm}} = F_1/F_0$) determined by the thermophoretic effect as a function of CHCHD4 concentration. Dots represent data point while the solid line is the best-fitting curve corresponding to the interpolating equation. Note the logarithmic scale of the horizontal axis.

**Figure 2. Titration of AIF in its CT-complex dimeric state with CHCHD4 using the MicroScale Monolith procedure.** (**A**) Lateral fluorescence emission scan of the capillary set recorded at baseline temperature, before laser irradiation. The number identifying the position of each of the 16 capillaries is reported below the horizontal axis. Note the fluorescence emission enhancement induced by the presence of CHCHD4 in a concentration-dependent fashion. (**B**) Titration plot reporting fluorescence change determined by CHCHD4-induced emission enhancement, as a function of CHCHD4 concentration.

Dots represent data point while the solid line is the best-fitting curve corresponding to the interpolating equation. Note the logarithmic scale of the horizontal axis.

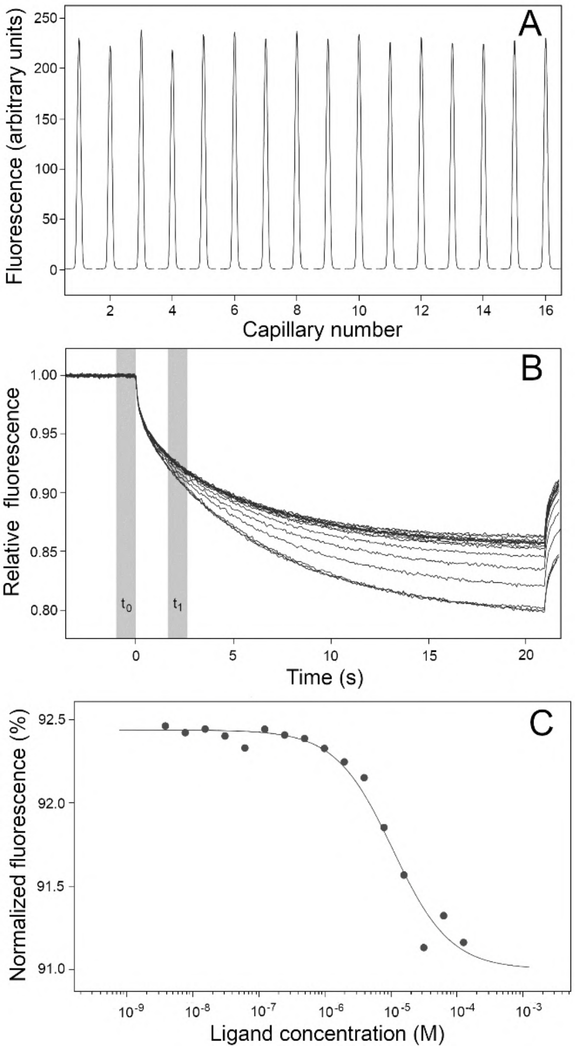

**Figure 1. Titration of AIF in its oxidized monomeric state with CHCHD4 using the MicroScale Monolith procedure.** (**A**) Lateral fluorescence emission scan of the capillary set recorded at baseline temperature, before laser irradiation. The number identifying the position of each of the 16 capillaries is reported below the horizontal axis. (**B**) MST traces of the 16 samples, showing the time-course of AIF concentration decrease as a consequence of the local increase in solution temperature, as well as the effect of the ligand concentration on thermophoresis. The two shadowed vertical bands represent the regions from which raw fluorescence emission data ($F_0$ and $F_1$, respectively) were obtained. (**C**) Titration plot reporting normalized fluorescence change ($F_{\mathrm{norm}} = F_1/F_0$) determined by the thermophoretic effect as a

function of CHCHD4 concentration. Dots represent data point while the solid line is the best-fitting curve corresponding to the interpolating equation. Note the logarithmic scale of the horizontal axis.

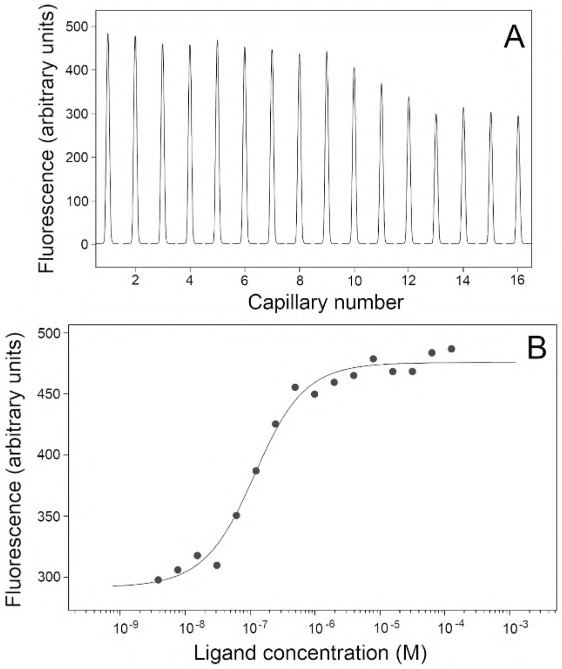

**Figure 2. Titration of AIF in its CT-complex dimeric state with CHCHD4 using the MicroScale Monolith procedure.** (**A**) Lateral fluorescence emission scan of the capillary set recorded at baseline temperature, before laser irradiation. The number identifying the position of each of the 16 capillaries is reported below the horizontal axis. Note the fluorescence emission enhancement induced by the presence of CHCHD4 in a concentration-dependent fashion. (**B**) Titration plot reporting fluorescence change determined by CHCHD4-induced emission enhancement, as a function of CHCHD4 concentration. Dots represent data point while the solid line is the best-fitting curve corresponding to the interpolating equation. Note the logarithmic scale of the horizontal axis.